MODELING OF PRECISION MOTION CONTROL SYSTEMS: A RELAY FEEDBACK APPROACH

CHEN SILU

NATIONAL UNIVERSITY OF SINGAPORE
2009

MODELING OF PRECISION MOTION CONTROL SYSTEMS: A RELAY FEEDBACK APPROACH

CHEN SILU
(B.Eng., NATIONAL UNIVERSITY OF SINGAPORE)

A THESIS SUBMITTED
FOR THE DEGREE OF DOCTOR OF PHILOSOPHY
DEPARTMENT OF ELECTRICAL AND COMPUTER ENGINEERING
NATIONAL UNIVERSITY OF SINGAPORE
2009

Acknowledgments

I would like to express my most sincere appreciation to all who had helped me during my PhD candidature at the National University of Singapore (NUS). First of all, I would like to thank my supervisor Associate Professor Tan Kok Kiong for his helpful discussions, support and encouragement. Prof. Tan's wisdom, vision, devotion and gentleness brighten my research paths. Without his guidance and support, I would not have accomplished this thesis.

I would also like to express my gratitude to all my friends who helped me in the last four years. Special thanks must be made to Dr Huang Sunan for his closed collaboration and real-time discussion. Great thanks to Dr Tang Kok Zuea and Mr Tan Chee Siong, two senior officers in Mechatronics and Automation (M&A) Lab, for providing high-class laboratory environment for my research. Lots of thanks to Dr Teo Chek Sing and Dr Andi Sudjana Putra for their guidance of setting up dSPACE control platforms. Many thanks to Mr Yang Rui for working together to win the third prize in the first Agilent VEE Challenge. Thanks to Dr Zhao Shao, Dr Goh Han Leong, Mr Zhang Yi, Mr Chua Kok Yong and all my colleagues working and used to work in M&A Lab for their friendship and help.

I am thankful to NUS for providing the research scholarship to undertake my PhD research. Special thanks also to the mechatronics division of Singapore Institute of Manufacturing Technology (SIMTech), for providing the experiment setups for testing and verification.

Finally, I would like to thank my family for their endless love and support. Specially, I would like to express my deepest gratitude to my virtuous wife Lanlan for her understanding and support.

Contents

Summary

Precision motion control is highly desirable in modern industries such as machine tools, ultra-precision spindles, wafer probing and lithography, to achieve good positioning or tracking performance with high speed and high accuracy. The requirements on these motion control systems are clearly more stringent. However, due to their physical design limitations, the accuracy and bandwidth of precision motion control systems are limited by various nonlinear factors, such as stiction, friction and force ripples. The recently developed various "model-free" and "intelligent" control schemes have common drawbacks of taking long time to learn or search for the optimal parameters. In fact, in current practice, conventional auto-tunning PID control schemes, affiliated with model-based feedback/feedforward nonlinear compensators, are still most popular choices to achieve satisfying tracking performances with efficient and accurate models.

Since 1980s, the relay feedback technique has been widely used for linear system identification and controller auto-tunning, due to its simplicity and efficiency. In this thesis, the efficient models are proposed and relay feedback methods are extensively applied to identify the model parameters of various motion control systems. The modeling of nonlinear force between to contacting surface of machine subparts, such as stiction and

friction will be addressed in this thesis.

First, the modeling of stiction is addressed widely in pneumatic and hydraulic control valves. Stiction generally leads to oscillation in control loops, which affects the product quality, increase energy consumption and accelerates the equipment wear. Based on the strength and weakness of various existing physical and data-driven stiction models, a new data-driven stiction model is proposed. This model has simple two-layer, binary-tree logic structure, and the model is able to deal with expanded type of stiction patterns, including some special cases such as linear and pure deadzone.

Secondly, the limit cycle properties are analyzed for a class of system under triple-relay feedback, especially the locations and the stability of limit cycles, using the time-domain approach. This configuration directly maps to a Coulomb friction impeded servo-mechanical system under dual-channel relay (DCR) feedback. Based on these analysis, a new method is developed to identify the dynamical and friction parameters accurately with only a single relay experiment.

Thirdly, a method is developed to model recently proposed, four-parameter friction models using DCR. This four-parameter model is able to adequately describe the friction property when the servo system runs in both high- and low-velocity modes. Four important properties of oscillation induced under the DCR will be presented, based on which insights for the selection of relay parameters can be drawn. Based on this, a systematic set of procedures is developed to derive all the parameters of the model. This model will be directly useful in the design of the feedback controller and feedforward friction

compensator.

Finally, relay feedback is used to identify both friction force and force ripples caused by the magnetic structures in permanent magnet linear motors (PMLMs). Since the force ripples are not odd-symmetric, only biased limit cycles can be obtained in PMLM under hysteretic relay feedback. To leverage on this type of limit cycles with both harmonics and DC contents, dual-input describing functions are imported so that the harmonic balance conditions are given. A set of explicit formulae is obtained for directly computing the model parameters including friction and ripples with minimum number of relay experiments.

In order to show the background and motivation of the research clearly, related literature reviews on relay feedback analysis, stiction models, and friction and force ripple modeling techniques are given in the corresponding chapters. In addition, the simulation and/or real-time experimental results are presented to verify the effectiveness of the approaches throughout the thesis.

List of Tables

List of Figures

List of Abbreviations

CPU	Central Processing Unit
DCR	Dual-Channel Relay
DE	Differential Equations
DF	Describing Function
DFT	Discrete Fourier Transform
DIDF	Dual-Input Describing Function
DSP	Digital Signal Processor
FOPDT	First-Order-Plus-Dead-Time
ILC	Iterative Learning Control
MEMS	Micro-Electro-Mechanical-System
MV	Manipulated Variable
NLS	Nonlinear Least Square
OP	Operational Point

PC	Personal Computer
PID	Proportional-Integral-Derivative
PMLM	Permanent Magnet Linear Motor
PV	Process Variable
RBF	Radial Based Function
RFS	Relay Feedback System
RLS	Recursive Least Square
RMS	Root Mean Square
SIDF	Sinusoidal-Input Describing Function
SNR	Signal to Noise Ratio

Chapter 1

Introduction

1.1 Precision Motion Control Systems

Motion control is a core enabling technology for automation, in which the position and/or velocity of a machine are controlled using some type of devices, such as pneumatic or hydraulic control valves and modern electric motors. Today, the increasing requirements of ultra-precision applications demand ever more accurate models in motion control systems. Meanwhile, the high speed requirements of precision motion control desire fast determination of controller parameters, while the relay feedback technique has been widely used in autotuning of motion controllers. In this thesis, the development of efficient modeling techniques for precision motion control systems are further studied using relay feedback approaches.

1.1.1 Evolution of precision motion control systems

The history of precision engineering can be dated back to 300 B.C., when the float regulator mechanism was designed for realization of water clock function. The first servo motor, the steam flyball governor was developed by James Watt in 1769, using the

principle of proportional feedback control. Its improved version, the commonly known proportional-integral-derivative (PID) controller has been widely implemented in automatic control systems since industrial revolution, in various mechanical and electrical designs. Great leaps were made to the development of high precision machine tools and instruments in the late 1800s and early 1900s by the ruling engineers for the manufacture of scales, reticule and spectrographic diffraction grating. The microprocessor has expanded to motion control application in the late 1970s. Since then, new power electronic devices integrate into microprocessors in providing more efficient and powerful implementation of motion controllers. On-board logic circuitry became available for servo drives or amplifiers to control motor commutation, current and velocity control. The servo boards were analog with output voltage signals from the generators as a function of speed providing the precision velocity measurements for the servo system. The requirements of high productivity demand not only accurate but also high speed motion controllers. Since 1980s, the Astrom-Hagglund PID autotuner, based on the relay feedback technique, has been commercialized in industrial automation, which is able to allow fast determination of the control system parameters [10]. In recent years, electronic control is become ever more proficient as new microprocessors, DSPs, and other electronics devices supply the control platform with tremendous computing and processing timing power. Advances in actuators, such as direct drive motors, linear motors, and brushless motors are reducing traditional difficulties such as backlash, friction and parasitic system dynamics. Promising new materials such as ceramics and composites offer

potential benefits in mechanical properties such as lower mass, improved damping, and reduced thermal effects. The advances in sensors, due to primarily to new techniques in optics, electronics and signal processing, give better feedback measurements. Today, ultra-precision machine tools under computer control can position the tool relative to the workpiece in a micron-scale accuracy.

1.1.2 Fields requiring precision control

The field of high-precision motion control is a subject attracting much research interest. The precision control technology is strongly required in the broad fields such as precision engineering, micromanufacturing, biotechnology, and nanotechnology.

Precision engineering is a set of systematized knowledge and principles for realizing high-precision machinery [71]. While conventional machines such as turning machines, drilling machines, milling machines etc. are still in use, the development of machining processes to provide high precision components has introduced new machining via laser cutting, hydrodynamic fluids, chemical substances, etc. Nowadays, there has been a trend towards non-contact machining as apposed to contacting one [91], such as air-bearing systems.

Micromanufacturing is the industry to design and fabricate the micro-devices in microelectronics. Micro-fabrication covers a range of manufacturing processes that produce patterns or layers of material to form microstructures. Lithography and Micro-Electro-Mechanical-Systems (MEMS) are common examples of micro-fabrication processes. Micro-assembly is another important process for precision engineering.

Biotechnology is a technological application that uses biological systems, living organisms, or derivatives thereof, to make or modify products or processes for specific use [99]. Modern biotechnology is often related to genetic alternation of living materials, such as microorganisms, plants and animals, which requires manipulation of device with precision control in micrometer or even in nanometer scales, such as minimally invasive surgery and intracytoplasmic sperm injection (ICSI) [76] etc.

Nanotechnology is to study, development and processing materials, devices and systems in which structure on a dimension of less than 100nm is required functional performance. It covers nano-fabrication processes, he design, behaviors and modeling of nanostructures, methods of measurement and characterization at the nanometer scale. As ultra-precision manufacturing progresses enter the nanometer scale regime, nanotechnology may be deemed as a natural next step to precision engineering.

1.1.3 Architectures

Although the applications of precision motion control can be in various fields as in the above overview, the basic architecture of a typical motion control system generally contains [1]:

- A motion controller to generate motion profiles and close a position and velocity feedback loop.
- A drive or amplifier to transform the signal from the motion controller into a higher electrical current or voltage which is presented to the actuator.

- An actuator such as a electric motor, hydraulic pump, air cylinder or linear actuator for output motion.

- One or more sensors such as optical encoders, resolvers or Hall effect devices to feedback the position and/or velocity of the actuator to the motion controller, forming a closed-loop configuration.

- Mechanical components to transform the motion of the actuator into the desired motion, including ball screw, gears, belts, shafting, linkages and linear and rotational bearings.

Depending on the equipment functioning as motion controllers, the modern motion control systems are further categorized as PC-based and stand-alone motion control systems. The PC-based motion control systems either directly use the CPU of the PC as the controller, or have the DSP control cards installed on the PC. Both of them enable the easy monitoring and reconfiguration with some supporting software. Figure 1.1 shows the architecture of a PC-based X-Y table control system, with on-board DSP control card [41]. The stand-alone motion control systems, just as their names imply, use pre-programmed stand-alone programmable motion controllers for working in hazardous or special environment. In this thesis, for research purposes, PC-based motion control systems are mainly used in the experiments. However, the stand-alone setups have also been widely used in industrial automation, or even medical treatment. One example is a recently developed physiotherapy system in M & A Lab, NUS, using the

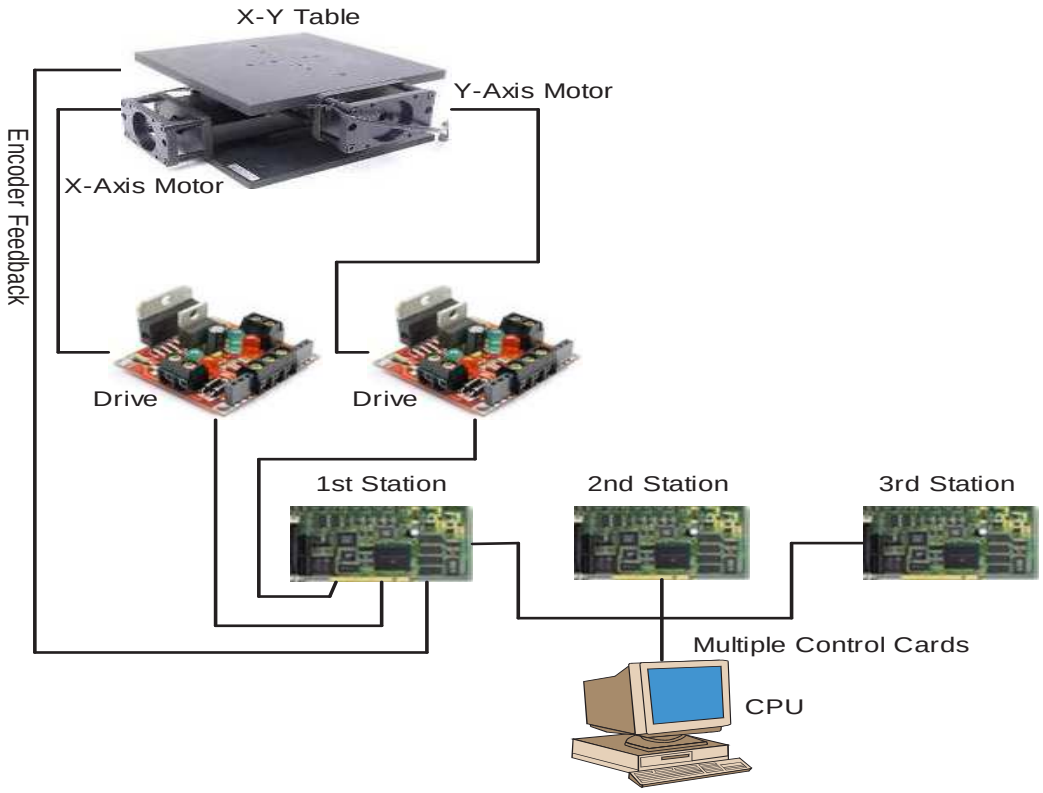

Figure 1.1: Architecture of a PC-based X-Y table motion control system.

CompactRIO® stand-alone controller, enable the patient to do the customized physical recovery exercises [20].

1.1.4 Control schemes

Although great leap has been made in control area, the precision motion control is challenging the control engineering to greater height. The control engineer needs to design a suitable controller which will effectively achieved the desired system characteristics, such as high precision, high speed requirements in precision motion control. However, there are practical issues which limit the controller performance, such as saturation of control efforts, uncertainty, noise and disturbances. Meanwhile, although great achievements have been reported on the development of advanced control techniques, limited

DSP processing capability may require simpler control algorithms to reduce processing time in lieu of higher sampling rates. Till now, the control schemes developed can be generally categorized into feedforward control and feedback control.

Feedforward control Feedforward is a term describing an element or pathway within a control system which passes a controlling signal from a source in the control system's external environment, often a command signal from an external operator, to load elsewhere in its external environment. The feedforward controller responds to its control signal in a pre-defined way, without any updated information on the status of the motion system. Feedforward controller can respond more quickly to known and measurable kinds of disturbance, but cannot do much with indeterministic disturbance such as environmental noise [91].

The technique of using feedforward control always involves finding an appropriate model of the system and enhancing the system performance by reacting to the predicted error. In the other way of thinking, the disturbance model, such as friction model or force ripple model, obtained in earlier procedures can be verified by the feedforward control, by checking whether the error due to the disturbance has been greatly decreased.

Feedback control Feedback control deals with any derivation from desired system behavior by measuring the system's variable and react accordingly. Till today, there are simply too many control schemes which have been proposed by researchers, the following are some methods which have been applied to motion systems:

- *PID feedback control* attempts to correct the error between a measured plant variable and a desired setpoint by calculating and then outputting a corrective action that can adjust the process accordingly and rapidly, to keep the error minimal.

- *Gain scheduling* is an approach to control of nonlinear systems that uses a family of linear controllers, each of which provides satisfactory control for a different operating point of the system [86].

- H_∞/H_2 *control* seeks to minimize certain weighting function to optimize system performance [19].

- *Sliding mode control*, a form of *variable structure control*, is a nonlinear control method that alters the dynamics of a nonlinear system by application of a high-frequency switching control [33].

- *Backstepping control* is based on identified models and recursively working backwards to obtain a desired controller [56].

- *Adaptive control* involves self-adjustable control laws to cope with the systems with slow-time-varying parameters, generally according to certain Lyapunov functions [11].

- *Intelligent control* uses various AI computing approaches to design the controller, such as fuzzy logic control [102], neural network control [49] and learning control [101] etc.

Notice that the above basic control schemes can work together to form a more advanced control schemes which may achieved better performance, such as feedforward-feedback control [91], adaptive sliding mode control [82], adaptive back-stepping [57], etc.

1.1.5 Relay feedback techniques for precision motion control

The relay feedback technique has been introduced in control application since 1960s. Although the theoretical studies of relay feedback systems have been made with great leaps since 1970s, the applications of relay feedback are mainly limited to design of adaptive controllers [11] and autotuning of PID controllers [10]. The principle behind relay-based PID autotuning is simple; self-oscillation is generated with relay elements, from which the system characteristics are inferred and subsequently used to tune the controller. Recent research tries to use relay feedback systems for modeling of nonlinear hybrid systems, typically friction-impeded motion control systems, by the same basic principles. In Figure 1.2, interconnections between precision motion control, system identification and relay feedback are clearly shown in knowledge hierarchy. These knowledge points will be reviewed systematically in later chapters.

1.2 Objectives and Challenges

The main objective of this thesis is to enhance the accuracy of the motion control systems by proposing and identifying the models, including commonly nonlinearities such as frictions and force ripples efficiently and accurately, with relay feedback approaches. From above reviews and comparisons of commonly control schemes, PID controls, with

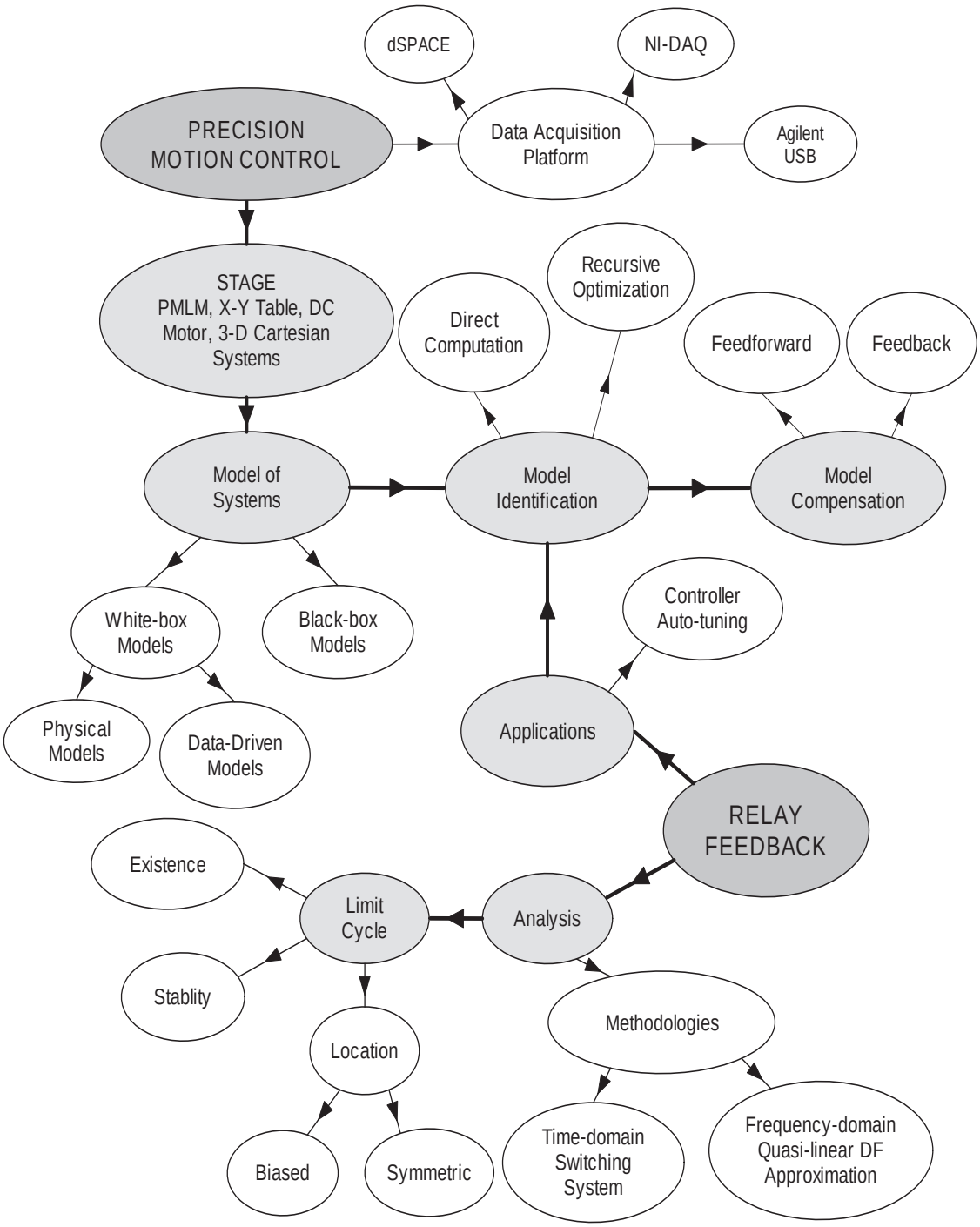

Figure 1.2: Interconnections among precision motion control, relay feedback and system identification.

its simplicity and efficiency, are still the most popular choice of controllers in motion control system. However, the various nonlinearities limit the accuracy of the motion control systems, since the conventional PID controllers are not able to handle time-varying nonlinearities such as stiction, friction or force ripples well.

Although the various advanced control schemes have been developed to overcome these nonlinear effects to improve the accuracy performance, these so-called "intelligent" control schemes have common drawbacks of heavy computational load or long-time learning processes, which may not be suitable for real-time applications. A more practical choice may be model-based control schemes, i.e., identify the various linear and nonlinear parameters within an appropriate model first, then apply the model-based feedforward-feedback (or feedback only) control [94], so that desired closed-loop linear characteristics are achieved while the nonlinear elements are eliminated. Thus, with this method, the key steps are to propose efficient models with minimal parameters and then identify the models parameters in efficient ways. The relay feedback approach, for its simplicity and light-computational load, is a good candidate. However, due to dissimilarity of linear and nonlinear systems, there are still great challenges in extending of relay feedback to nonlinear system identification.

The representative challenges regarding model proposition and model identification in motion control systems are given below.

Lack of simple, complete and user-friendly data-driven stiction model In industrial applications, control of valve's opening and closing motion is commonly seen in

process control. However, stiction (or stick friction) in control valve is common existing phenomenon leading to oscillation in control loops, which affects the product quality, increase energy consumption and accelerates the equipment weariness [105]. Existing physical models on valve stiction, based on Newton's 2nd law of motion requires too many parameters to be known, which increases the difficulty in analysis. The recently proposed data-driven stiction models for control valves only use simpler, fewer parameters to describe the stiction behaviors. However, the existing models are either incomplete, inefficient or tedious to understand. The computer programmers require simple, rigorous and efficient algorithms to describe such stiction behavior, so that the real-time applications are achievable.

Inefficient usage of limit cycle information Existing relay-based methods on modeling linear-nonlinear hybrid systems are mainly categorized into time domain based and frequency domain based approaches. For the time domain approach, current existing methods based on relay-feedback are mainly two-stage approaches, i.e., first identifying the parameters in the linear portions with differential inputs, then least-square optimizations are applied to obtain the models of nonlinear portions. These two-stage approaches are generally time-consuming and the information of limit cycles has not been fully utilized in the identification process.

Heavy computational load with nonlinear least-square optimization For frequency domain based approaches, the common approaches are by using describing func-

tion (DF) analysis with harmonic balance conditions. Since this category of approaches are based on quasi-linear approximations, the existing methods are mainly limited to simple, one-segment nonlinear models, such as Coulomb or Coulomb-viscous friction models. For identification of multi-segment and more accurate friction models, no closed-form identification formulae are available till now, since investigations of DFs of such nonlinear elements usually involve solving of transcendant equations, which are not possible in symbolic forms. To evade such difficulties, some of the existing methods use multi-parameter nonlinear optimization with large volumes of data, where the advantages of relay feedback are totally lost. Furthermore, the reliability of such approach is also a doubt, since the estimation of parameters using multi-parameter nonlinear optimization will generally converge to local minimum rather than global one.

Difficulty in modeling asymmetric nonlinearities For modeling of systems involving strong force ripples, the usage of the relay-based methods currently encounters greater difficulty. Force ripples are generally strong asymmetric, position dependent nonlinearities [91]. Due to their position depending characteristic, the model obtained based on one reference position is generally not applicable for another one, thus a fast, efficient modeling method is highly demanded. Due to its asymmetric properties, the self-excited oscillations by relay feedback are generally not symmetric as the case in friction modeling, but with strong bias. Although limit cycles with bias have been applied in linear system identification, there are still great challenges to use bias limit cycles for systems with nonlinearity.

1.3 Contributions

Base on the objectives and challenges lists in the earlier section, the following contributions have been made in this thesis.

Two-layer binary tree data-driven model for valve stiction A new data-driven stiction model for valve positioning systems is proposed in this thesis, with two-layer binary tree structure. This binary tree model has advantage of strict logic and simple structure, and it has close relationship with its physical counterpart. Thus, the difficulty of understanding and implementation of existing-data driven model is conquered. The logic behind the new model is carefully explained and illustrated. Simulations on different typical valve control loops shows the practical appeals of proposed models.

Identifying friction-impended servo-mechanical systems with single relay experiment The limit cycle oscillations arising for a class of linear systems under full state triple-relays feedback configuration are investigated. Locations of resultant limit cycles are derived which allow the exact time durations between two consecutive switchings of relays to be determined via numerical computation. The stability of limit cycles can be verified via the Jacobian of the Poincaré map. In motion control application, this triple-relays feedback configuration maps directly to a servo mechanical systems affected by Coulomb friction, under deliberate dual-channel relay (DCR) feedback. A new method, leveraging on the presented analysis, is thus developed to identify the dynamical friction parameters of the servo system accurately with only a single relay

experiment, surpassing existing results. Simulation examples and real-time experiments on a DC motor platform will show the effectiveness of proposed method.

Four-parameter friction modeling in position-encoded motion control systems with DCR feedback A recent proposed, two-segment, four-parameter friction model is able to describe the friction behavior in both low-velocity mode and high-velocity mode. A new, two-velocity-stage method is proposed to identify this model using DCR setup under position feedback loop. With describing function approximation, limit cycle characteristics induced under DCR will be presented, based on which the selection of relay parameters can be drawn. A systematic set of procedures to derive all the parameters of the model will be furnished. The proposed modeling method minimizes the usage of multi-parameter, nonlinear optimization. The model will be directly useful in the design of feedback controller and feedforward friction compensator. Simulations and real-time experiments are demonstrated to verify the effectiveness of this new method.

Concurrent friction and ripple modeling in servo-mechanical system using hysteretic relay A new method to identify various linear and nonlinear parameters in permanent-magnet linear motor, using a hysteretic relay feedback is proposed. To leverage on the biased limit cycles generated by asymmetric nonlinearities due to force ripples, the dual-input describing functions are imported. The explicit formulae, derived from the harmonic balance condition, enable direct computation of model parameters

with a minimum number of relay experiments. The practical appeal of proposed new method is verified by simulations and real-time experiments on a tubular permanent magnet linear motor.

1.4 Organization of Thesis

The thesis is organized as follows: In Chapter 2, with the review and comments of existing stiction models of motion control valves, a two-layer binary tree data driven model is proposed for describing sticky valve behavior correctly and efficiently. In Chapter 3, the relevant literature on the analysis of relay feedback system is reviewed first, and then a time-domain based relay feedback technique is developed to model the friction-impended servo-mechanical system by single relay experiment, using information of limit cycles' locations. In Chapter 4, the frequency domain approach is selected instead of time-domain approach, for solving more difficult modeling problems. After reviewing the existing friction models and friction modeling approach, a two-stage modeling method is developed to identify two-segment and four-parameter friction model, using DCR feedback. Next, in Chapter 5, the interest of application shifts to biased limit cycles instead of symmetric limit cycles in previous chapters. Following by reviews on permanent magnet linear motors and the force ripples arising from their physical design, a hysteretic relay based modeling technique is proposed to concurrently model friction and force ripples in arbitrary reference position by dual-input describing function analysis. Finally, conclusions and a few suggestions for future works are documented in Chapter 6.

Chapter 2

Two-Layer Binary Tree Data-Driven Model for Valve Stiction

2.1 Review of Stiction Models for Control Valves

A control valve is a device that starts, stops or regulates the flow of a fluid by adjusting the position of a movable part. A control valve requires an actuator that is capable of positioning the movable part to any value between the two extremes of fully open and fully closed. Depending on source of power, the actuators of control valves can be classified into pneumatic, electric and hydraulic types. However, the motion control of valves is commonly far from precise, mostly due to the commonly encountered stiction in associated with the control valves. The term, "stiction", is formed by combination of "stick" and "friction". Specially, in control valves, stiction is represented as the force necessary to be applied to a stem to put the valve in motion. The existence of stiction will induce system oscillatory, which may further affect the product quality, increase energy consumption and speed up the equipment weariness. From these points of view, stiction is highly undesirable in control valves, and a suitable model for description of

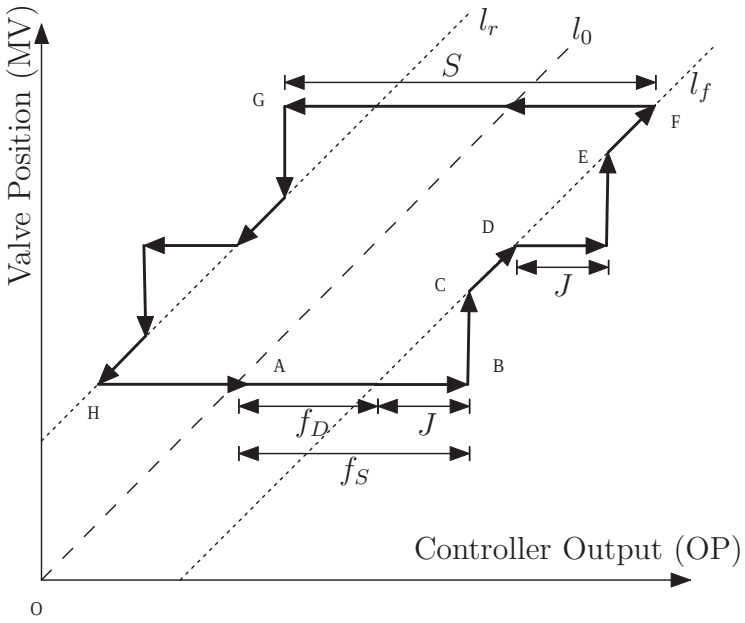

Figure 2.1: Normalized input-output behavior of a sticky valve.

the stiction behavior will greatly help to improve the accuracy of control valves.

2.1.1 Definition of stiction

Many literature have defined stiction in different ways [7] [47] [85] [53] [72] [79]. Based on careful investigation of experimental data, a new definition of stiction has been proposed by Choudhury, et al. [27], i.e., "*stiction is a property of an element such that its smooth movement in response to a varying input is preceded by a sudden abrupt jump called the slip-jump. Slip-jump is expressed as a percentage of the output span. Its origin in a mechanical system is static friction which exceeds the friction during smooth movement.*" The phase plot of the controller output (Operational Point or OP) versus actual valve position (Manipulated Variable or MV) of a valve suffering from stiction can be described as shown in Figure 2.1.

As illustrated in Figure 2.1, if there is no stiction, the valve will move along l_0, which is

linear and crosses the origin. However, since dynamic friction f_D exist in the valve, with the symmetric deadband $2f_D$, the valve will move along l_f in the forward direction, and it will move along l_r in the reverse direction. Additionally, due to the existence of static friction f_S, the stickband J is presented. Thus, the valve may move along the bond line $ABCDEFGH$ with stick-slip behavior. Since the model is normalized, MV will jump up (or down) to l_f (or l_r) for same amount J, after stick is conquered. The deadband and stickband represent the behavior of the valve when it is static, though the input of valve keep varying. The presence of slip jump is due to the abrupt increase of kinetic energy from potential energy stored in the actuator due to high static friction when the valve starts moving. However, it is difficult to estimate slip jump J from the output of a overall system (Process Variable or PV) and the controller output (OP) data because the slip jump in the valve output is filtered by the overall system dynamics. Some simple relations of parameters can be observed from Figure 2.1.

$$S = f_S + f_D, \tag{2.1}$$

$$J = f_S - f_D. \tag{2.2}$$

where f_S is maximum static friction and f_D is kinetic friction.

2.1.2 Review of a typical physical model

In earlier years, physical models of valve stiction were adopted, which requires a number of parameters to be known. In this section, a typical physical model [70] is formulated for the control valve stiction, so that the relationship directly linked to the practical

situation can be understood.

For a typical control valve, the simplified version of force balance equation [54], according to Newton's second law, can be written as

$$M\ddot{x} = F_a + F_r + F_f, \tag{2.3}$$

where M is the mass of the moving body, x is the relative stem position (PV), $F_a = Au$ is the force applied by pneumatic actuator where A is the area of diaphragm and u is valve input signal (OP), $F_r = -kx$ is the spring force where k is the spring constant [27].

The friction model F_s in (2.3), a summarized in [7] can be expressed with the following piecewise equation,

$$F_f = \begin{cases} -F_c \text{sgn}(\dot{x}) - \dot{x}F_v & \text{if } \dot{x} \neq 0 \\ -(F_a + F_r) & \text{if } \dot{x} = 0 \text{ and } |F_a + F_r| \leq F_s \\ -F_s \text{sgn}(F_a + F_r) & \text{if } \dot{x} = 0 \text{ and } |F_a + F_r| > F_s \end{cases} \tag{2.4}$$

The first line of (2.4) concerns the the slip state of the valve, where F_c is Coulomb friction and F_v is viscous friction. The second line is used for determining the static friction when the valve is stuck, where F_s is the maximum static friction. The third line represents the situation at the instance of break away. This model has been used for discussion of limit cycles generated by friction in [73].

The obvious disadvantage with applying the model presented above to a generic valve is the need to specify a rather large set of parameters. Parameters that need to be specified are M,F_s, F_c, F_v, k, A, a total of 6 parameters. Figure 2.2 shows the friction force characteristics in which the magnitude of the moving friction is smaller than that of the static friction. The friction force opposes velocity, as in (2.4), thus the force is

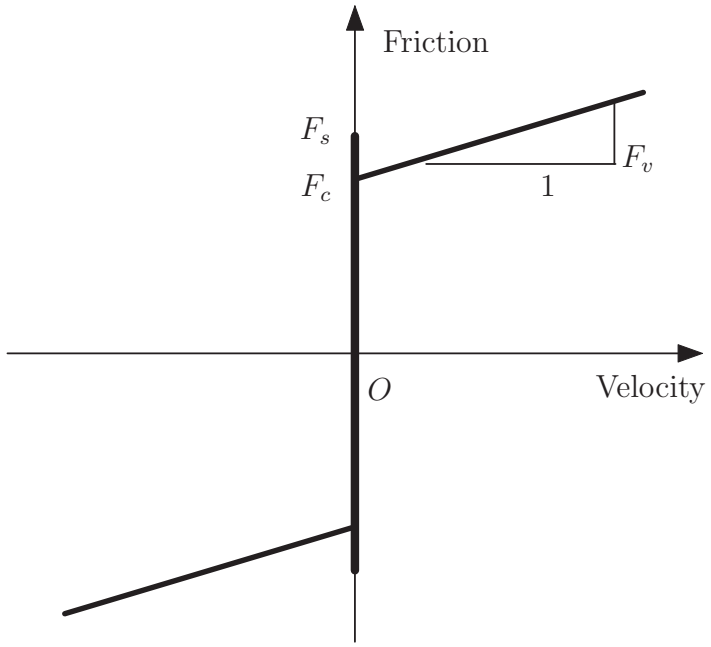

Figure 2.2: A physical friction model.

negative when the velocity is positive.

Open-loop test Consider the above stiction model with $F_v = 600$, $M = 1.5$, $k = 5 \times 10^4$, $A = 0.05$, and different sets of F_s and F_c will be chosen later to investigate the properties of stiction. Figure 2.3 shows SIMULINK block diagram for open-loop simulation. The block "Valve" is written in *.m* file according to (2.4). Since the discrete solver is used, the exact zero velocity condition in (2.2) seldom occurs. In order to observe the stick-slip properties of valves in the simulation, the condition is replaced by $|v| < \delta$, where δ is a small value. Moreover, to ensure that the output follows input in linear range, a correction factor p is cascaded to the end of the valve position output.

Figure 2.4 shows various patterns, w.r.t. difference choice of F_s and F_c, namely, linear, deadzone and stiction (only undershoot and no-offset cases). The linear pattern occurs

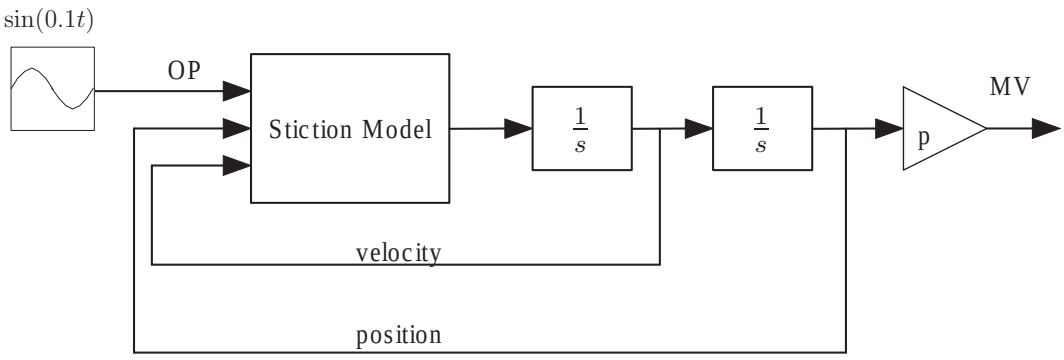

Figure 2.3: Open-loop simulation block diagram for physical model.

when $F_s = F_c = 0$. When $F_s = F_c \neq 0$, the deadzone pattern can be observed from MV-OP plot. When $F_s > F_c > 0$, the undershoot pattern of stiction is presented since the valve experience a sudden jump when it starts moving, which is different from deadzone pattern. When $F_s > F_c = 0$, the stiction without offset is detected since the output follows input well unless the valve is static. The overshoot pattern of stiction is practically not present in stick valve, because friction always resists motion.

Closed-loop test The closed-loop test can be applied to the above valve stiction model cascaded with FOPDT system $G(s) = 3e^{-5s}/(5s+1)$ under PI control feedback $C(s) = 0.1(s+5)/s$, with a step reference input $r(t) = 10U(t)$, as shown in Figure 2.5. Figure 2.6 gives the different (non)linear pattern observed from input-output waveforms, as well as MV-OP plot, in the steady-state. Unlike the forced oscillation of open-loop case, the oscillations in closed-loop are self-exciting. Since there are integrators in the physical model, even the deadzone pattern will induce limit cycle [68] [74]. It may not be easy to distinguish some of the patterns from waveforms in the left column, due to

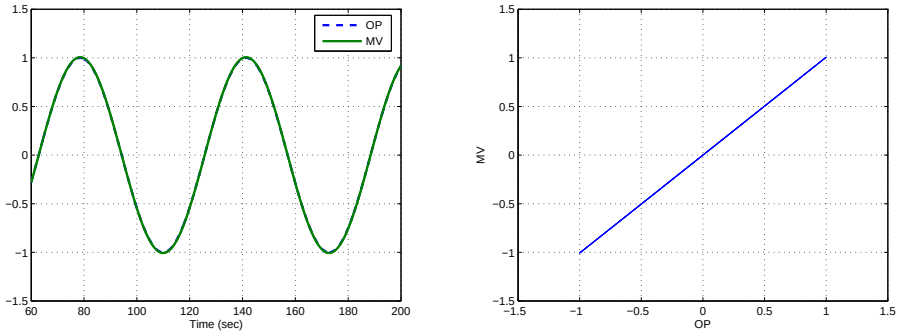

(a) Linear with $F_s = 0$ and $F_c = 0$.

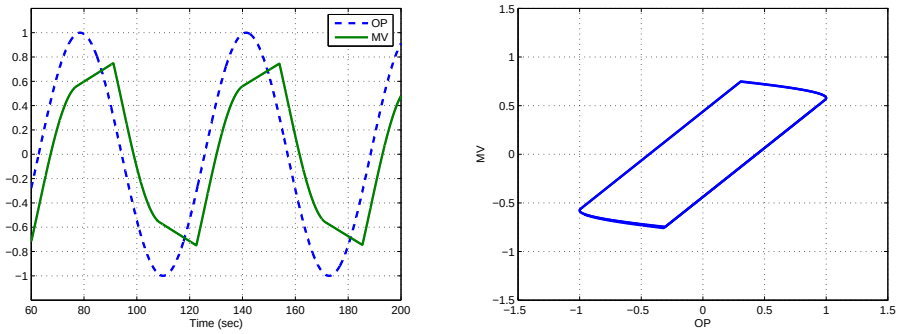

(b) Deadzone with $F_s = 2000$ and $F_c = 2000$.

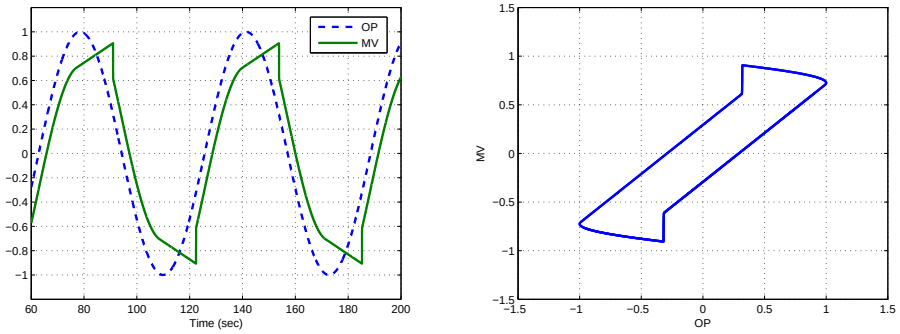

(c) Stiction (undershoot) with $F_s = 2000$ and $F_c = 1000$.

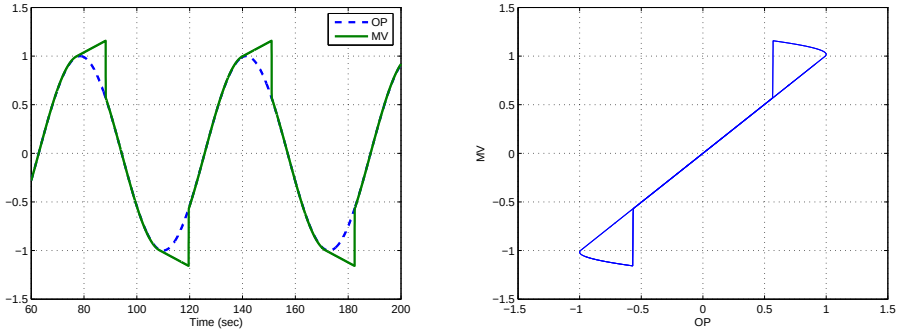

(d) Stiction (no offset) with $F_s = 2000$ and $F_c = 0$.

Figure 2.4: Open-loop response pattern of the physical model. Left column: OP / MV waveforms. Right column: MV-OP plot.

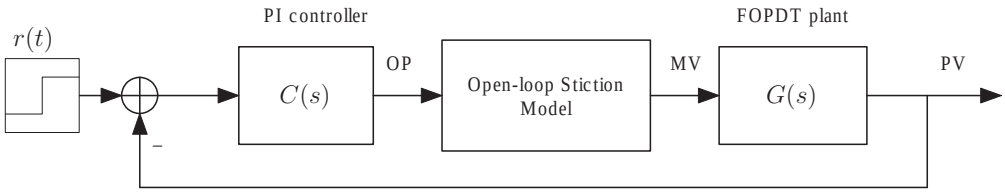

Figure 2.5: Closed-loop simulation block diagram.

the integral control action and the dynamics of the plant. Meanwhile, the patterns of MV-OP plot in closed-loop are somehow distorted, they can be viewed as the rotated versions of their open-loop counterparts. The out-of-phase problem between MV and OP can be greatly solved by the variable strength integral action PI controller [38].

2.1.3 Review of existing data-driven models

Recently, several data-driven models are proposed, which only use simple parameters to describe the stiction behavior [21] [27] [43] [52]. However, some of the models are either incomplete or tedious to understand.

Choudury et al.'s model The data-driven model proposed by Choudhury et al., as shown in Figure 2.7 [27] [21], uses the stick band S and slip band J as parameters to describe the above stiction behavior. This model can deal with most cases of stiction. However, as stated in [43], this model cannot describe the behavior when stiction does not exist, i.e., when $f_S = f_D = 0$. Moreover, if the controller output (OP) changes direction, according to the model, the output within current instant is set to be stuck directly. In practice, if the change of OP is large enough in the opposite direction, the valve may overcome the stickband as well as deadband and slip inversely [21]. The logic

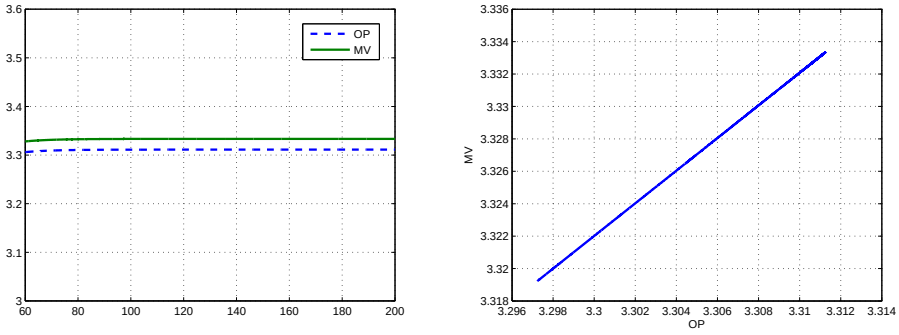

(a) Linear with $F_s = 0$ and $F_c = 0$.

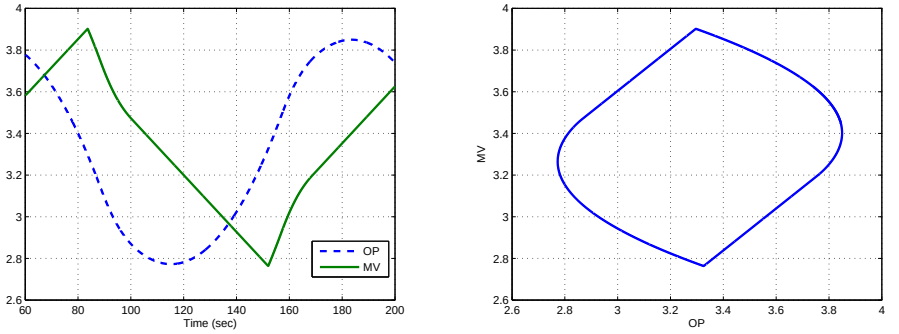

(b) Deadzone with $F_s = 2000$ and $F_c = 2000$.

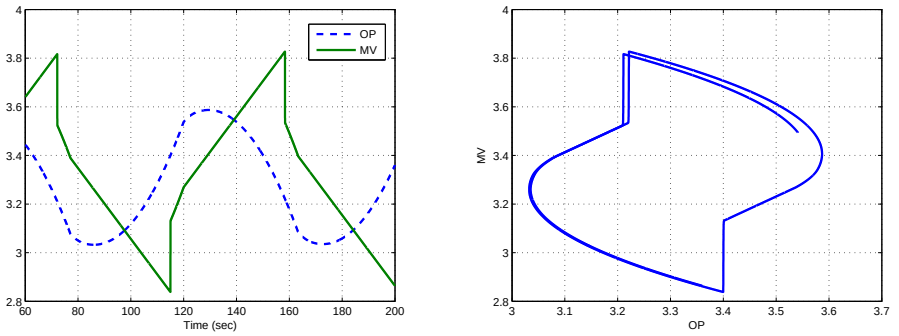

(c) Stiction (undershoot) with $F_s = 2000$ and $F_c = 1000$.

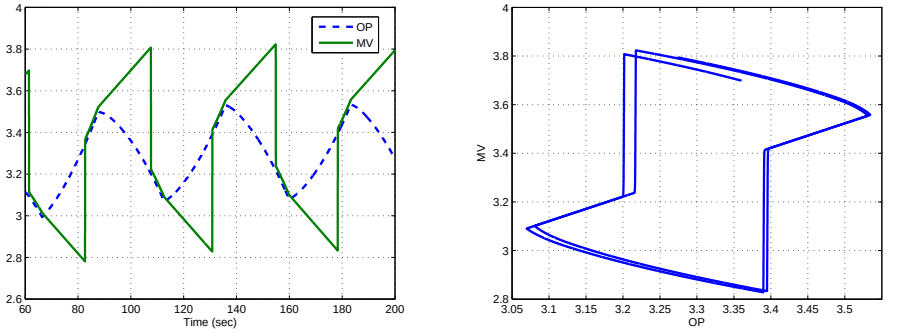

(d) Stiction (no offset) with $F_s = 2000$ and $F_c = 0$.

Figure 2.6: Closed-loop response pattern of the physical model. Left column: OP / MV waveforms. Right column: MV-OP plot.

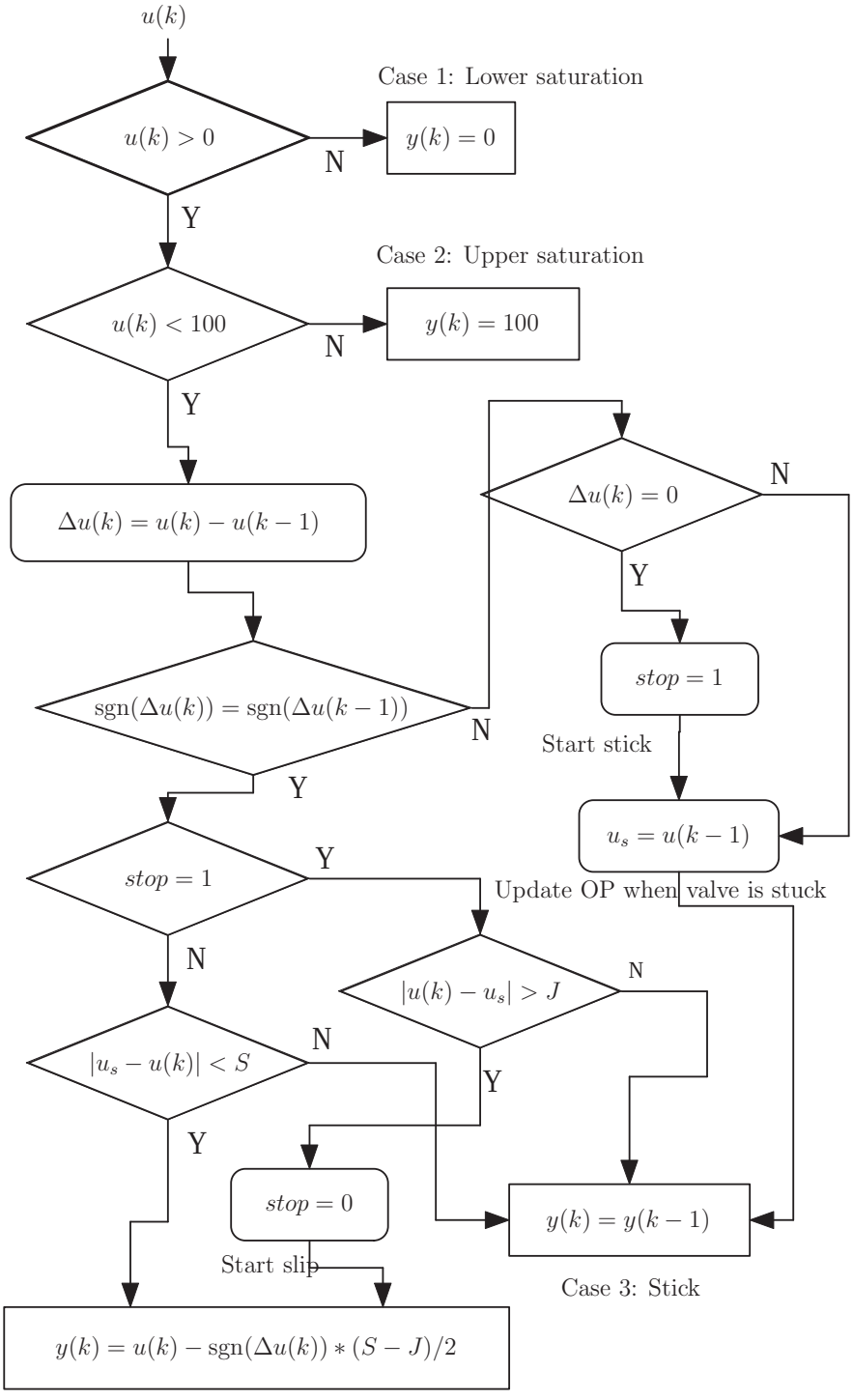

Figure 2.7: Choudhury's stiction model.

conditions are frequently crossing with each other, making the model be tedious for understanding and programming too.

Kano et al.'s model The model proposed by Kano et al. [52], as shown in Figure 2.8 removes these shortcomings of above. This model also describes the stiction behavior via S and J. It memorizes the input when the valve changes the direction and assume the valve stops, which is in line with Choudhury et al. model. However, an additional internal variable d is used to memorize the actual direction of valve sliding. However, the conditions of selection is still too many, and the time taken to determine the valve's position and moving status is relatively long.

He et al.'s model and its critical drawbacks He et al. [43] proposes a simplified data-driven stiction model. Compared to Choudhury et al. model in [27] and Kano et al. model [52], this model is formulated from a different perspective. It uses the static friction f_S and dynamic friction f_D as model parameters, which brings the model closer to the physical model, rather than the stick band S and slip jump J used in [27] and [52]. This model uses a temporary variable cum_u, the current accumulated force compensated by friction, which greatly simplifies the algorithm.

However, the model proposed by He et al. can be simplified further. First, $\text{sgn}(cum\_u - f_S) = \text{sgn}(cum\_u)$ if $|cum\_u| > f_S$. Secondly, the internal variable u_r can be simply replaced by the updated cum_u in either branch to reduce the complexity. After simplification, the model can be re-illustrated in Figure 2.9. Moreover, the original He et al.

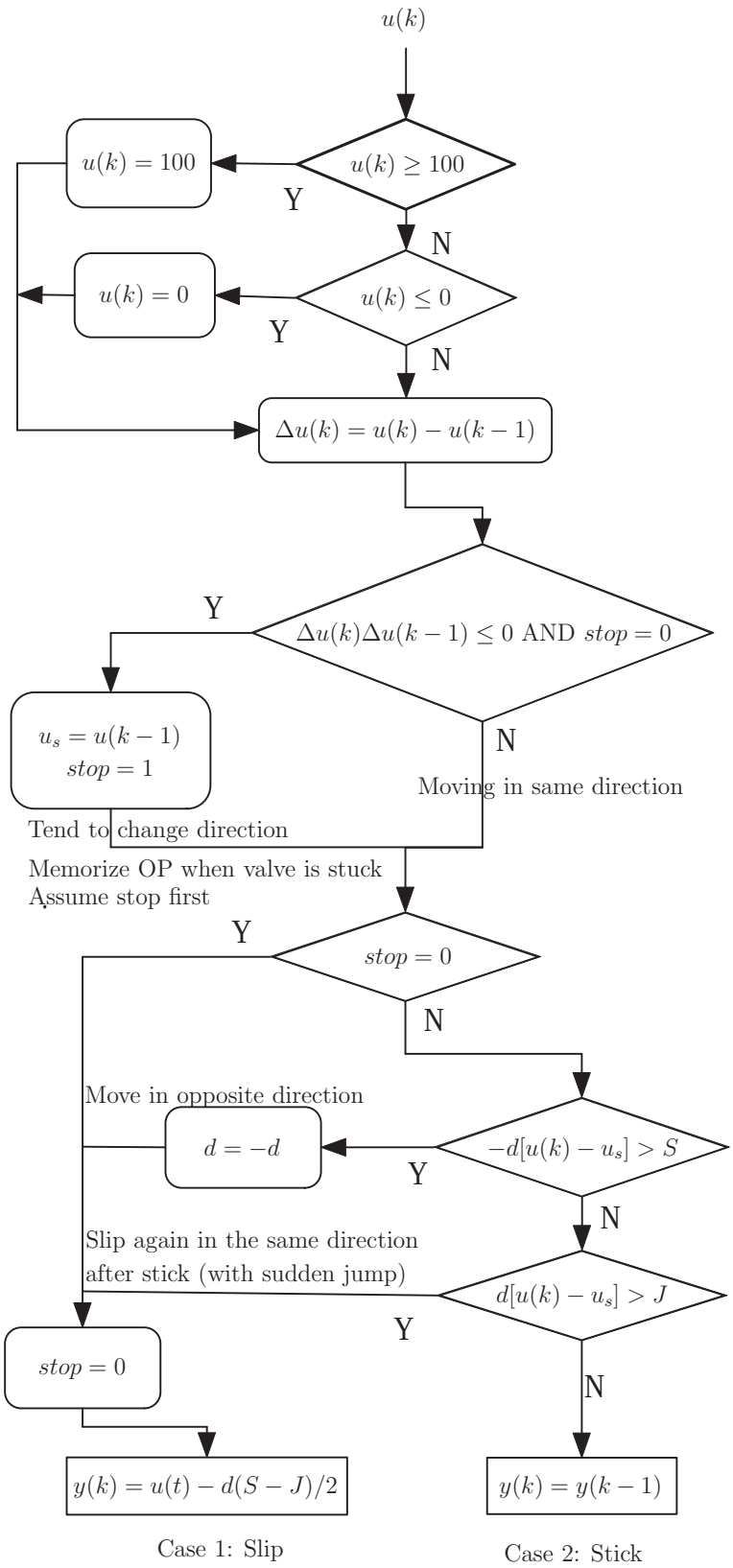

Figure 2.8: Kano's stiction model.

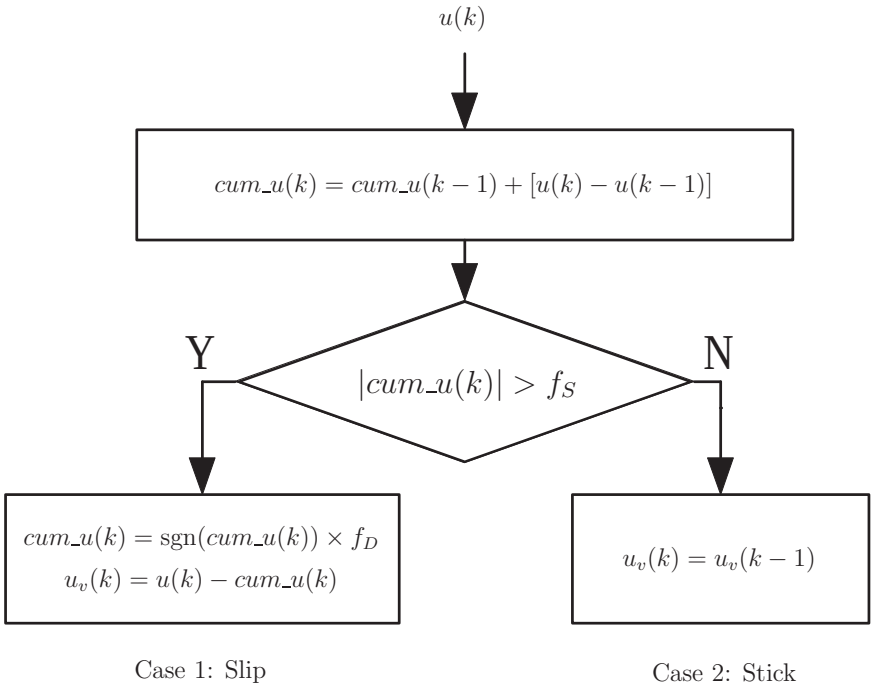

Figure 2.9: He et al. stiction model after simplification.

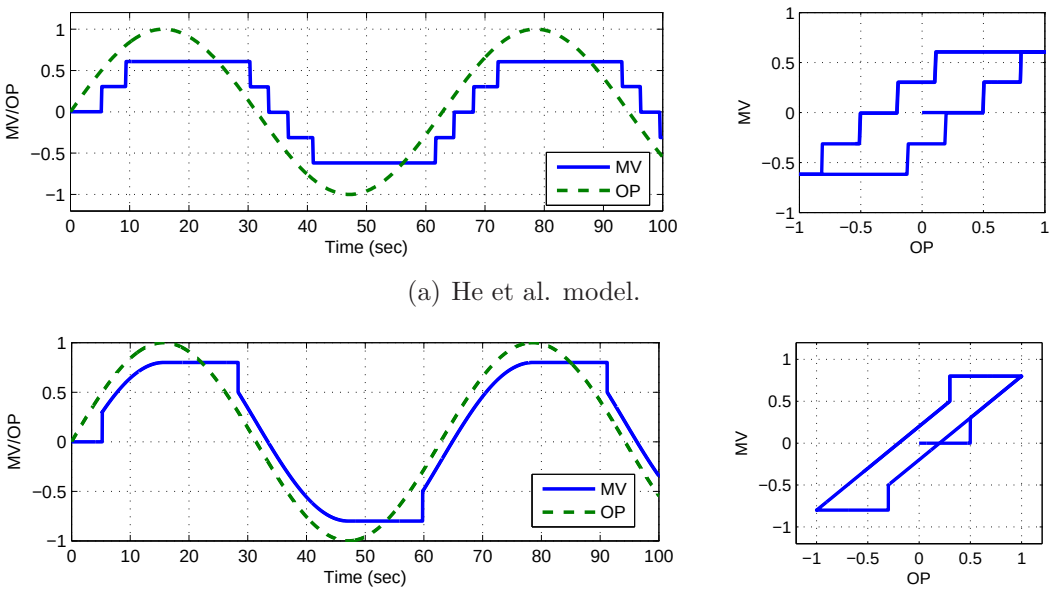

(a) He et al. model.

(b) Choudhury et al. model.

Figure 2.10: Open-loop behavior of He et al. model and Choudhury et al. model ($f_S = 0.5$, $f_D = 0.2$).

model has some limitations. Let's trace the model behavior in the two consecutive instants. As in Figure 2.9, if in current instant k, $|cum\_u(k)| > f_S$, i.e., the valve overcomes the static friction and starts moving, then $cum\_u(k)$ is updated as $cum\_u(k) = \pm f_D$. In the following instant, if the sampling period is small enough and the input changes smoothly, then $u(k+1) \approx u(k)$, so that $cum\_u(k+1) \approx cum\_u(k) = \pm f_D$ at the starting of the following instant $k+1$. Generally speaking, $|f_D| < f_S$, so the valve will certainly stick in the following instant $k+1$, according to He et al. model.

For example, set $u(t) = \sin(0.1t)$, $f_S = 0.5$ and $f_D = 0.2$. The open-loop response of the valve position (MV, or $u_v(k)$ in Figure 2.9) corresponding to the control signal (OP or $u(k)$) is shown Figure 2.10, w.r.t. He et al. model as well as Choudhury et al. model. Comparing Figure 2.10(a) with 2.10(b), the MV-OP plot is step-like by He et al. model, while the plot follows similar paths as in Figure 2.1 by Choudhury et al. model.

Logically, since the valve has two states, *stick* and *slip*, there are four possible state transitions, *stick to slip*, *keep sticking*, *slip to stick* and *keep slipping*. The main drawback of He et al. model is that it only covers the first two possible state transitions. In [43], it is assumed that the static friction affects every valve movement, so that the model is applicable. However, when the valve keeps slipping, the model becomes inadequate.

2.2 Proposed Two-Layer Binary Tree Model for Valve Stiction

Based on the review which will reveal the deficiencies and possible improved areas, a simple, complete valve stiction model with two-layer binary tree logic is proposed in

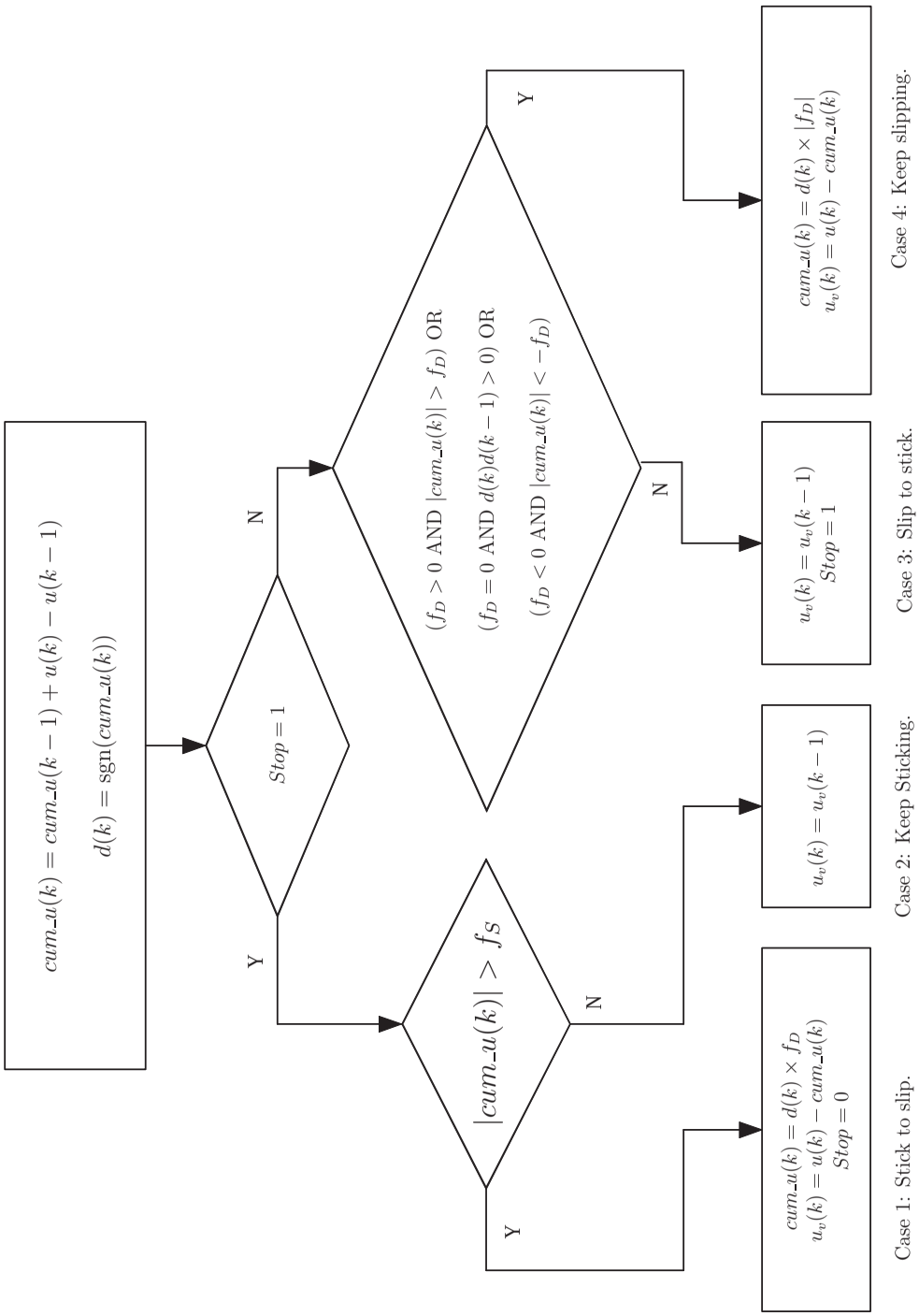

Figure 2.11: Improved version of stiction model.

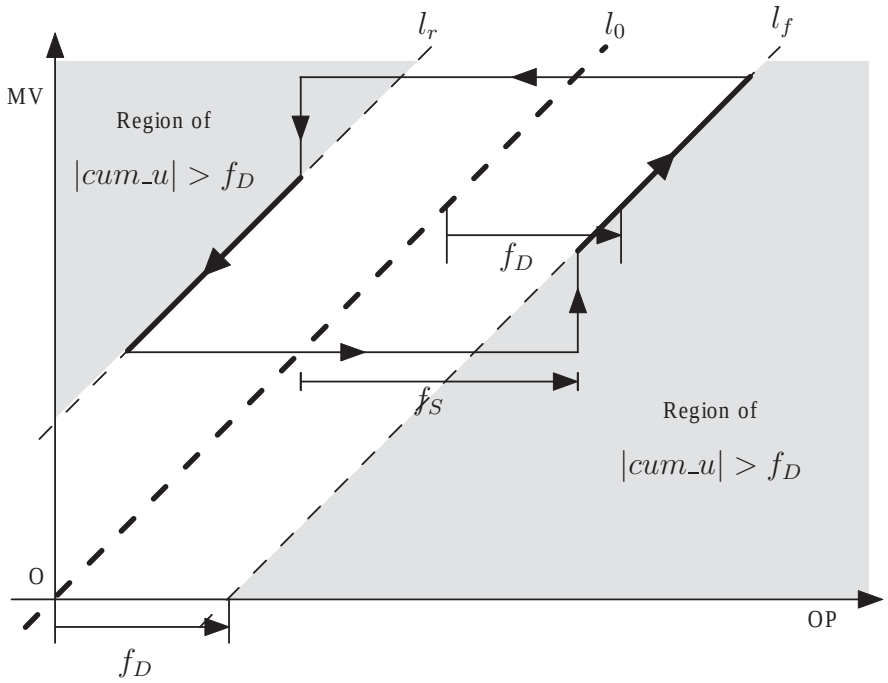

Figure 2.12: MV-OP plot of stiction with undershoot pattern.

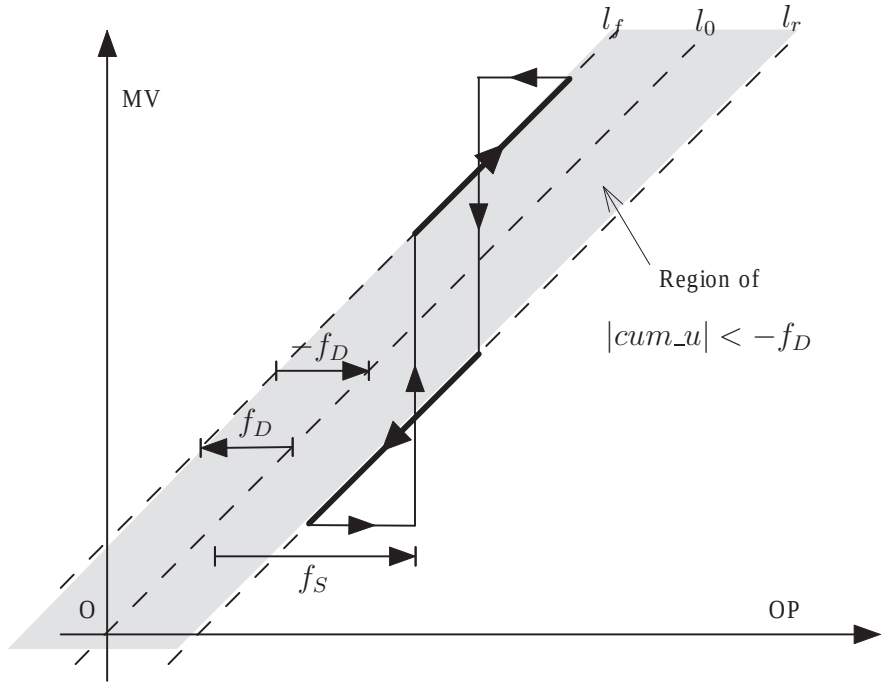

Figure 2.13: MV-OP plot of stiction with overshoot pattern.

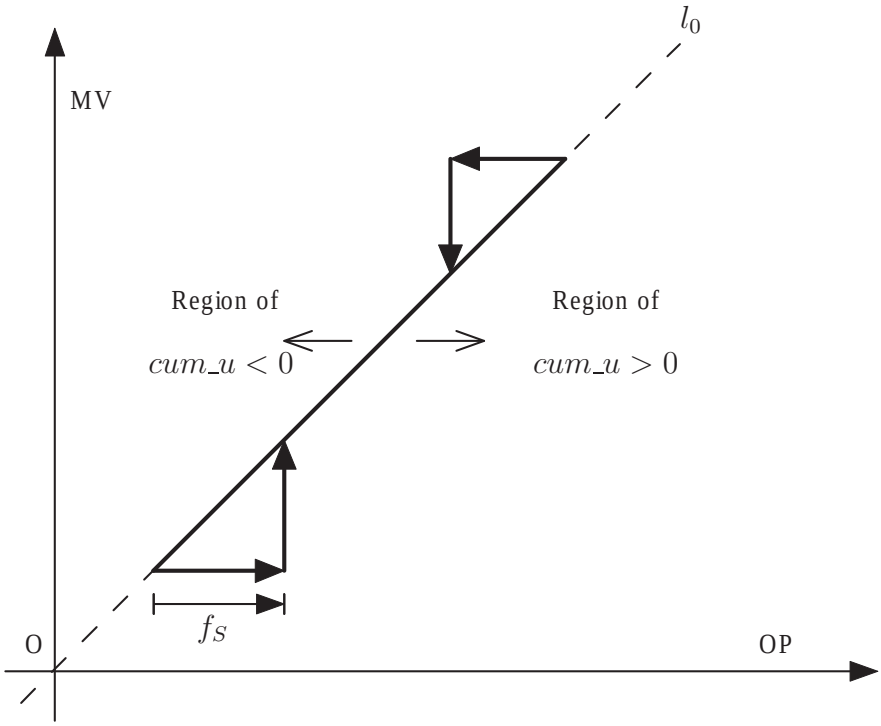

Figure 2.14: MV-OP plot of stiction with no offset pattern.

this chapter, as shown in Figure 2.11. This model extends the model proposed by He et al., which addresses all possible state transitions, as well as different stiction patterns. Define

$$u(k) = \begin{cases} 1 & \text{if } \tilde{u}(k) \geq 1; \\ 0 & \text{if } \tilde{u}(k) \leq 0; \\ \tilde{u}(k) & \text{otherwise,} \end{cases} \tag{2.5}$$

where $\tilde{u}(k)$ is the control signal in kth iteration, as degree of output span; while $u(k)$ is the actual control signal exerted on the valve, taking consideration of saturation effect. According to Figure 2.11, the model first updates the value of $cum\_u(k)$, additionally, the direction of movement $d(k)$ is obtained via $\text{sgn}(cum\_u(k))$ then, if $Stop = 1$, the logic flows to the left branch, which determines the position of the valve if it is stuck in the previous interval. The algorithm contained in the left branch is identical to He et al.

model. In other words, He et al. model is part of the complete model being proposed in this chapter. If $cum\_u(k)$ is large enough to overcome the static friction f_S, the valve position $u_v(k)$ will be the controller output $u(k)$ deducted by dynamic friction f_D. The $cum\_u(k)$ is updated to be equal to $\pm f_D$, since when valve starts slipping, the force being counteracted by friction is equal to $\pm f_D$ (the sign depends on the direction of movement $d(k)$). Additionally, the valve status flag *Stop* is updated to be 0 to indicate that the valve switches to a slipping mode. Otherwise, the valve remains in the previous position.

When the valve is in a slipping state, the condition to determine the status in the next instant depends on the sign of f_D, since the two pairs $\{f_S,\ f_D\}$ and $\{S,\ J\}$ have the following relationships [52],

$$f_S = (S + J)/2, \tag{2.6}$$

$$f_D = (S - J)/2. \tag{2.7}$$

The various stiction patterns corresponding to S and J are discussed in [27]. Note that $f_S > 0$ since $S > 0$ and $J > 0$. The MV-OP pattern corresponding to f_D can be summarized as follows:

- $f_D > 0$ (or $S > J$). Stiction with undershoot or pure deadzone.
- $f_D = 0$ (or $S = J$). Stiction with no offset or linear.
- $f_D < 0$ (or $S < J$). Stiction with overshoot.

Pure deadzone and linear pattern can be seen as special cases of stiction pattern with $f_S = f_D > 0$ and $f_S = f_D = 0$ accordingly. In what follows, the major three patterns: stiction with undershoot, no offset and overshoot are discussed separately.

The MV-OP plot of stiction with undershoot pattern is shown in Figure 2.12. The shading area in the MV-OP plane shows the region where $|cum\_u| > f_D$. From this figure, it can be observed that, if the valve is currently slipping, it will keep on slipping as long as $|cum\_u| > f_D$. Otherwise, it will change to stick mode. When the valve keeps on slipping, cum_u is updated to be $d(k) \times f_D$, while the actual valve displacement is the offset between input u and updated cum_u. When the valve changes to a stick mode, the valve remains in the previous position and the status parameter *Stop* is set to be 1.

Figure 2.13 gives the MV-OP plot of stiction with overshoot pattern. Similar to the undershoot case, the slipping valve will continue slipping as long as $|cum\_u|$ falls into the shading region, i.e., $|cum\_u| < -f_D$. In this case, the cum_u is updated by $d(k) \times (-f_D)$. The valve position is determined by the same equation as that in the undershoot pattern, in both cases of keeping slipping and starting sticking.

The stiction without offset pattern is somewhat special. Figure 2.14 shows the MV-OP plot in this case. The slipping valve will keep on slipping when the direction flag d has the same sign over two consecutive sampling intervals. Since in the slipping mode, there is no dynamic friction or $f_D = 0$, the cum_u is reset to be zero and the actual valve position $u_v = u$. The condition for determining the valve position when it changes from slip to stick is identical to previous two cases.

Combining the above three cases, the position of the valve when it is currently in a slipping mode can be summarized in the right branch of Figure 2.11. A complete, two-layer binary tree logic stiction model has been set up.

2.3 Simulation Study with the Proposed Stiction Model

2.3.1 Open-loop simulation

To verify the proposed model, the simulation results of open-loop MV-OP plots of the proposed models, under sinusoidal input, w.r.t. different f_S and f_D values are shown in Figure 2.15, which is identical to the simulation results of Kano et al. data-driven model [21] [52]. The simple data-driven model also shows similar behaviors with its physical counterpart [21] [27]. Moreover, the model can cover all the five patterns relating to the stiction, especially the linear pattern, which is not covered in [27].

2.3.2 Closed-loop simulation on a valve-controlled FOPDT system

As shown in Figure 2.5, to analyze the closed-loop behavior of FOPDT systems with sticky pneumatic control valve, the PI controller, data-driven model of valve and system model $G(s)$, form a negative feedback loop, under reference input of unit step $r(t) = U(t)$, where $C(s) = 0.1(s + 5)/s$, $G(s) = 3e^{-5s}/(5s + 1)$. The simulation results of controller output (OP) versus valve position (MV) are given in Figure 2.16, while their results of OP versus PV are given in Figure 2.17. The presence of stiction of the data-driven model causes the limit cycle of PV in steady state, similar to the situation with

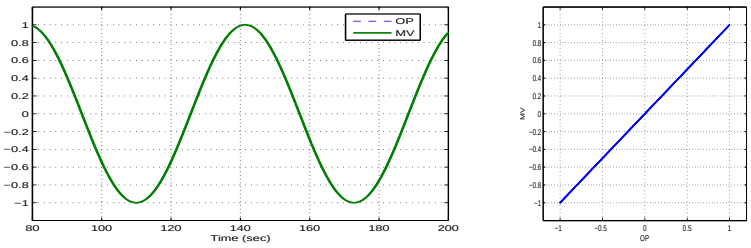

(a) Linear with $f_S = 0$ and $f_D = 0$.

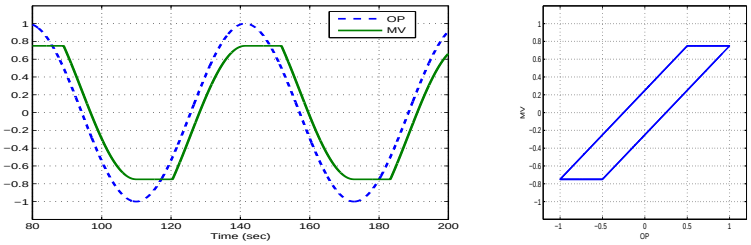

(b) Deadzone with $f_S = 0.25$ and $f_D = 0.25$.

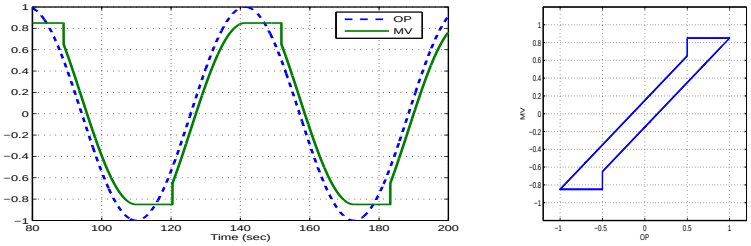

(c) Stiction (undershoot) with $f_S = 0.35$ and $f_D = 0.15$.

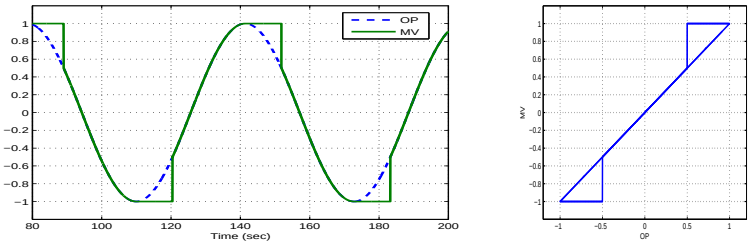

(d) Stiction (no offset) with $f_S = 0.5$ and $f_D = 0$.

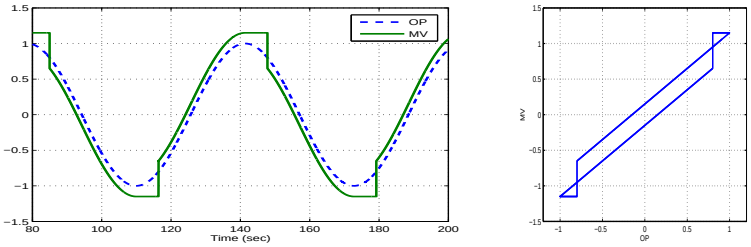

(e) Stiction (overshoot) with $f_S = 0.4$ and $f_D = -0.1$.

Figure 2.15: Open-loop response pattern of the new model with $u(t) = \sin(0.1t)$. Left column: OP / MV waveforms. Right column: MV-OP plot.

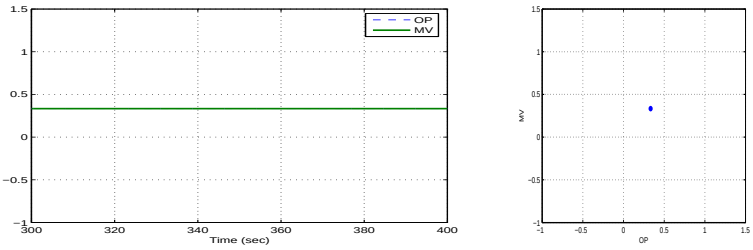

(a) Linear with $f_S = 0$ and $f_D = 0$.

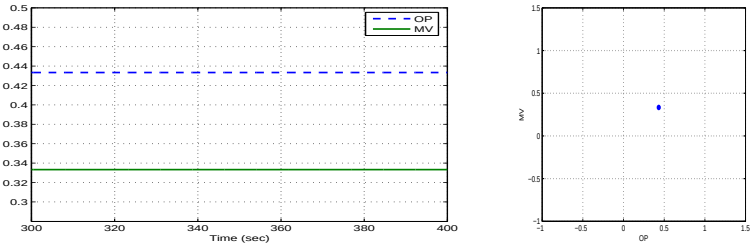

(b) Deadzone with $f_S = 0.25$ and $f_D = 0.25$.

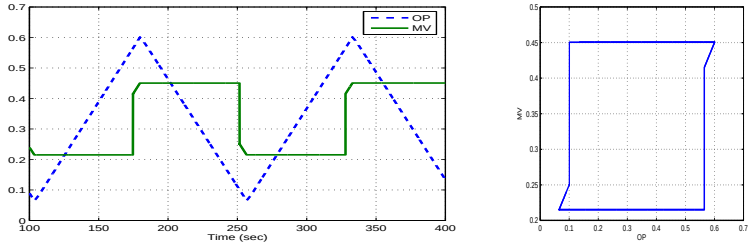

(c) Stiction (undershoot) with $f_S = 0.35$ and $f_D = 0.15$.

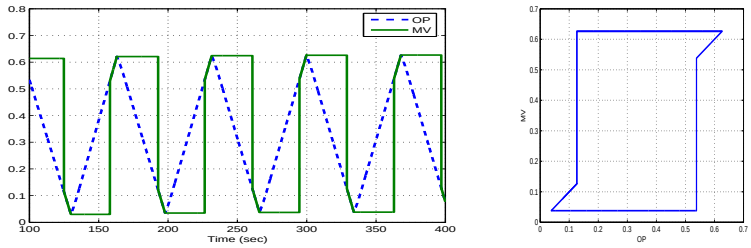

(d) Stiction (no offset) with $f_S = 0.5$ and $f_D = 0$.

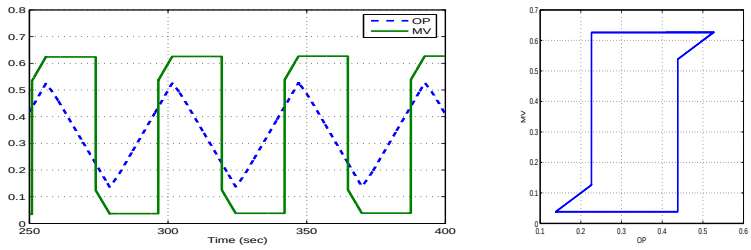

(e) Stiction (overshoot) with $f_S = 0.4$ and $f_D = -0.1$.

Figure 2.16: Closed-loop response pattern of the new model in a valve-controlled FOPDT system. Left column: OP / MV waveforms. Right column: MV-OP plot.

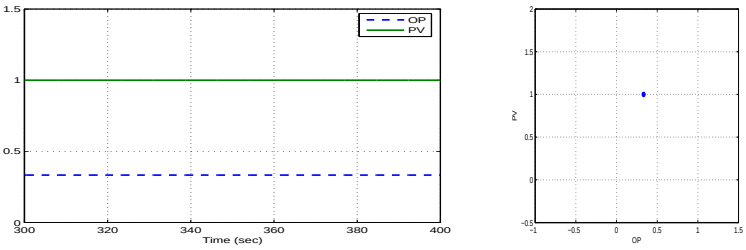

(a) Linear with $f_S = 0$ and $f_D = 0$.

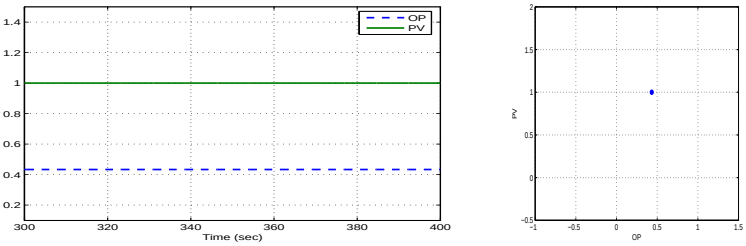

(b) Deadzone with $f_S = 0.25$ and $f_D = 0.25$.

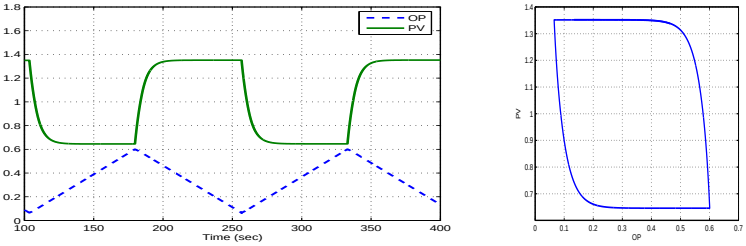

(c) Stiction (undershoot) with $f_S = 0.35$ and $f_D = 0.15$.

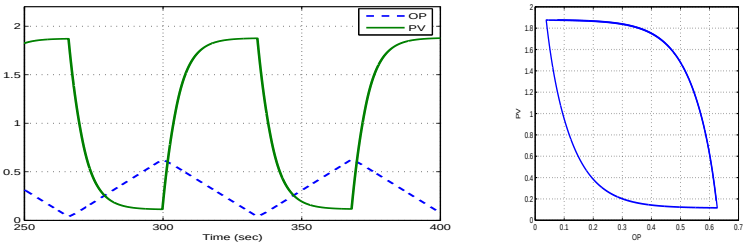

(d) Stiction (no offset) with $f_S = 0.5$ and $f_D = 0$.

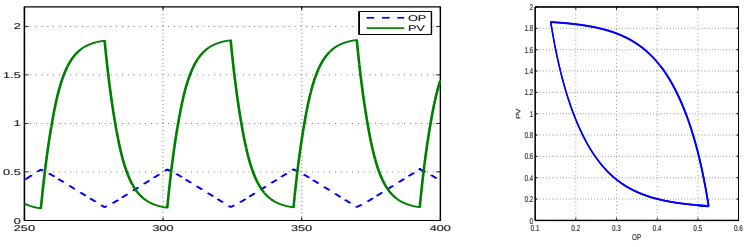

(e) Stiction (overshoot) with $f_S = 0.4$ and $f_D = -0.1$.

Figure 2.17: Closed-loop response pattern of the new model in a valve-controlled FOPDT system. Left column: OP / PV waveforms. Right column: PV-OP plot.

the physical model. Compared with the physical model in [21], [27], the most obvious difference is that the deadzone model does not excite limit cycles [68], since there is no integrator in the data-driven model. The PV-OP plots are also listed in Figure 2.17. Except the linear and deadzone cases, one can hardly tells the difference between the three categories of the stiction pattern from the elliptical PV-OP plot with sharp turn around. Generally speaking, the PV-OP plot is not a reliable diagnostic for valve faults, since the PV-OP plot ignores some nonlinearities due to low-pass properties of the system. Thus, if the valve position data is available, the use of MV-OP plot is encouraged. Otherwise, some qualitative stiction detection method may be used to analyze the stiction behavior [26].

2.3.3 Closed-loop simulation on a valve-controlled integral system

In this part, the closed-loop simulation is performed on a valve-controlled integral system $G(s) = 1/s$ with same stiction model, controller and reference input as the concentration loop. The results are shown in Figure 2.18 and 2.19. Compared with the earlier case of FOPDT system, it is observed that the limit cycle exists in the deadzone nonlinearity since there is at least one integrator in the overall system. The MV-OP plots clearly show various cases of valve nonlinearities, while the PV-OP plots show elliptical loops with sharp turns around. Similarly, the PV-OP plots are not reliable for valve diagnostics in level loops.

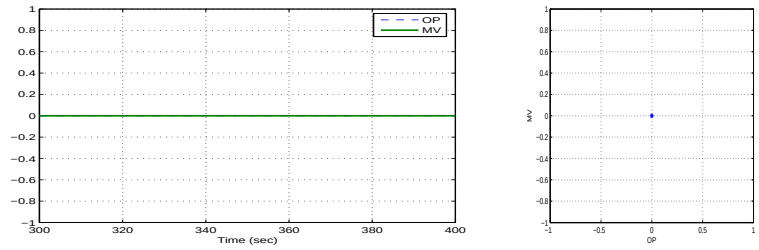

(a) Linear with $f_S = 0$ and $f_D = 0$.

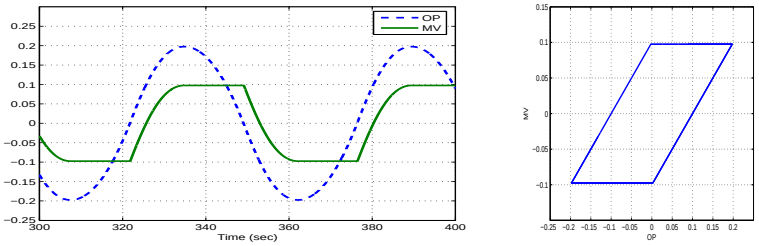

(b) Deadzone with $f_S = 0.25$ and $f_D = 0.25$.

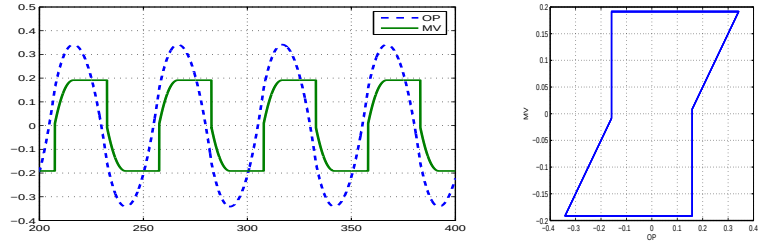

(c) Stiction (undershoot) with $f_S = 0.35$ and $f_D = 0.15$.

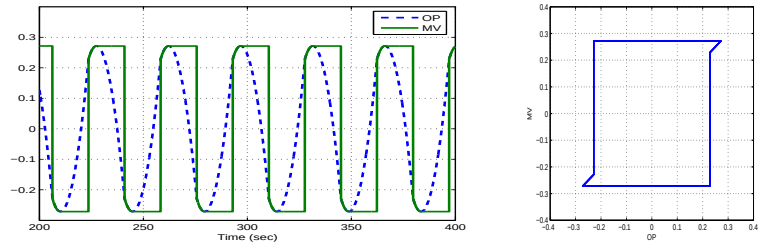

(d) Stiction (no offset) with $f_S = 0.5$ and $f_D = 0$.

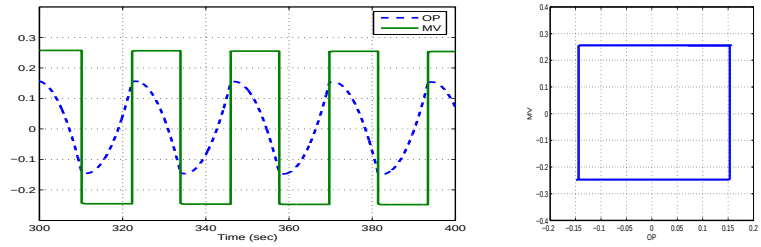

(e) Stiction (overshoot) with $f_S = 0.4$ and $f_D = -0.1$.

Figure 2.18: Closed-loop response pattern of the new model in a valve-controlled integral system. Left column: OP / MV waveforms. Right column: MV-OP plot.

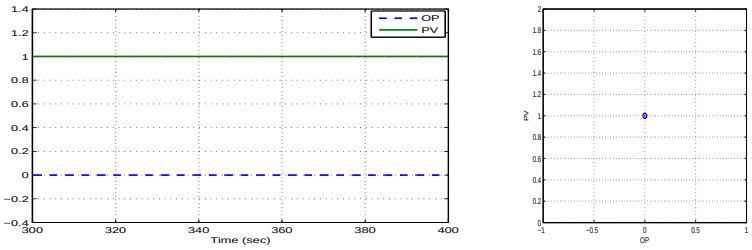

(a) Linear with $f_S = 0$ and $f_D = 0$.

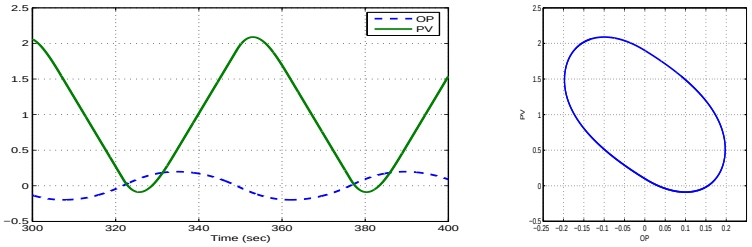

(b) Deadzone with $f_S = 0.25$ and $f_D = 0.25$.

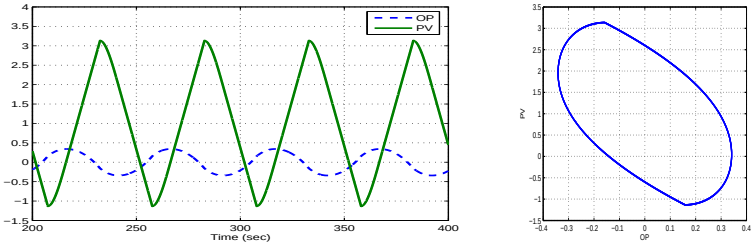

(c) Stiction (undershoot) with $f_S = 0.35$ and $f_D = 0.15$.

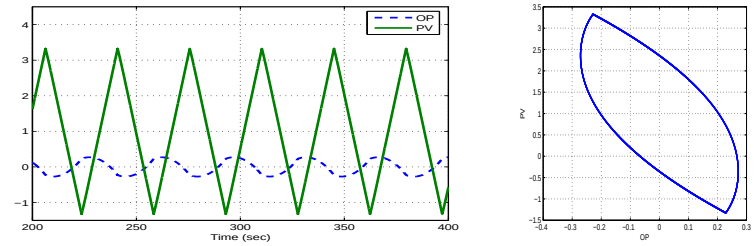

(d) Stiction (no offset) with $f_S = 0.5$ and $f_D = 0$.

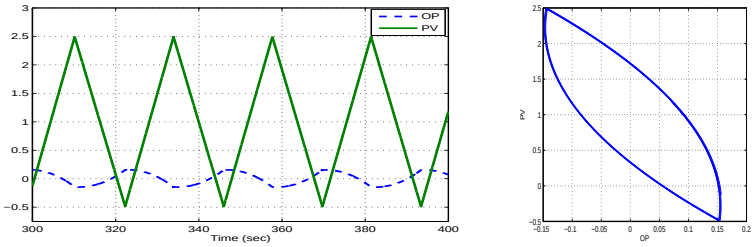

(e) Stiction (overshoot) with $f_S = 0.4$ and $f_D = -0.1$.

Figure 2.19: Closed-loop response pattern of the new model in a valve-controlled integral system. Left column: OP / PV waveforms. Right column: PV-OP plot.

2.4 Conclusion

In this chapter, several stiction models of control valve positioning systems proposed by earlier researchers are first reviewed and compared. Based on this, a simple, two-layer binary tree logic structure data-driven stiction model is proposed. It includes He et al. incomplete model as a part of the new model. It can describe various stiction patterns with only two external parameters, i.e., static friction f_S and dynamic friction f_D, which are closely related to the physical model. The open-loop and closed-loop simulation realized on different system models shows the correctness and effectiveness of the proposed stiction model. The data-driven stiction model can be used to replace the physical valve model for simulation and design to evaluate the performance of valve control systems in the presence of stiction.

Chapter 3

Friction-Impeded System Modeling by Analysis of a Class of Full State Relay Feedback Systems in Time Domain

3.1 Introduction

Relay control systems differ from continuous and sampled-data ones by the fact that they contain discontinuous relay elements. Due to their simplicity, quick action and considerable power amplification, the applications have been widely expanded to various domains of technology. In order to explain the motivations and illustrate the contributions more clearly, the literature reviews on analysis of relay feedback system are given first.

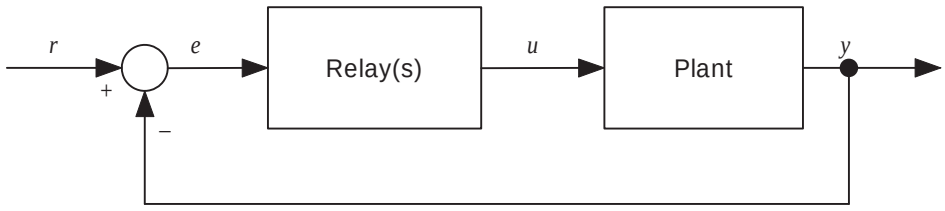

Figure 3.1: The simplest form of RFS.

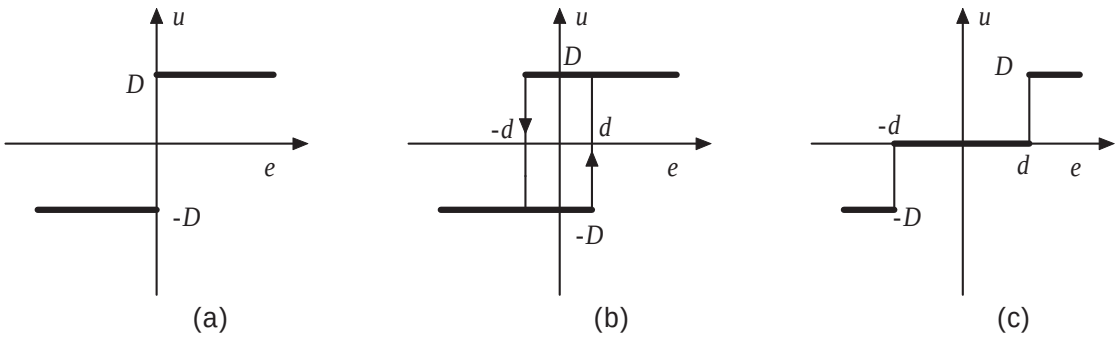

Figure 3.2: Variations of relay elements. (a) Relay without hysteresis. (b) Relay with hysteresis. (c) Relay with deadzone.

3.1.1 Review of relay feedback systems

Application of relay apparatus can be tracked back to 1950s, when it is used as amplifiers. In 1960s, relay feedback were firstly applied to adaptive control [98], an example is the adaptive missile roll control system proposed in [36]. The simplest form of relay feedback system is shown in Figure 3.1. The most important application of relay feedback system (RFS) is design of auto-tuners for PID controllers [9] [10] [105], where continuous cycling of controlled variable is generated from the relay experiment and the important model information can be directly extracted from it. Compared with the conventional Ziegler-Nicols tuning, the sustained oscillation generated in the relay experiment is in a control manner and a very efficient way, i.e. a one-shot solution. The simplicity of the tuning mechanism makes relay based auto-tuner a great success. The various of commonly used single relay elements are shown in Figure 3.2, including single-valued relay, hysteresis relay and deadzone relay. To increase the degree-of-freedom of tuning, dual-channel relay (DCR) feedback is developed in [35].

However, compared with other subfields of control engineering, theoretical develop-

ment of RFSs is far behind the practical applications. Phase-plane analysis is the classical technique which is applicable to investigate the existence and stability of limit cycles [42] of second-order systems. The analysis of RFS using describing function (DF) approximation has received great attention since 1960s [12] [36]. The DF is applicable to a rough estimation of location of limit cycles with harmonics balance conditions [83] and it has been extended to analyze the stability of limit cycles, as in [3]. Control auto-tuners have been developed based on the identification of ultimate gain and frequency with a DF approach, resulting in an inaccurate estimation of critical point under some circumstance. In order to overcome the above weaknesses, the Tsypkin locus is introduced by describing the nonlinearities with infinite series of frequency components [98]. The Tsypkin locus is further applied to investigate the force oscillations and subharmonic oscillations in simple first-order-plus-dead-time (FOPDT) systems [60].

On the other hand, the time-domain methods for investigation of RFSs are based on the analysis of differential equations (DEs) with discontinuous terms [34]. These special kinds of DEs may exhibit such phenomena as non-uniqueness of solutions, chattering, fast switching, sliding modes, bifurcations and chaos. The existence of solutions had been studies for systems having input-output forms in [37]. It is known that relay feedback systems often possess limit cycles. However, establishing the exact conditions for existence of limit cycles only limits to certain kinds of RFSs till today. The stability of limit cycles is another important issue since most applications of RFSs are based on stable limit cycle oscillations. The elegant criteria for the local stability of limit

cycles are investigated in [8] [63] by perturbations of the Poincare map. In [39], a method to compute the bound of local stability is given. The limit cycle stability for more complicated patterns such as sliding motions is further investigated in [51]. If the system starts from arbitrary set point, the RFS will be driven to converge to the periodic motions, then the RFS has the global stability of limit cycle. The study of the global stability of RFS with two switchings per period is given in [40]. The complete discussion of hysteresis relay feedback of certain linear systems, including of FOPDT and second-order type-1 systems are discussed in [61] [100] [104].

3.1.2 Motivations and novelty of new method

In recent years, the relay feedback approach has also been extended beyond tuning of controllers to the identification of commonly encountered nonlinearities in practical systems, such as friction [7] [15] [23] [92]. The properties of limit cycle oscillations generated due to friction are further investigated in [66] [73]. In [23] [55] [92], friction models are identified based on the DF analysis. A two-relay configuration is used in [15], where inner and outer relays switch asynchronously, to generate oscillations based on which a Coulomb friction model is identified. However, this approach requires open-loop and closed-loop two-phase identification with multiple sets of experiment data. Step response analysis is used in their works along with recursive least square for identification of the model parameters, while the characteristics of relay switchings have not been fully utilized for system modeling.

For systems involving multiple relays, there remain open issues to address and resolve,

including switching conditions, locations and stability of limit cycles under specific forms of multiple relays feedback. In this chapter, a class of linear systems under a triple-relay feedback will be analyzed. The locations and the stability of limit cycles arising from this system will be discussed in Section 3.2. This class of systems relates directly to servo-mechanical system operating with Coulomb friction under Dual-Channel Relay (DCR) feedback [35] [92]. Thus, the analysis results are leveraged on to fulfill an application to identify the friction parameter as well as system dynamics via limit cycle analysis in the time-domain. In this new method proposed, by observation of critical switching points in limit cycle oscillation, it is able to numerically solve all the system model parameters within just one single relay experiment data. In addition, it releases the requirement of having a sinusoidal-like output signal associated with DF-based identification method as in [23] [55] [92]. Simulation examples and real-time experiments show the practical appeal of the proposed methods.

3.2 Triple-Relay Feedback System

The configuration of triple-relay feedback system is shown in Figure 3.3. The linear system is essentially a third-order system comprising of a first-order portion $\dot{y} = \alpha y + \beta u$, in series with two integrators. Three feedback relays RA, RB and RC are connected to each state of the system. This configuration relates to a typical servomechanical system experiencing Coulomb friction, under deliberate DCR feedback as will be shown in [92].

Set $x_1 = y$, $x_2 = \int_0^t (x_1)\,\mathrm{d}t$, $x_3 = \int_0^t (x_2)\,\mathrm{d}t$. Under triple-relay feedback, the effective

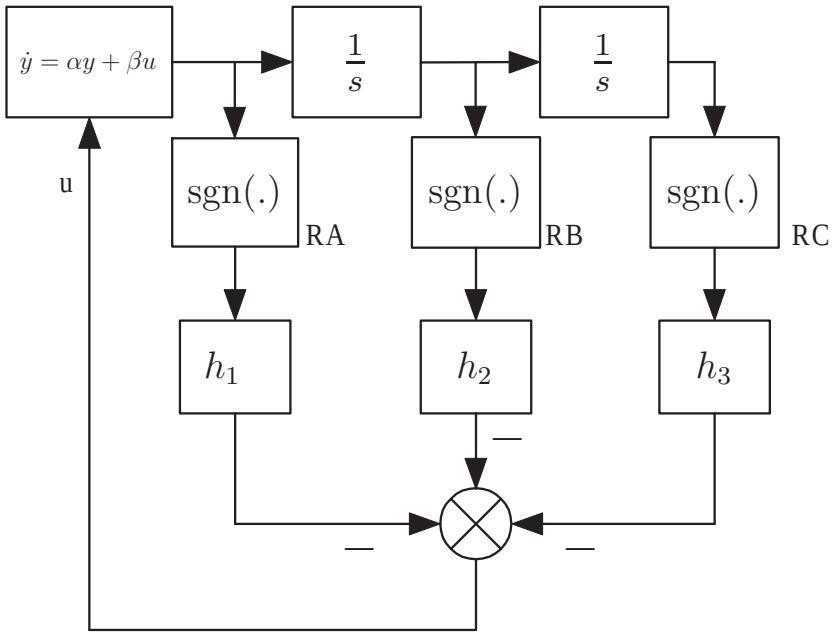

Figure 3.3: System under triple-relay feedback apparatus: standard form.

control signal u is governed by the following equation,

$$u(t) = -h_1 \text{sgn}(x_1) - h_2 \text{sgn}(x_2) - h_3 \text{sgn}(x_3). \tag{3.1}$$

By defining the augmented state vector $x = [x_3, x_2, x_1]^{\text{T}}$, the augmented state-space form of the linear portion of the system can be represented as

$$\dot{x} = Ax + Bu, \tag{3.2}$$

$$x_1 = C_1 x, \tag{3.3}$$

$$x_2 = C_2 x, \tag{3.4}$$

$$x_3 = C_3 x, \tag{3.5}$$

where

$$A = \begin{bmatrix} 0 & 1 & 0 \\ 0 & 0 & 1 \\ 0 & 0 & \alpha \end{bmatrix}, \tag{3.6}$$

$$B = \begin{bmatrix} 0 \\ 0 \\ \beta \end{bmatrix}, \tag{3.7}$$

$$C_1 = \begin{bmatrix} 0 & 0 & 1 \end{bmatrix}. \tag{3.8}$$

$$C_2 = \begin{bmatrix} 0 & 1 & 0 \end{bmatrix}, \tag{3.9}$$

$$C_3 = \begin{bmatrix} 1 & 0 & 0 \end{bmatrix}. \tag{3.10}$$

Meanwhile, note that $x_2 = \dot{x}_3 = C_3\dot{x} = C_3Ax + C_3Bu = C_3Ax$. Similarly, $x_1 = C_1A^2x$. Thus, $C_2 = C_3A$, and $C_1 = C_3A^2$.

In the ensuing sections, the switching conditions, locations and stability of limit cycles arising from the configuration of Figure 3.3 will be analyzed. These are fundamental issues which need to be addressed to better facilitate the subsequent application to system modeling.

3.2.1 Locations of limit cycles in triple-relay feedback systems

The study of the limit cycle oscillations arising from the triple-relay feedback system of Figure 3.3 will be restricted to the case of *simple* oscillation, which is defined as one comprising of switching due to a relay is followed by one and only one switching from the other relays before its next switch. This restriction is also usually referred to as the *condition of no additional switching* [98].

Define the switching plane where the outputs of the three relays change as $S_1 := \{x :$

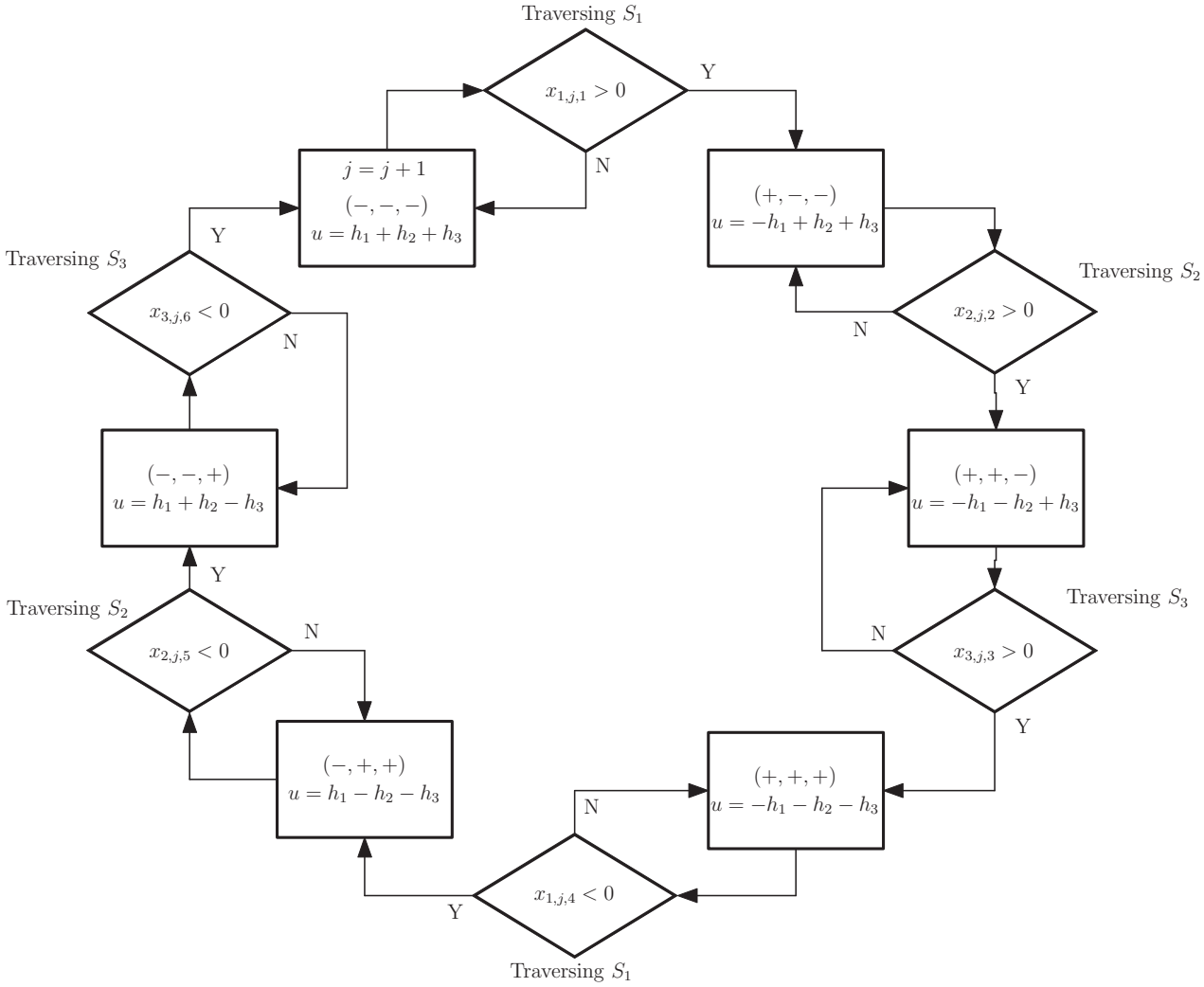

Figure 3.4: Sequence of switching arising from the triple-relay feedback.

$C_1x = 0\}$, $S_2 := \{x : C_2x = 0\}$, and $S_3 := \{x : C_3x = 0\}$. Since x_1 leads x_2 by a phase of $\pi/2$ and x_2 leads x_3 by the same amount, relays RA, RB and RC will switch sequentially within a half period of periodic oscillations. Thus, the assumption of simple oscillations is reasonable when the system goes into steady state oscillation. Under this condition, since the control u arises from three branches of switching sources, and every branch contributes two possible values, there are six possible states during the steady state oscillation.

The following theorem determines the location of limit cycles in the triple-relay feedback system.

Theorem 3.1. *For the augmented state-space system in the form (3.2)∼(3.8) under feedback (3.1), if there exists an odd symmetric and periodic trajectory with period* $T = 2l^* = 2(l_1 + l_2 + l_3)$*, and the trajectory traverses planes* S_3*,* S_1 *and* S_2 *at* $t = 0$*,* $t = l_1$*, and* $t = l_1 + l_2$ *accordingly with initial condition* $x_1(0^+) < 0$*,* $x_2(0^+) < 0$ *and* $x_3(0^+) < 0$*, then* l_1*,* l_2 *and* l_3 *are given by*

$$f_1(l_1, l_2, l_3) = C_1(I + \Phi^*)^{-1}(\Gamma_1 u_1 - \Phi_1\Phi_3\Gamma_2 u_2 - \Phi_1\Gamma_3 u_3) = 0, \tag{3.11}$$

$$f_2(l_1, l_2, l_3) = C_2(I + \Phi^*)^{-1}(\Phi_2\Gamma_1 u_1 + \Gamma_2 u_2 - \Phi_1\Phi_2\Gamma_3 u_3) = 0, \tag{3.12}$$

$$f_3(l_1, l_2, l_3) = C_3(I + \Phi^*)^{-1}(\Phi_2\Phi_3\Gamma_1 u_1 + \Phi_3\Gamma_2 u_2 + \Gamma_3 u_3) = 0. \tag{3.13}$$

subject to $I + \Phi^*$ *being non-singular, where*

$$\Phi_j = e^{Al_j} \quad \forall \quad j = 1, 2, 3, \tag{3.14}$$

$$\Gamma_j = \int_0^{l_j} e^{A\tau} B \, \mathrm{d}\tau \quad \forall \quad j = 1, 2, 3, \tag{3.15}$$

$$\Phi^* = \prod_{i=1}^{3} \Phi_i. \tag{3.16}$$

The control $u_j \ \forall \ j = 1, 2, 3$ *at the three stages within half of the period, are respectively given by*

$$u_1 = h_1 + h_2 + h_3, \tag{3.17}$$

$$u_2 = -h_1 + h_2 + h_3, \tag{3.18}$$

$$u_3 = -h_1 - h_2 + h_3. \tag{3.19}$$

Furthermore, the solution $x(t)$ *must satisfy the following conditions within the time interval* $(0, 2l^*)$*:*

$$x_1(t) = C_1 x(t) \begin{cases} < 0 & for \quad 0 < t < l_1 \ and \ l_1 + l^* < t < 2l^* \\ > 0 & for \quad l_1 < t < l_1 + l^* \end{cases}, \tag{3.20}$$

$$x_2(t) = C_2 x(t) \begin{cases} < 0 & for \quad 0 < t < l_2 \ and \ l_2 + l^* < t < 2l^* \\ > 0 & for \quad l_2 < t < l_2 + l^* \end{cases}, \tag{3.21}$$

$$x_3(t) = C_3 x(t) \begin{cases} < 0 & for \quad 0 < t < l^* \\ > 0 & for \quad l^* < t < 2l^* \end{cases}. \tag{3.22}$$

Proof of Theorem 3.1. Note that the trajectory will traverse S_3 at $t = l_1 + l_2 + l_3$ again by symmetry. Define $x_{i,j,k}$ as the value of x_i at the kth switching instant of the jth period of oscillation. Then, under the condition of no additional switching, the sequential chart of switching instants and variation of relative parameters is depicted in Figure 3.4. In this

figure, for simplicity, $x_1 < 0$, $x_2 < 0$ and $x_3 < 0$ are simply abbreviated as $(-,-,-)$. In this way, the state variable x for different switching states is listed for ease of analysis. The traversing points $x_{i,j,k}$ in system (3.2)$\sim$(3.8) are related to $x_{i,j+1,k}$ by the same function P, w.r.t. the same k:

$$x_{i,j+1,k} = P\left(x_{i,j,k}\right). \tag{3.23}$$

In fact, P is the Poincaré Map [42] on the switching plane S_1 (or S_2 or S_3). In the case of *periodic oscillations*, the traversing point x^* of the trajectory with S_1 is fixed. Furthermore, if the periodic oscillation is odd symmetric, $x_{1,j,m} = -x_{1,j,m+3}$, $\forall m = 1,2,3$. Similar properties exist for other switching planes S_2 and S_3.

The solution $x(t)$ for $0 < t \leq l_1$ with control u_1 and initial condition $x(0)$ is given by $x(t) = e^{At}x(0) + \int_0^t e^{A(t-\tau)}B\,\mathrm{d}\tau u_1$. For simplicity, set $x(0) = a$, $x(l_1) = b$, and $x(l_1 + l_2) = c$. Thus, at $t = l_1$, $b = e^{Al_1}a + \int_0^{l_1} e^{A\tau}B\,\mathrm{d}\tau u_1$ which can be simply written as

$$b = \Phi_1 a + \Gamma_1 u_1. \tag{3.24}$$

Inferring from the symmetric property of oscillation, $x(l^*) = -x(0) = -a$. Then, considering the time intervals $l_1 < t < l_1 + l_2$, and $l_1 + l_2 < t < l^*$, it follows that

$$c = \Phi_2 b + \Gamma_2 u_2, \tag{3.25}$$

$$-a = \Phi_3 c + \Gamma_3 u_3, \tag{3.26}$$

where Φ_j, Γ_j, u_j $\forall j = 1,2,3$ are defined in (3.14)$\sim$(3.19). Note that Φ_1, Φ_2 and Φ_3 commutes. (3.17)$\sim$(3.19) can be obtained from Figure 3.4 under the simple oscillation condition.

Solving the equation set (3.24)∼(3.26) yields

$$a = -(I+\Phi^*)^{-1}(\Phi_2\Phi_3\Gamma_1 u_1 + \Phi_3\Gamma_2 u_2 + \Gamma_3 u_3), \tag{3.27}$$

$$b = (I+\Phi^*)^{-1}(\Gamma_1 u_1 - \Phi_1\Phi_3\Gamma_2 u_2 - \Phi_1\Gamma_3 u_3), \tag{3.28}$$

$$c = (I+\Phi^*)^{-1}(\Phi_2\Gamma_1 u_1 + \Gamma_2 u_2 - \Phi_1\Phi_2\Gamma_3 u_3). \tag{3.29}$$

Conditions $x_1(l_1) = 0$, $x_2(l_1 + l_2) = 0$ and $x_3(l^*) = 0$ will give rise to the equations (3.11)∼(3.13). Equations (3.20)∼(3.22) can be obtained from Figure 3.4, which shows the change of signs of key state variables at the switching instants. The above theorem is given to allow numerical computation of the duration l_1, l_2 and l_3 of the three stages of half period of oscillation, so that the locations of the limit cycles can be determined. Compared to DF analysis which can only approximate the period of the resultant limit cycle, Theorem 3.1 is able to provide the exact time duration between two consecutive switchings in the triple-relay feedback system.

3.2.2 Local stability of limit cycles in triple-relay feedback systems

In practical application, only the stable limit cycles are useful for autotuning and system modeling since they need to be immune to random noise and perturbation. In Section 3.2.1, the limit cycles have been located for a class of relay feedback system. For further investigating their local stability, the Jacobian W^2 of the Poincaré map P is imported. Physically, it shows the variation of states after one period of oscillation w.r.t. the perturbed initial states. For the case of odd symmetric oscillation, the Jacobian W

w.r.t. half of the period suffices for the analysis, while the Jacobian w.r.t. the full period is given by W^2.

The following theorem gives the expression for W and the condition for local stability of limit cycles.

Theorem 3.2. *Under condition of no additional switching, the Jacobian W^2 of the Poincaré map P is given by*

$$W = \left(I - \frac{v_3 C_3}{C_3 v_3}\right) \Phi_3 \left(I - \frac{v_2 C_2}{C_2 v_2}\right) \Phi_2 \left(I - \frac{v_1 C_1}{C_1 v_1}\right) \Phi_1, \tag{3.30}$$

where $v_1 = Ab + Bu_1$, $v_2 = Ac + Bu_2$, and $v_3 = -Aa + Bu_3$, with various notations in Theorem 3.1 are inherited. The limit cycle is locally stable iff all the eigenvalues of W are inside the unit circle.

Proof: Consider a trajectory with initial condition $x(0) = a$. If the initial value a varies within the switching plane S_3 by δa, i.e., $C_3(a + \delta a) = 0$. If $x(t)$ reaches the switching plane S_1 at time l_1 and the control signal $u(t) = u_1$ for $t \in (0, l_1)$, it yields

$$x(l_1) = e^{Al_1}(a + \delta a) + \int_0^{l_1} e^{A(l_1 - \tau)} B u_1 \, \mathrm{d}\tau. \tag{3.31}$$

Set $F(l_1) = e^{Al_1}(a + \delta a)$, $G(l_1) = \int_0^{l_1} e^{A(l_1-\tau)} B u_1 \, \mathrm{d}\tau$, so that $x(l_1) = F(l_1) + G(l_1)$.

If $x(t)$ reaches the switching plane S_1 at time $l_1 + \delta l_1$, i.e., some perturbations exist due to the variation of initial conditions,

$$\begin{aligned} x(l_1 + \delta l_1) &= e^{A(l_1 + \delta l_1)}(a + \delta a) + \int_0^{l_1 + \delta l_1} e^{A(l_1 + \delta l_1 - \tau)} B u_1 \, \mathrm{d}\tau \\ &= F(l_1 + \delta l_1) + G(l_1 + \delta l_1). \end{aligned} \tag{3.32}$$

The following properties are useful for further analysis:

$$\int_0^t e^{A(t-\tau)}\,\mathrm{d}\tau = \int_0^t e^{A\tau}\,\mathrm{d}\tau, \tag{3.33}$$

$$A\int_0^t e^{A\tau}\,\mathrm{d}\tau = e^{At} - I, \tag{3.34}$$

$$Ae^{At} = e^{At}A. \tag{3.35}$$

Using a first-order Taylor series expansion, together with (3.33)$\sim$(3.35), it yields

$$\begin{aligned} F(l_1 + \delta l_1) &= F(l_1) + \frac{\partial}{\partial l_1}F(l_1)\,\delta l_1 + O(\delta^2) \\ &= e^{Al_1}(a + \delta a) + e^{Al_1}A\,\delta l_1(a + \delta a) + O(\delta^2) \\ &= \Phi_1(I + A\,\delta l_1)(a + \delta a) + O(\delta^2). \end{aligned}$$

$$\begin{aligned} G(l_1 + \delta l_1) &= G(l_1) + \frac{\partial}{\partial l_1}G(l_1)\,\delta l_1 + O(\delta^2) \\ &= \Gamma_1 u_1 + \frac{\partial}{\partial l_1}\left(\int_0^{l_1} e^{A\tau}\,\mathrm{d}\tau B u_1\right)\delta l_1 + O(\delta^2) \\ &= \Gamma_1 u_1 + \left(e^{Al_1} - I\right)Bu_1\,\delta l_1 + Bu_1\,\delta l_1 + O(\delta^2) \\ &= (I + A\,\delta l_1)\Gamma_1 u_1 + Bu_1\,\delta l_1 + O(\delta^2). \end{aligned}$$

Thus,

$$\begin{aligned} x(l_1 + \delta l_1) &= \Phi_1(I + A\,\delta l_1)(a + \delta a) + (I + A\,\delta l_1)\Gamma_1 u_1 + Bu_1\,\delta l_1 + O(\delta^2) \\ &= b + \Phi_1\,\delta a + (Ab + Bu_1)\,\delta l_1 + O(\delta^2). \end{aligned} \tag{3.36}$$

Set $v_1 = \dot{x}(l_1) = Ab + Bu_1$, which is the velocity of the trajectory at time l_1. Since $x(l_1 + \delta l_1)$ is on the switching plane S_1, $C_1 x(l_1 + \delta l_1) = 0$. By ignoring the higher order terms $O(\delta^2)$,

$$C_1\Phi_1\,\delta a + C_1 v_1\,\delta l_1 = 0.$$

Note that the condition

$$C_1 v_1 > 0 \tag{3.37}$$

must hold to satisfy the switching direction condition if there is a symmetric limit cycle. Hence,

$$\delta l_1 = -\frac{C_1 \Phi_1}{C_1 v_1}\, \delta a. \tag{3.38}$$

Substituting (3.38) into (3.36), it follows that

$$x(l_1 + \delta l_1) = b + \left(I - \frac{v_1 C_1}{C_1 v_1} \right) \Phi_1\, \delta a + O(\delta a^2). \tag{3.39}$$

Similarly, consider the time interval $t \in (l_1, l_1 + l_2)$, the trajectory starts at $x(l_1) = b$ on S_1 and eventually reaches $x(l_1 + l_2) = c$ on S_2, under the control torque u_2. Similar to the previous interval, the final state $x(l_1 + l_2)$ is investigated with perturbation corresponding to the initial condition b with a small variation δb, yielding

$$x(l_1 + \delta l_1 + l_2 + \delta l_2) = c + \left(I - \frac{v_2 C_2}{C_2 v_2} \right) \Phi_2\, \delta b + O(\delta b^2), \tag{3.40}$$

where $v_2 = \dot{x}(l_1 + l_2) = Ac + Bu_2$. The switching direction is given by

$$C_2 v_2 > 0. \tag{3.41}$$

In the same way, within the time interval $t \in (l_1 + l_2, l_1 + l_2 + l_3)$, the trajectory starts at $x(l_1 + l_2) = c$ on S_2 and eventually reaches $x(l_1 + l_2 + l_3) = -a$ on S_3, under the control torque u_3. Thus,

$$x(l_1 + \delta l_1 + l_2 + \delta l_2 + l_3 + \delta l_3) = -a + \left(I - \frac{v_3 C_3}{C_3 v_3} \right) \Phi_3\, \delta c + O(\delta c^2), \tag{3.42}$$

where $v_3 = \dot{x}(l_1 + l_2 + l_3) = -Aa + Bu_3$. The switching direction is given by

$$C_3 v_3 > 0. \tag{3.43}$$

From (3.39) and (3.40),

$$\delta b = \left(I - \frac{v_1 C_2}{C_2 v_1}\right) \Phi_1 \, \delta a, \tag{3.44}$$

$$\delta c = \left(I - \frac{v_2 C_3}{C_3 v_2}\right) \Phi_2 \, \delta b. \tag{3.45}$$

Substitute (3.44)$\sim$(3.45) into (3.42), it follows

$$x(l_1 + \delta l_1 + l_2 + \delta l_2 + l_3 + \delta l_3) = -a + W \, \delta a + O(\delta^2), \tag{3.46}$$

where the Jacobian W w.r.t. half period of oscillation is given by

$$W = \left(I - \frac{v_3 C_3}{C_3 v_3}\right) \Phi_3 \left(I - \frac{v_2 C_2}{C_2 v_2}\right) \Phi_2 \left(I - \frac{v_1 C_1}{C_1 v_1}\right) \Phi_1.$$

Similar to the analysis in [8], the limit cycle is stable if and only if $|\lambda(W)| < 1$.

Remark 3.1. *One eigenvalue of the matrix* $(I - v_1 C_1 / C_1 v_1)\Phi_1$ *is zero with right eigenvector* $\Phi_1^{-1} v_1$.

This states that the perturbation in the velocity of the state at time $l_1 + \delta l_1$ due to δa is removed. Thus, it guarantees that the trajectory is just traversing the switching plane S_1 at $t = l_1 + \delta l_1$. Similar properties can be extended to the matrices $(I - v_2 C_2 / C_2 v_2)\Phi_2$ and $(I - v_3 C_3 / C_3 v_3)\Phi_3$.

For convenience, set $W_1 = (I - v_1 C_1 / C_1 v_1)\Phi_1$, $W_2 = (I - v_2 C_2 / C_2 v_2)\Phi_2$ and $W_3 = (I - v_3 C_3 / C_3 v_3)\Phi_3$. Hence, $W = W_3 W_2 W_1$, and the following remarks can be stated.

Remark 3.2. *$|\lambda(W)| < 1$ does not imply that $|\lambda(W_1)|$, $|\lambda(W_2)|$, $|\lambda(W_3)|$ are all within the unit circle.*

Remark 3.2 states that although the condition of having eigenvalues of W_1, W_2 and W_3 within the unit circle is sufficient for stability of limit cycles, it can be hardly satisfied in most cases. In other words, even if some (or all) eigenvalues of W_1, W_2 or W_3 are outside the unit circle, all eigenvalues of W may still within the unit circle. Physically, the triple-relay feedback system can be seen as a switching system. The stable of the overall trajectory need not be granted by the stability of individual segment.

Remark 3.3. $\lambda(W_3W_2W_1) = \lambda(W_1W_3W_2) = \lambda(W_2W_3W_1)$.

Remark 3.3 states that the result of stability of limit cycle is independent of initial point on the trajectory of a certain limit cycle.

A systematic set of procedures has thus been realized for examining the stability of limit cycles arising in the three-relay feedback systems, and they are summarized as follows:

1. Find l_1, l_2 and l_3 by Theorem 3.1, check the conditions of (3.20)$\sim$(3.22).

2. Compute v_1, v_2, v_3 and check the conditions of (3.37), (3.41) and (3.43).

3. Compute W and verify $|\lambda(W)| < 1$ by Theorem 3.2.

3.2.3 Simulation and discussions

Example 3.1. *Consider a system $\dot{x} = -2x + 20u$, under the triple-relay feedback as in Figure 3.3, where $h_1 = 1$, $h_2 = 5$ and $h_3 = 3$.*

The augmented system can be represented as $\dot{x} = Ax + Bu$, and $[x_1, x_2, x_3]^{\mathrm{T}} = [C_1, C_2, C_3]^{\mathrm{T}} x$, where

$$A = \begin{bmatrix} 0 & 1 & 0 \\ 0 & 0 & 1 \\ 0 & 0 & -2 \end{bmatrix}, \quad B = \begin{bmatrix} 0 \\ 0 \\ 20 \end{bmatrix},$$

$$C_3 = \begin{bmatrix} 1 & 0 & 0 \end{bmatrix}, \quad C_2 = \begin{bmatrix} 0 & 1 & 0 \end{bmatrix}, \quad C_3 = \begin{bmatrix} 0 & 0 & 1 \end{bmatrix}.$$

Numerical calculations with Theorem 3.1 gives only one set of positive solutions $l_1 = 0.0147$, $l_2 = 0.2777$ and $l_3 = 0.3022$ for (3.11)$\sim$(3.13). Thus, the limit cycle has period $T = 2(l_1 + l_2 + l_3) = 1.1892$. Furthermore,

$$a = \begin{bmatrix} 0 \\ -4.5029 \\ -2.6903 \end{bmatrix}, \quad b = \begin{bmatrix} -0.0667 \\ -4.5226 \\ 0 \end{bmatrix}, \quad c = \begin{bmatrix} -0.8854 \\ 0 \\ 29.8282 \end{bmatrix},$$

and

$$C_3 v_3 = 4.5029, \quad C_2 v_2 = 29.8282, \quad C_1 v_1 = 180.0097.$$

The Jacobian of the Poincaré map can be computed from Theorem 3.2 as

$$W = \begin{bmatrix} 0 & 0 & 0 \\ -0.5975 & -0.7249 & -0.0250 \\ 14.5198 & 1.2994 & 0.3715 \end{bmatrix}.$$

The eigenvalues of W are 0, -0.6944 and 0.3410. It can be concluded that the limit cycle is locally stable with period $T = 1.1892$ according to Theorem 3.2. In addition, although W_1, W_2 and W_3 all have at least one eigenvalue outside the unit circle, all the eigenvalues of W are still within the unit circle.

The trajectory of the limit cycle and its projections on the $x_1 - x_2$, $x_2 - x_3$ and $x_1 - x_3$ planes are shown in Figure 3.5.

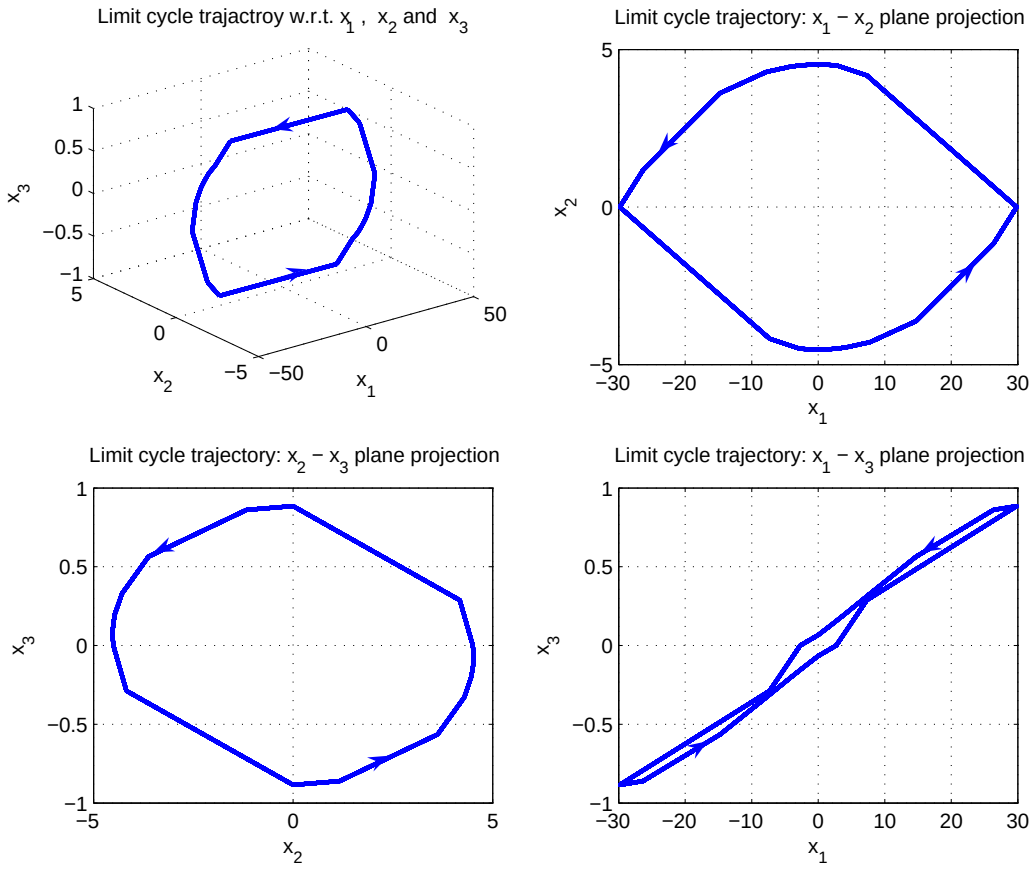

Figure 3.5: Trajectory of state variables in the limit cycle.

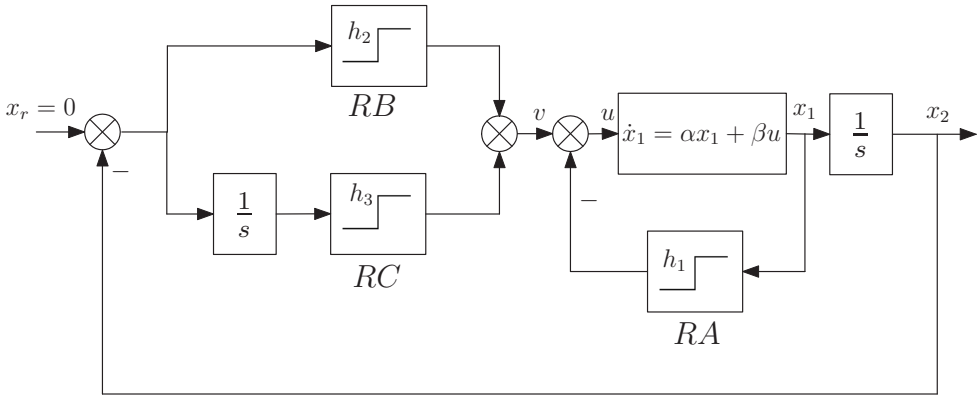

Figure 3.6: Servo-mechanical system with friction under DCR feedback.

3.3 System Modeling using Limit Cycle's Locations

The configuration of Figure 1 is akin to a servo-mechanical system experiencing Coulomb friction under deliberate dual-channel relay (DCR) feedback . The DCR is first proposed in [35], and it is used for the identification of a friction model within a typical servo-mechanical system configuration [92] via relay experiments. It consists of a parallel intentional relay construct acting on the linear portion of the dynamic system. The second feedback relay RC, which is cascaded to an integrator, provides a second degree of freedom to adjust the frequency of oscillation and ensure that the phase lag of the oscillation does not exceed π.

3.3.1 Modeling methodology

As shown in Figure 3.6, a typical second order linear positioning system

$$\dot{x}_1 = \alpha x_1 + \beta u; \tag{3.47}$$

$$\dot{x}_2 = x_1 \tag{3.48}$$

experiencing the effect of the Coulomb friction $f = h_1\text{sgn}(x_1)$, under the intentional DCR feedback apparatus [35] [92]

$$v = -h_2\text{sgn}(x_2) - h_3\text{sgn}(x_3). \tag{3.49}$$

where $\dot{x}_3 = x_2$, is equivalent to the three-relay feedback system which is discussed in the previous section. The actual control signal u fed to the linear system is

$$u = v - f = -h_1\text{sgn}(x_1) - h_2\text{sgn}(x_2) - h_3\text{sgn}(x_3). \tag{3.50}$$

The describing function based modeling technique is applied in [92] by simply assuming the position signal has a sinusoidal form, an assumption which ceases to be valid when better accuracy is required. In this proposed new method, instead of using the overall period of fundamental harmonic, the switching behavior of limit cycle will be leveraged to identify the system parameters based on the location of resultant limit cycles according to Theorem 3.1.

In the position feedback system under study, the position signal x_2 and the input signal v from the DCR are measurable. Under the condition of simple oscillation, without loss of generality, select the instant when the DCR switches to the maximum value as the starting time t_0. Inferring from the nature of integration, when x_2 (position) reaches the maximum value, the time instant then can be denoted as t_1 for relay RA with x_1 (velocity) as input to switch from a positive to negative state. Furthermore, the switching instants t_2 and t_3 of RB and RC are directly observed from v. In this way, the durations between two consecutive switchings $l_1 = t_1 - t_0$, $l_2 = t_2 - t_1$ and $l_3 = t_3 - t_2$ in

the limit cycle are known. By Theorem 3.1, with just one relay experiment, it is possible to estimate the model parameters, i.e., h_1, α and β by numerically solving the set of equations (3.11)$\sim$(3.13). For convenience, (3.11)$\sim$(3.13) can be rewritten as

$$f_1(\theta, \varphi) = C_1\ b(\theta, \varphi) = 0; \tag{3.51}$$

$$f_2(\theta, \varphi) = C_2\ c(\theta, \varphi) = 0; \tag{3.52}$$

$$f_3(\theta, \varphi) = C_3\ a(\theta, \varphi) = 0, \tag{3.53}$$

where a, b, c are the state vectors when the trajectory traverses the switching planes as defined in (3.27)$\sim$(3.29), $\theta = [\alpha, \beta, h_1]^{\mathrm{T}}$ is the identifying parameter vector, and $\varphi = [l_1, l_2, l_3, h_2, h_3]^{\mathrm{T}}$ is the experiment data vector.

However, due to the nonlinear nature of the equation set, it is useful to use additional characteristics of the oscillations to increase the robustness of the parameter estimation. To this end, it may be noted that when the trajectory traverses the switching plane S_1 at time t_1, not only the switching condition $x_1 = C_1 b = 0$ is satisfied, but also the position x_2 is measurable denoted as $x_{2,b} = C_2 b$. Similarly, when the trajectory traverses S_3 at time t_3, an additional condition $x_{2,a} = -C_2 a$ holds. Hence, another two equations are given

$$f_4(\theta, \varphi) = C_2\ b(\theta, \varphi) - x_{2,b} = 0; \tag{3.54}$$

$$f_5(\theta, \varphi) = -C_2\ a(\theta, \varphi) - x_{2,a} = 0. \tag{3.55}$$

Now, numerically solve θ from (3.51)$\sim$(3.55) are achieved using the Gauss-Newton iterative method [50], with an initial guess of parameters $\theta_0 = [\alpha_0, \beta_0, h_{1,0}]^{\mathrm{T}}$.

For the vector function $F = [f_1, f_2, f_3, f_4, f_5]^T$, the Jacobian J_θ of F, w.r.t. θ at $\theta = \theta_i$ at the ith iteration, is defined as

$$J_{\theta,i} = \left[\begin{array}{ccc} \frac{\partial f_1}{\partial \alpha} & \frac{\partial f_1}{\partial \beta} & \frac{\partial f_1}{\partial h_1} \\ \vdots & \vdots & \vdots \\ \frac{\partial f_5}{\partial \alpha} & \frac{\partial f_5}{\partial \beta} & \frac{\partial f_5}{\partial h_1}. \end{array}\right]\Bigg|_{\theta=\theta_i} \tag{3.56}$$

The incremental $\Delta\theta_i$ at ith iteration, is solvable from

$$J_{\theta,i}^T \; J_{\theta,i} \; \Delta\theta_i = -J_{\theta,i} \; F_i. \tag{3.57}$$

where F_i is the value of function vector at the ith iterative based on current guess of parameters' value. The parameter vector is updated as

$$\theta_{i+1} = \theta_i + \Delta\theta_i. \tag{3.58}$$

The iterative search for the parameters terminates when $|\Delta\theta_i| < \varepsilon$, where ε is a small positive value. The function 'lsqnonlin' in MATLAB optimization toolbox provides a ready implementation of Gauss-Newton algorithm [67]. To avoid the situation of the gradient-based optimization indulging in a local minimum, different sets of initial guess values may be used.

This approach is a closed-loop approach based on position feedback information only. Thus, it has advantage of low cost and high noise immunity in practical applications. In addition, the time-domain based method releases the constraint to have sinusoidal-like output waveform in DF based method [23] [92]. Instead, the approach only require the switching information from arbitrary stable limit cycles. Thus, it is able to identify all the model parameters efficiently with a single relay experiment.

3.3.2 Simulation and discussion

Example 3.2. *Consider the second-order positioning system* $\ddot{x} = \alpha\dot{x} + \beta u$*, under the effect of friction simulated via the following models*

1. $f = f_c \text{sgn}(\dot{x})$,

2. $f = (f_s - f_c)\exp(-(\dot{x}/v_s)^2) + f_c \text{sgn}(\dot{x}) + f_v\dot{x}$.

f_s, f_c and f_v denote the static, Coulomb and viscous friction coefficient accordingly, v_s denotes the Stricbeck velocity. The proposed approach in this chapter is amenable to the first friction model comprising of only a Coulomb friction component. The second friction model includes other friction characteristics and it is included in the simulation study to test the robustness of this estimation method. The parameters used in the two friction models are: $f_s = 0.6$, $f_c = 0.5$, $f_v = 0.05$, $v_s = 0.5$, and the linear portion parameters are set as $\alpha = -4$, $\beta = 40$. Through the simulation, the efficiency and accuracy of estimating the model parameters (Coulomb friction f_c (i.e. h_1) as well as linear system parameters α and β) using DCR apparatus will be verified as shown in Figure 3.6.

The Coulomb-friction only model is first simulated, and the gains of DCR are selected as $h_2 = 0.8$, $h_3 = 1$. The steady state oscillation resulting from the relay feedback is shown in Figure 3.7. By Theorem 3.1, the starting time t_0 corresponds to the instant of relay control signal v switching to its maximum amplitude. Although the velocity is not assumed to be measurable, the RA switching instant t_1 can still be tracked from the

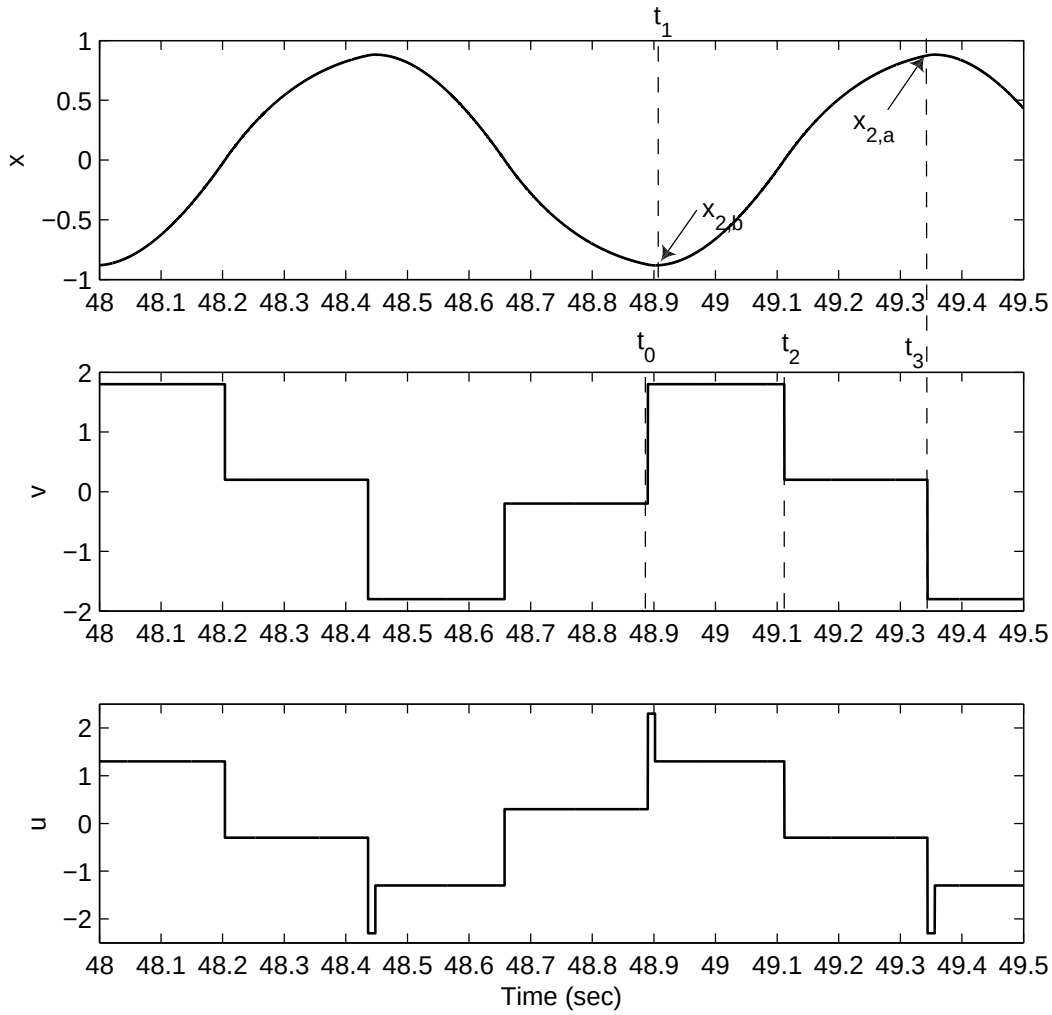

Figure 3.7: Limit cycle with the first friction model. Top: Output signal x. Mid: DCR signal v. Bottom: Actual input signal u fed to linear portion (not measurable in practice).

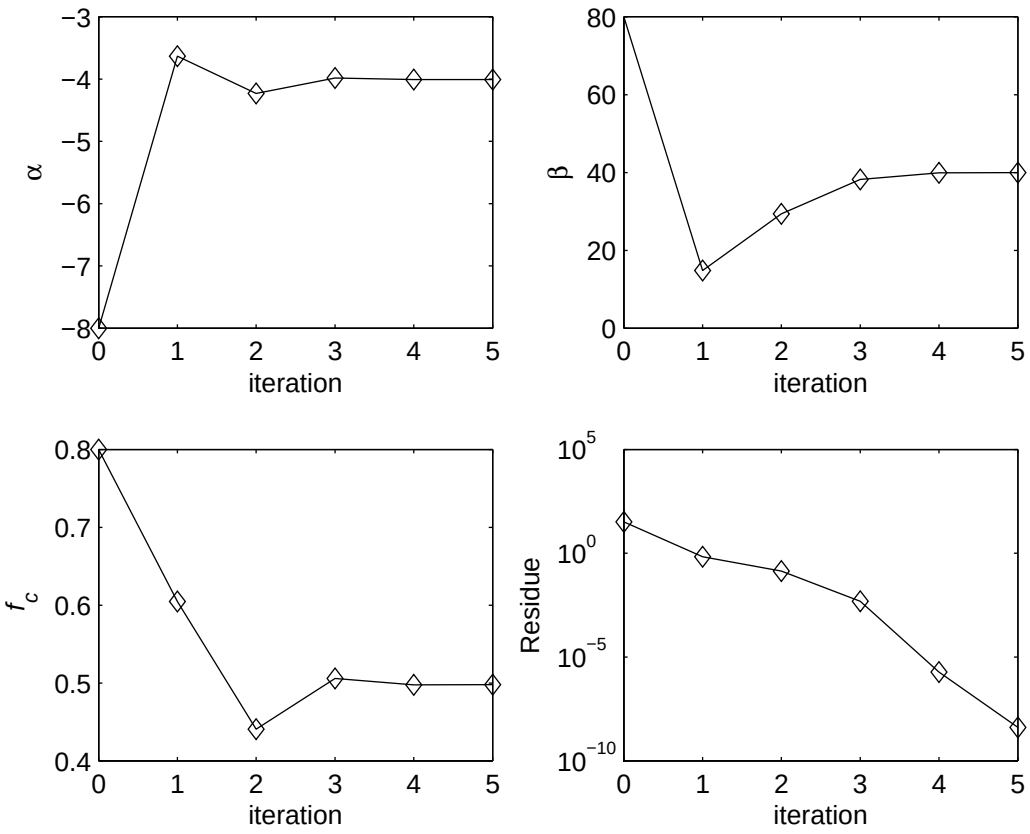

Figure 3.8: Convergence of parameter estimations and residue of cost function with Coulomb friction model.

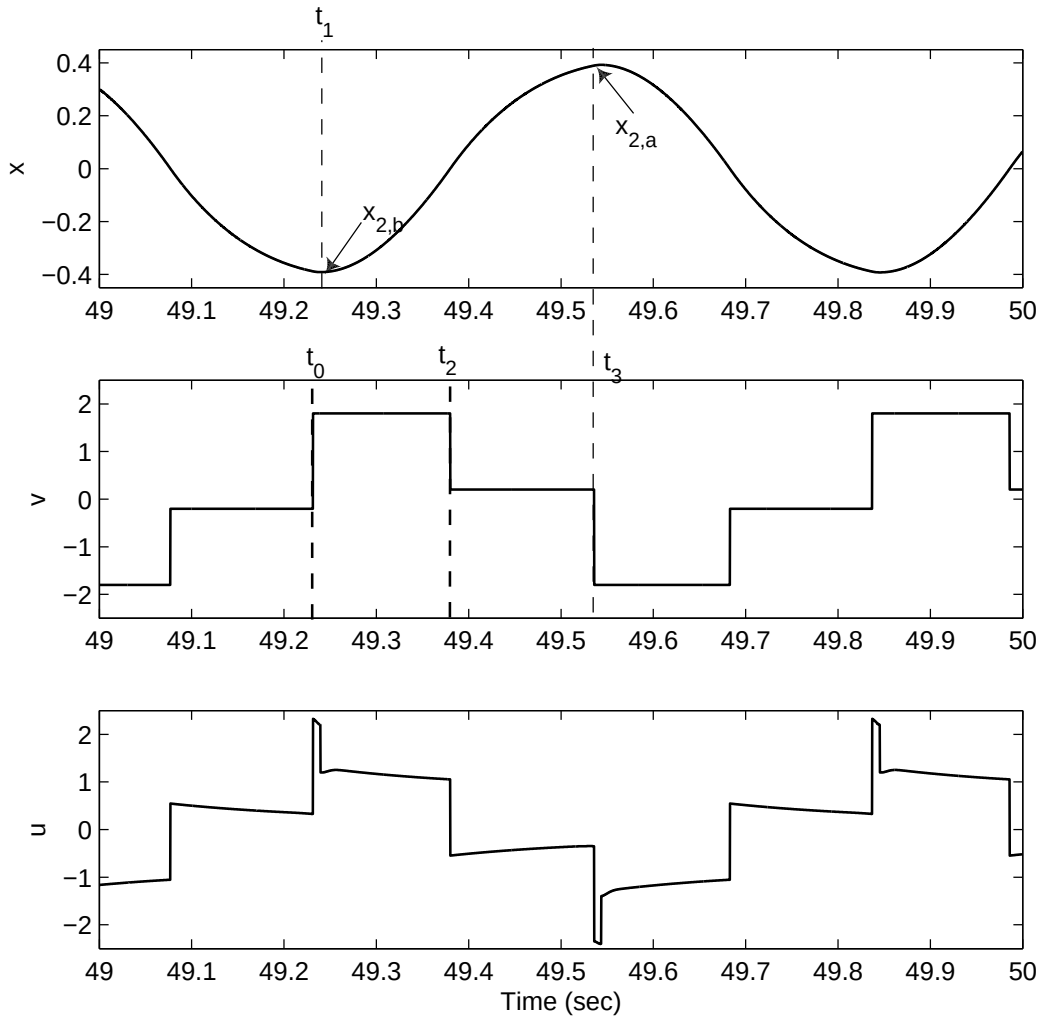

Figure 3.9: Limit cycle with the second friction model. Top: Output signal x. Mid: DCR signal v. Bottom: Actual input signal u fed to linear portion (not measurable in practice).

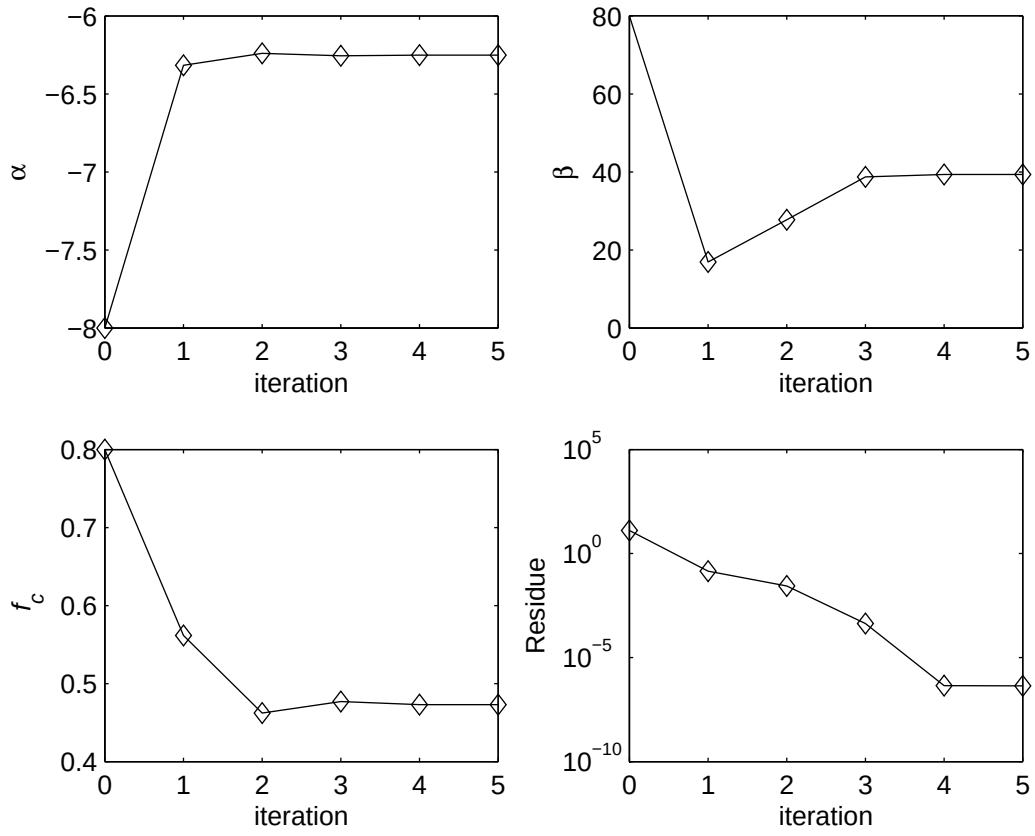

Figure 3.10: Convergence of parameter estimation and residue of cost function with Coulomb friction and Stricbeck effect model.

time the position signal reaches its minimum. The switching instants t_2, t_3 of RB and RC are detectable from the relay control signal v. Thus, the respective time durations required for modeling are obtained as $l_1 = t_1 - t_0 = 0.0119$, $l_2 = t_2 - t_1 = 0.2097$, $l_3 = t_3 - t_2 = 0.2324$, $x_{2,b} = -0.8817$, $x_{2,a} = 0.8752$. By (3.51)$\sim$(3.58), starting from initial guess of $\theta_0 = [-8, 80, 0.8]^T$, the parameters are identified as $\hat{\alpha} = -4.0081$, $\hat{\beta} = 39.9558$ and $\hat{f}_c = 0.4978$ after just five iterations, which are very close to their true values, as shown in Figure 3.8.

Next, the second friction model is used for simulation. Figure 3.9 shows the simulation results of selected waveforms in the system during steady state oscillation, with the same gains of relays as $h_2 = 0.8$ and $h_3 = 1$. l_1, l_2 and l_3 are now observed as 0.0084, 0.1406 and 0.1560. The additional position information $x_{2,b}$, $x_{2,a}$ for modeling are obtained as -0.3925 and 0.3902 respectively. As shown in Figure 3.10, by using the Gauss-Newton iterative method, starting from initial guess of $\theta_0 = [-8, 80, 0.8]^T$, after five iterations, the parameters are identified as $\hat{\alpha} = -6.2520$, $\hat{\beta} = 39.3470$ and $\hat{f}_c = 0.4730$. $\hat{\beta}$ and $\hat{f}_c$ are close to the actual values. The apparent deviation from its true value of $\hat{\alpha}$ is not due to inaccuracy arising from the identification process. The model structure used in this chapter does not include a viscous friction component. Thus, the equivalent effect of viscous friction $f_v\dot{x}$simulated is absorbed into the time constant of the dynamics of the servo system, so that the model is able to account for the viscous friction dynamics via a modified linear portion. It can be verified that this is indeed true by checking if

$$\hat{\alpha} \approx \alpha - \beta f_v$$

. Indeed, $\hat{\alpha}$ is close to -6 consistent with the simulation results.

3.4 Real-Time Experiment on a DC Motor

To illustrate the effectiveness of proposed method, real-time experiments are carried out on a LJ Electronic MS15 DC Motor platform, as shown in Figure 3.11. The DC Motor accepts the analog input voltage to generate different rotation speeds. In the proposed method, only the position signal is required, which is provided by the on-shaft potentiometer. With PC-based National Instrument (NI) Data Acquisition (DAQ) Card and LabVIEW virtual instrument platform, the front panel or user interface is integrated with the background program into a single development platform. MATLAB optimization toolbox is also used for data analysis [67]. Figure 3.12 further illustrates the block diagram of the experiment setup. For conducting the experiment, a virtual instrument (VI) program is built using LabVIEW based on the DCR feedback configuration of Figure 3.6. Note that the potentiometer in this DC motor is attached to the slave shaft, rather than the master one, and the ratio of angular velocity between them are $1:9$. The gains of the DCR are selected according to the properties of DCR gains in [23], such that the angular displacement of the slave shaft does not exceed $\pm 2\pi$, for correctly detecting the position signal.

3.4.1 Parameter estimation

By selecting $h_2 = 0.5$ and $h_3 = 0.8$; the experiment results of limit cycles of DC motor position signal under DCR feedback is shown in Figure 3.13, with a sampling period

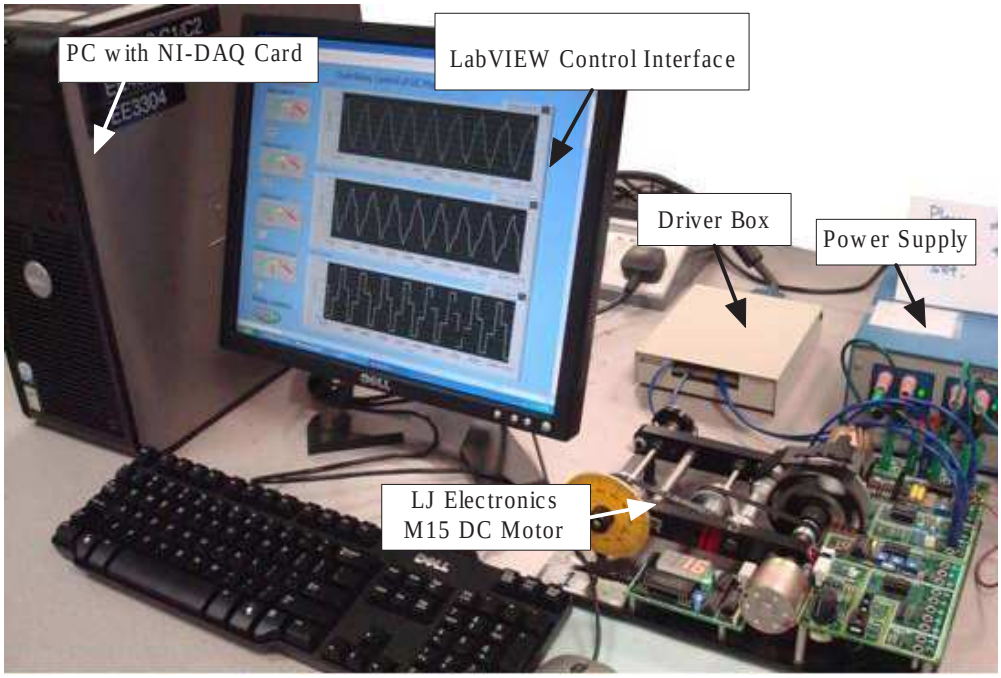

Figure 3.11: Setup of DC motor experiment.

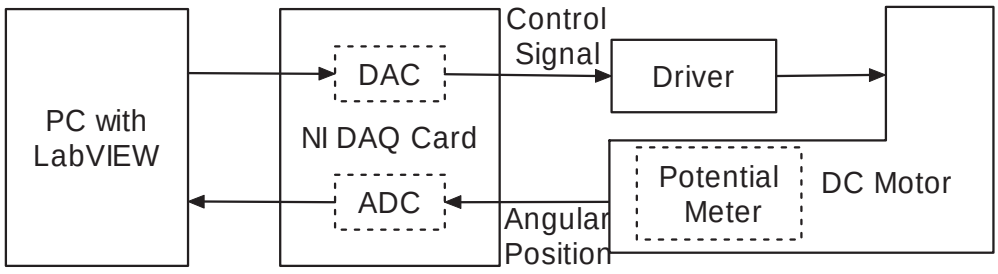

Figure 3.12: Block diagram for illustration of experiment setup.

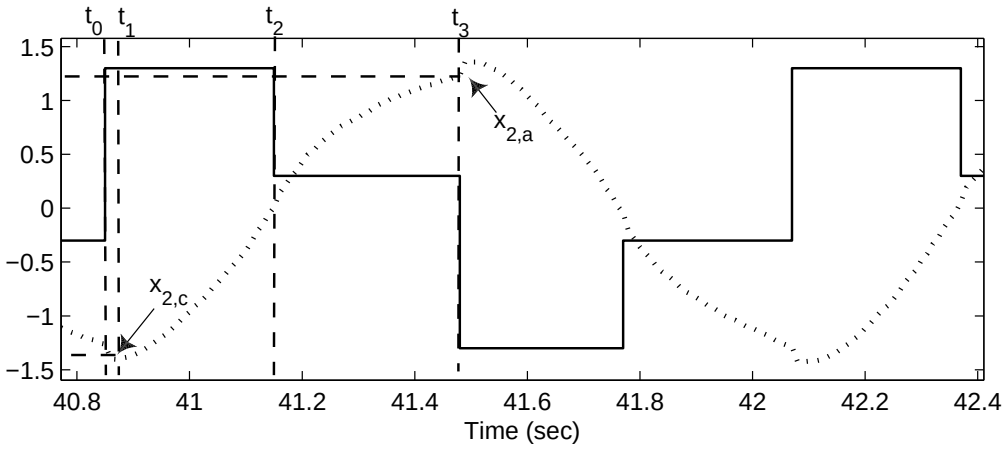

Figure 3.13: Limit cycle in the DC motor experiment by the DCR feedback $h_2 = 0.5$, $h_3 = 0.8$. Solid line: Waveform of relay signal. Dotted line: waveform of DC motor position.

of $10ms$. The various data required for modeling are extracted from the oscillation as $l_1 = 0.025$, $l_2 = 0.270$, $l_3 = 0.330$, $x_{2,a} = 1.250$ and $x_{2,c} = -1.402$. Starting from $\theta_0 = [-3, 30, 0.3]^T$, by Gauss-Newton method, the system parameters are identified as $\alpha = -6.3935$, $\beta = 52.4523$, $h_1 = 0.1456$ after just four iterations, as illustrated in Figure 3.14.

3.4.2 Model verification via feedback compensation

With the model identified, a full-state feedback linearization controller is designed to verify the adequacy of model parameters thus obtained. Due to the placement of velocity and position sensor, a gain of 9 exists between velocity and position signals obtained, as shown in Figure 3.12. Thus, in the velocity loop model, $\ddot{x} = \alpha\dot{x} + \bar{\beta}u$, where $\bar{\beta} = \beta/9$, and $u = v - f$, f is the friction force.

With the identified model α , β , f_c , in order to achieved the tracking of the trajectory

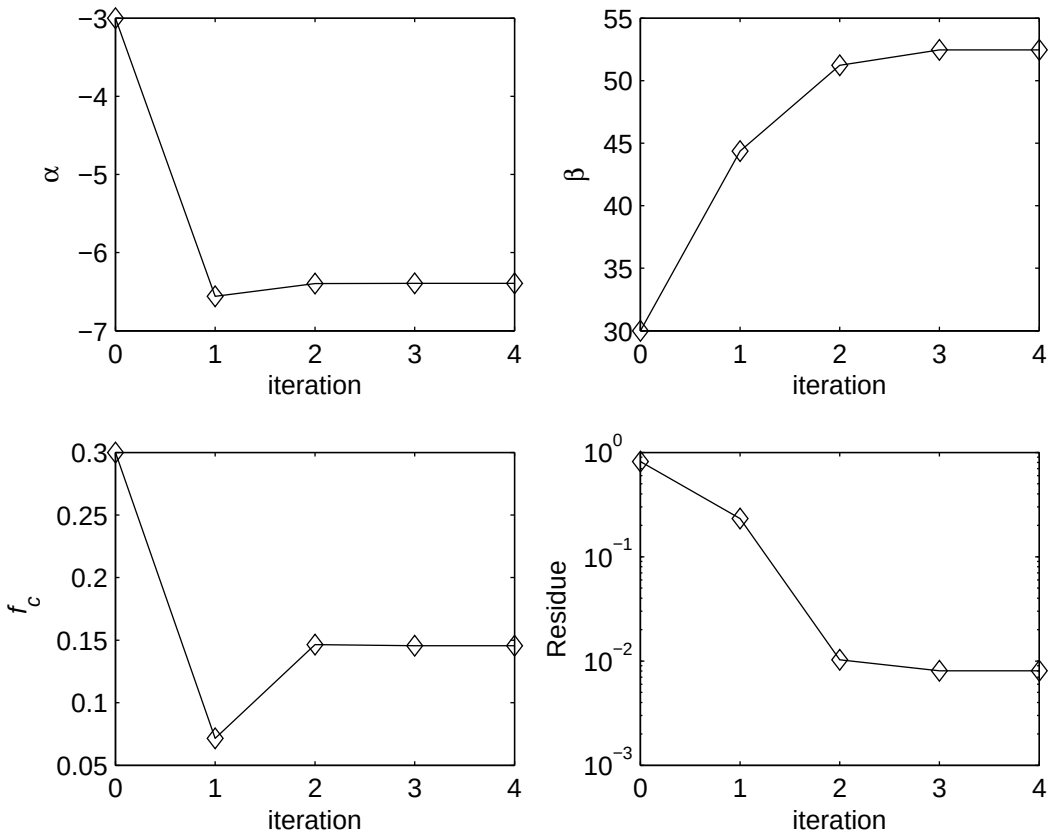

Figure 3.14: Convergence of parameter estimation and residue of cost function in DC motor experiment.

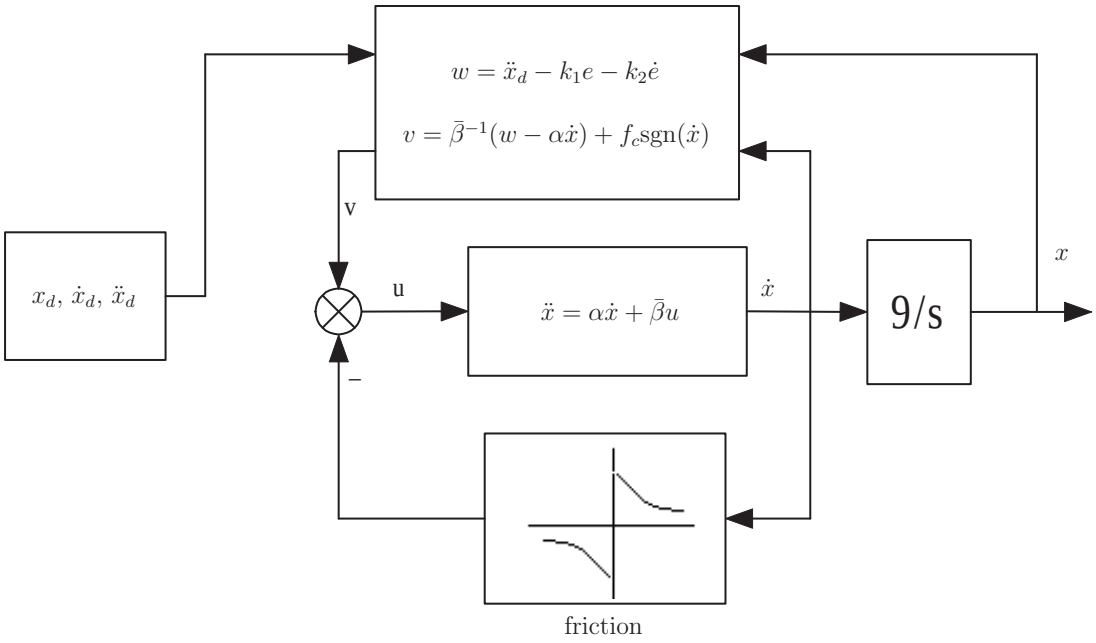

Figure 3.15: Design of feedback controller with compensation.

profile x_d, set $w = \alpha\dot{x} + \bar{\beta}\left[v - f_c \mathrm{sgn}(\dot{x})\right]$, or

$$v = \bar{\beta}^{-1}(w - \alpha\dot{x}) + f_c \mathrm{sgn}(\dot{x}), \tag{3.59}$$

so that $\ddot{x} \approx w$. Define the tracking error as $e(t) = x(t) - x_d(t)$, so that $\dot{e} = \dot{x} - \dot{x}_d$ and $\ddot{e} = \ddot{x} - \ddot{x}_d$. If w is is defined as

$$w = \ddot{x}_d - k_1 e - k_2 \dot{e}, \tag{3.60}$$

Then the following closed-loop error dynamics is achieved

$$\ddot{e} + k_2 \dot{e} + k_1 e = 0. \tag{3.61}$$

For comparison purpose, define the controller without the friction compensator as

$$v = \bar{\beta}^{-1}(w - \alpha\dot{x}), \tag{3.62}$$

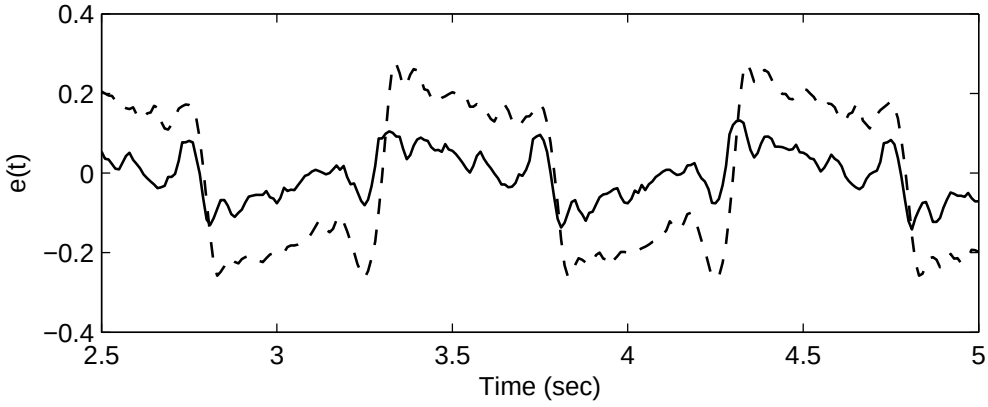

Figure 3.16: Tracking error with model-based feedback controller. Solid line: with friction compensation. Dashed line: without friction compensation.

while w is defined as in (3.60).

In the experiment, the desired time-varying trajectory is defined as $x_d(t) = 4.5\sin(0.2\pi t)$. By applying the control scheme in (3.59) and (3.60), with the parameters obtained from identification $\hat{\alpha} = -6.39$, $\hat{\bar{\beta}} = \hat{\beta}/9 = 5.823$, $\hat{f}_c = 0.1456$ and select $k_1 = 5.5$ and $k_2 = 14.5$. The control scheme without friction compensation as in (3.60) and (3.62), with the same parameters values, is also investigated for comparison purposes. The tracking error and the control signals are shown in Figure 3.15 and 3.16 accordingly. From these two figure, it is able to observe that, by applying similar control efforts, with the model-based friction compensation scheme, the root-mean-square (RMS) of the tracking error is drastically reduced from 0.1881 to 0.0613, using the model parameters obtained in the previous phase. The remaining error can be attributed mainly to unmodeled dynamics of the DC motor.

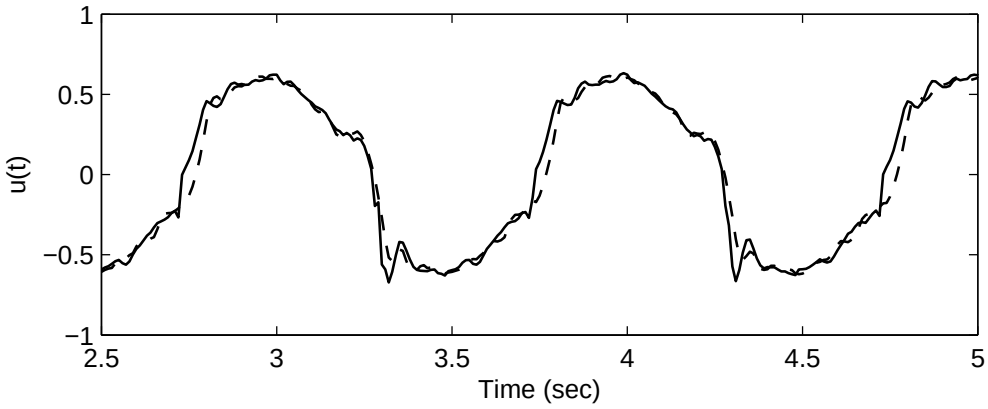

Figure 3.17: Controller output with model-based feedback controller. Solid line: with friction compensation. Dashed line: without friction compensation.

3.5 Conclusion

A systematic analysis of the properties of limit cycles arising in a class of commonly encountered systems under full-state triple-relay feedback is done in this chapter. The locations of limit cycles can be determined by the numerical method proposed, which gives the exact duration between two consecutive relay switchings. The local stability of limit cycles can be further assessed using the Jacobian of Poincaré Map. The results are applied to modeling of servo-mechanical systems experiencing Coulomb friction as the configuration considered can be mapped to an equivalent case of such systems under DCR feedback. Simulation and real-time experiment have verified the applicability of the new method.

Chapter 4

Identification of Four-Parameter Friction Model with Dual-Channel Relay Feedback

4.1 Introduction

The designs and applications of motion control systems have been closely related to investigation of friction between contact surfaces of machine's subparts. Thus, this chapter starts from brief review of the the history of science of friction, or tribology.

4.1.1 Review of friction and friction models

Friction is the force resisting the relative lateral (tangential) motion of solid service. Humans has tried to make use of friction between two rough stones to lay fires since stone ages. In ancient Egypt, workers learned to put heavy stones on wooden sledges so that easier transportation of these stones is achieved due to much reduced friction during rolling. The usage of friction was even applied to design a complicated loom machine for figure weaving in silk handicraft industry in the Ming Dynasty of China (1368-1644 A.D.) [84]. The classical understanding of friction was continually investigated

in [29] [6] [28] et al., their findings are summarized in the following laws:

1. The force of friction is directly proportional to the applied load.

2. The force of friction is independent of the apparent area of contact.

3. Kinetic friction is independent of sliding velocity.

The laws above describe the behaviors of so-called Coulomb friction. The relay-type Column friction model in Figure 4.1(a) is a simple, but efficient one to describe friction behavior when the motion is non-stuck and in medium speed. In order to describe friction behavior under different moving condition, various other friction models are developed. For the motion with high speed, the viscous friction needs to be considered, thus the Coulomb+viscous friction model is set up, as shown in Figure 4.1(b). For motion involving sticking behavior, the ideal of static friction is introduced, forming the most common used friction model in Engineering: the static+Coulomb+viscous friction model [69] [77], as shown in Figure 4.1(c). For example, this friction model is used for setting up physical model of valve positioning system, where strong skip-slip behavior is observed, as shown in Chapter 2, as well as in [27].

The increasing demands on the precision engineering boost the modeling of friction in an more accurate way. As the machine accelerates from zero velocity, the friction will first drop from maximum static friction to Coulomb friction, and then increase due to the viscousity, forming the negative-viscous+Coulomb+viscous friction model [17], as shown in Figure 4.1(d). This model may be approximated as a four-parameter segmental

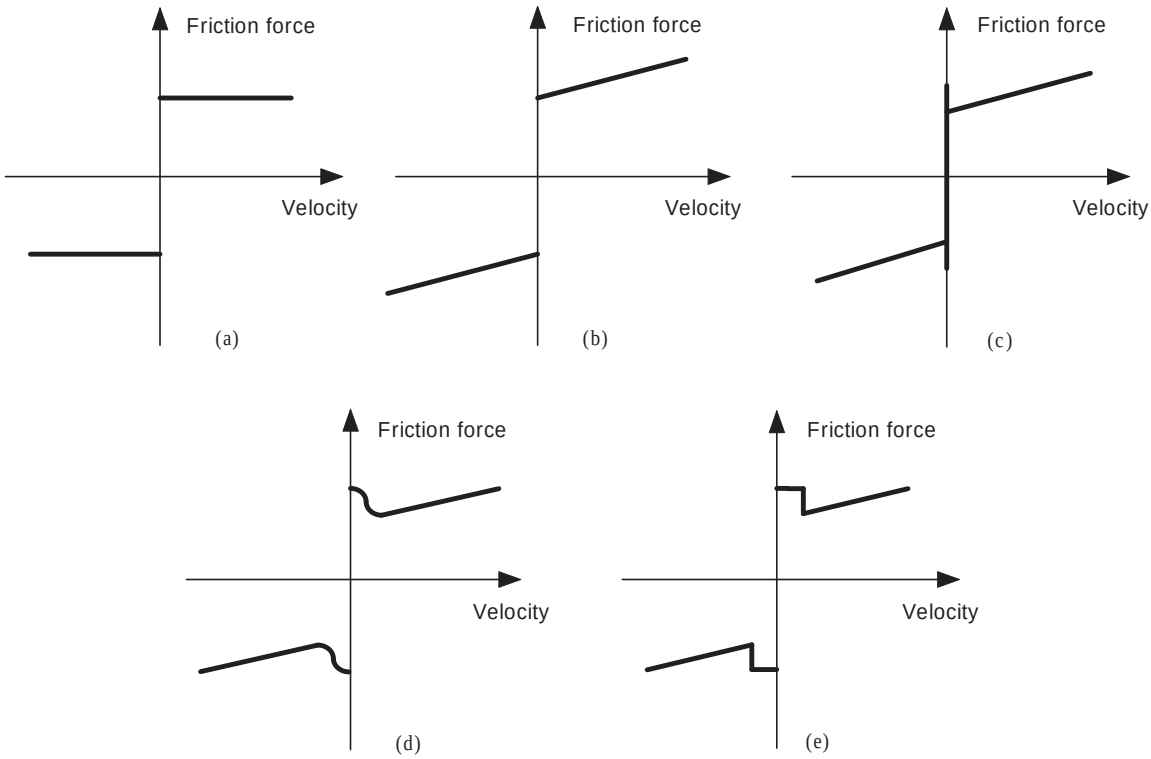

Figure 4.1: Various friction models. (a) Coulomb. (b) Coulomb + viscous. (c) static + Coulomb + viscous. (d) negative viscous + Coulomb + viscous: Form A. (e) negative viscous + Coulomb + viscous: Form B.

hard-nonlinearity type model [55], as shown in Figure 4.1(e), which is easier for further analysis by decomposition.

The above models approximate the friction force as a function of steady state velocity. For more accurate investigation of friction behavior, various the dynamic friction models, such as LuGre Model and Maxwell Slip Model are proposed [31] [87] [58] [5] [32] and discussed [44] [45] [78] [48], which consists the internal variables for describing the memorial properties of friction force. However, till now, it is still difficult to use these models for compensation since the state variables of the models are generally not measurable while the identification of the model parameters remains a challenge.

In the theoretical investigation of property of friction, the describing function analysis approximate the friction as a quasi-linear element, from which the limit cycle amplitude and frequency can be estimated [12]. For a more accurate analysis in time domain, the concepts of set-valved theorems and differential equations with discontinuous right hand side are imported, so that solutions of ordinary differential equations can be extended to this kind of discontinued nonlinearity [34].

4.1.2 Review of existing friction modeling techniques

As mentioned in Chapter 3, applications of relay feedback techniques to automatic tuning of controllers have been widely explored since the 1980s [10]. Today, many industrial controllers are equipped with such automatic tuning features in different forms [94]. The basis of such an approach is simple and efficient; a sustained oscillation of a controlled variable is first excited through relay feedback, from which the characteristics of the system can be inferred and subsequently used to tune the controller. Besides identifying and tuning the linear plants [100], new applications have arisen where relay feedback is used to identify nonlinear models since 1990s. In [16], [92], [95] and Chapter 3 of this thesis, approaches using relay feedback for the identification of simplified friction models for servo-mechanical systems are presented. However, the simplified models considered in these works comprise only at most of either or both the Coulomb and viscous friction components only. When the servo-mechanical system operates bi-directionally, or it operates over a wide range of velocity including low velocities, these simplified friction models can become rather inadequate when the other friction components, such as static

friction and the Stribeck effect, are not considered and yet they become dominant at low velocities [24]. Friction compensation via inadequate models can still incur large tracking errors. In recent years, different techniques, either black-box or white-box based, are proposed for precise friction modeling. In [97], black-box friction modeling via Radial-Based Function (RBF) neural networks is applied to piezoelectric motor control. In [96], the RBF network is designed in parallel with a iterative learning control (ILC), modeling the nonlinear part while iteratively adjusting the reference signal, hence the error convergence rate is greatly improved. White-box modeling approaches, such as those using the frequency response for dynamic friction modeling [45] and relay-based method for two-segment, four-parameter friction modeling with a velocity feedback loop [55], are also proposed in recent years. In [25], binary multi-frequency signal is imported for open-loop identification of friction in frequency domain. In [45], the frequency response function technique is applied to identify the dynamic friction model by augmenting it with the plant, linearizing and simplifying it to a lower dimension model. However, some parameters are still coupled after identification, which may result in difficulties for model-based compensation. The applicability is also limited by the requirement of large volume of experiment data and prerequisite of open-loop stability. Theoretical research on multiple relay feedback systems has extended application of RFSs from single relay structures to multiple ones [62] [63]. For identifying friction models with more than one parameter, Dual-Channel Relay (DCR) feedback systems have been proposed [35] [92] [95] so that additional degree-of-freedom is enjoyed.

4.1.3 Motivations and novelty of new approach

The four-parameter friction model as in Figure 4.1(e) is proposed and identified in [55] with DCR feedback apparatus. However, explicit formulas to extract these parameters efficiently from the data collected from finite sets of relay experiments are not available, yet such efficient ways of computing model parameters from the data obtained with relay feedback experiments are trademarks of this highly popular approach in process control. Instead, a nonlinear-least-square (NLS) method is used in their method to estimate the four parameters. However, the estimated parameters can be significantly different from the actual parameters, the extent of which greatly depends on the initial conditions. Moreover, the approach requires extensive data to yield results, and in addition, the approach is based on a velocity feedback loop and thus, it inherits the usual problem of noise sensitivity when the velocity measurements have to be observed from the position signal. To overcome this problem, the low-pass filter is used, which increases the complexity of their identification method.

In the new approach, the same four-parameter model of [55] is used. However, the velocity feedback used in [55] is replaced by the position feedback, thus eliminating the need to have an additional filter. Furthermore, the new approach is formulated to circumvent the problem and remove the necessity to search for the multiple parameters simultaneously in the optimization process. Instead, a systematic approach is adopted to run the relay experiments with the servo-mechanical system operating first under a low velocity mode, and subsequently, a high velocity mode. In this way, a set of explicit

formulas derived based only on describing function analysis are obtained to extract the parameters very efficiently from data. Only the boundary lubrication velocity is obtained through a single parameter optimization based on the same set of data available from the same experiments. As the bounds are known and there is only a single parameter variation in the optimization process, the difficulties with [55] do not exist in the method. The properties of the DCR apparatus will be analyzed and presented in the method, and based on these properties, proper selection of the relay amplitudes is done to yield adequate oscillations necessary in each phase of the procedures. Based on the system model obtained, a control scheme of incorporating a PID feedback controller with a feed-forward friction compensator is developed and demonstrated to give better tracking performance. All the results are supported by simulation and real-time experiment.

4.2 System Model

The dynamics of a servo-mechanical system is described using a nonlinear mathematical model:

$$u(t) = K_e\dot{x} + Ri(t) + Ldi(t)/dt, \tag{4.1}$$

$$f(t) = K_f i(t), \tag{4.2}$$

$$f(t) = m\ddot{x}(t) + \bar{f}_{\text{load}}(t) + \bar{f}_{\text{nl}}(t), \tag{4.3}$$

where $u(t)$ and $i(t)$ are the time-varying motor terminal voltage and armature current, respectively; $x(t)$ is the motor position; $f(t)$ and $\bar{f}_{\text{load}}$ are the developed force and the applied load force respectively, $\bar{f}_{\text{nl}}$ is nonlinearity affecting the developed force. In the

Table 4.1: Parameters of the linear motor.

Parameters	Physical meaning	Units
K_f	Force constant	N/Amp
R	Resistance	Ohms
K_e	Back EMF	vol/m/sec
L	Armature inductance	mh
m	Mass of moving part	Kg

servo-mechanical system concerned in this chapter, friction force $\bar{f}_{\text{fric}}$ and the remaining small and unaccounted dynamics $\bar{f}_{\text{res}}$ are presented. Thus,

$$\bar{f}_{\text{nl}} = \bar{f}_{\text{fric}} + \bar{f}_{\text{res}}. \tag{4.4}$$

Other parameters are described in Table 4.1.

Since the electrical time constant is much smaller than the mechanical one, the transient delay due to the electrical response is ignored. The following equivalent model is obtained after simplification

$$\ddot{x} = (a\dot{x} + u - f_{\text{fric}} - f_{\text{load}} - f_{\text{res}})/b, \tag{4.5}$$

where $a = -K_e$, $b = mR/K_f$, $f_{\text{fric}} = R\bar{f}_{\text{fric}}/K_f$, $f_{\text{load}} = R\bar{f}_{\text{load}}/K_f$, and $f_{\text{res}} = R\bar{f}_{\text{res}}/K_f$.

Let $\tilde{u} = u - f_{\text{fric}} - f_{\text{load}} - f_{\text{res}}$, $\tau = -b/a$, and $K = -1/a$. The transfer function of the linear portion of the servo-mechanical system is shown to be

$$G_p(s) = X(s)/\tilde{U}(s) = K/\left[s(\tau s + 1)\right]. \tag{4.6}$$

The friction force is usually modeled as an odd nonlinearity with different types of friction components. The complexity and required accuracy of the model mainly depends

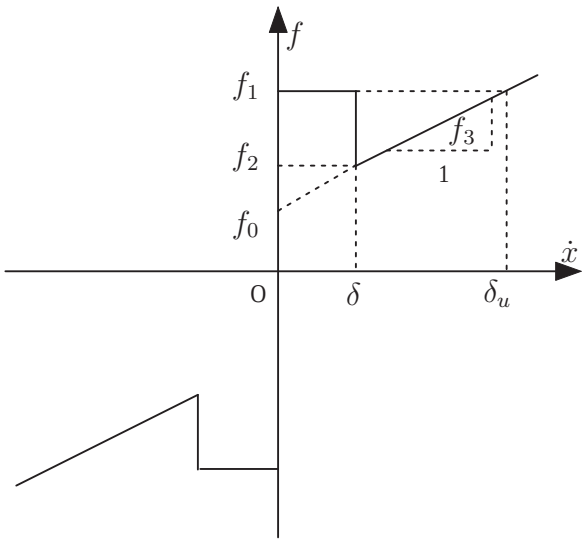

Figure 4.2: Four-parameters friction model.

on the application domain. When the system operates essentially in the high-velocity mode, a two-parameters friction model, which takes into account the Coulomb friction f_c and viscous friction f_v [7], [92] is adequate enough. However, when the system operates in the low-velocity or a bi-directional mode, a more accurate and elaborate model, which considers the static friction f_s, the Coulomb friction f_c, viscous friction f_v as well as the Stribeck effect, will become necessary [7], [55].

The generalized friction force f, discussed in the method, is a summation of friction force f_{fric} and loading force f_{load}. If the loading force is dependent of the direction of motion, f_{load} is described as $f_{\text{load}} = f_l \text{sgn}(\dot{x})$. The generalized four-parameter friction model as shown in Figure 4.2 is expressed as

$$f = \begin{cases} f_1 \text{sgn}(\dot{x}) & \text{if } |\dot{x}| < \delta, \\ [f_2 + f_3(|\dot{x}| - \delta)] \, \text{sgn}(\dot{x}) & \text{if } |\dot{x}| \geq \delta, \end{cases} \tag{4.7}$$

where f_1 is the generalized maximum static friction, f_2 is generalized Coulomb friction,

f_3 is associated with the viscosity constant and δ is the lubrication boundary velocity (LBV), where $f_1 = f_s + f_l$, $f_2 = f_c + f_l$, $f_3 = f_v$.

4.3 DCR Feedback System

The DCR feedback structure, as shown in Figure 4.3(a), has been used for the identification of friction model as well as the parameters of the linear dynamical part of a servo-mechanical system [35], [92]. The configuration of DCR has been discussed in Chapter 3.

For the convenience of further discussion, an equivalent circuit is shown in Figure 4.3(b) which segregates the full feedback system into a linear portion and a nonlinear portion. The linear portion contains the system dynamics and DC gain, while the nonlinear portion includes the actual frictional and load forces SR, as well as the two intentional relays FR1 and FR2 in use. The Describing Function (DF) of the equivalent relay (N_{ER}) is simply the sum of the individual DFs due to the feedback relays (N_{FR1}), (N_{FR2}) and the inherent system relay (N_{SR}), i.e.,

$$N_{ER} = N_{FR1} + N_{FR2} + N_{SR}, \tag{4.8}$$

where $N_{FR1}(A) = 4h_1/(\pi A)$, $N_{FR2}(A) = -4jh_2/(\pi A)$. Similar to [55], the nonlinear friction element in the four-parameter friction model of Figure 4.2 is approximated with quasi-linear elements by using the following DFs [36], [83], as shown in Figure 4.4

$$N_{SR}(A, \omega) = N_A(A) + N_B(A, \omega) - N_C(A, \omega), \tag{4.9}$$

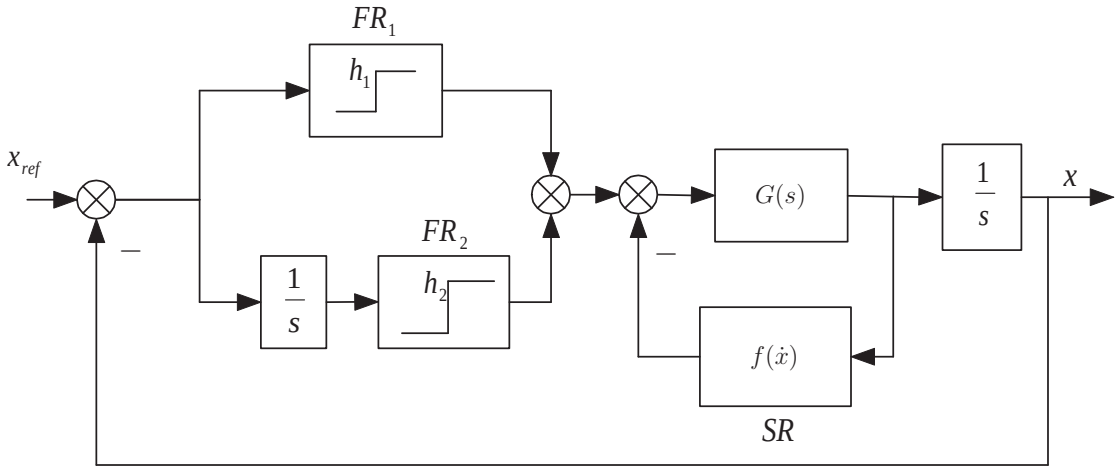

(a)

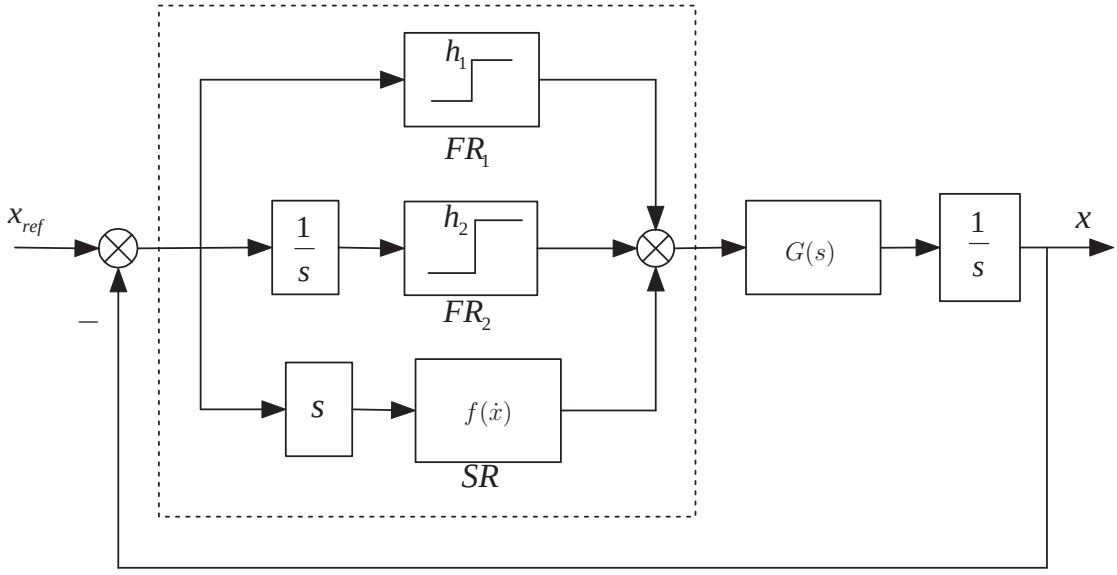

(b)

Figure 4.3: The DCR apparatus. (a) Original Setup. (b) Equivalent system.

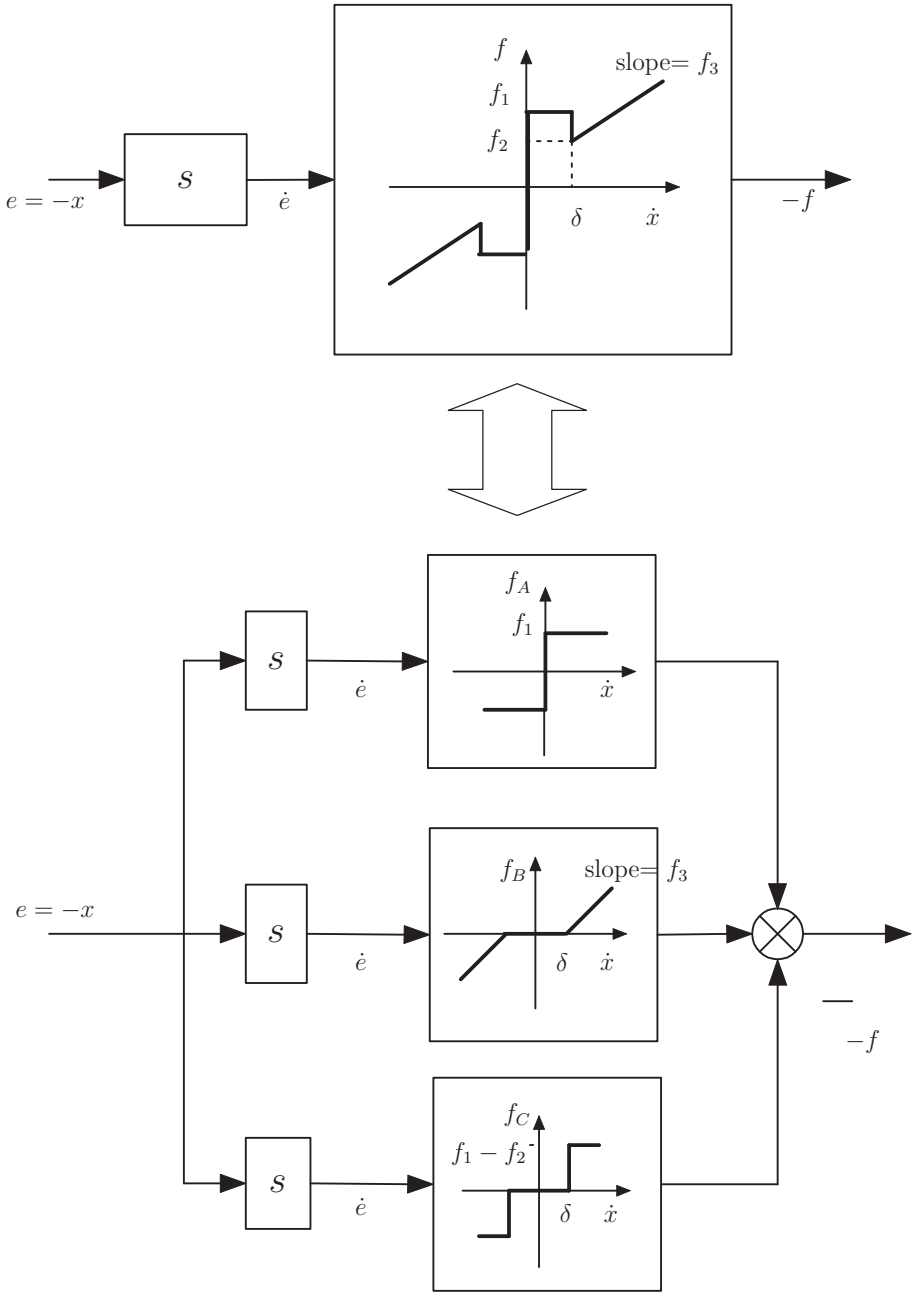

Figure 4.4: Friction model decomposition.

where

$$N_A(A) = 4jf_1/(\pi A), \tag{4.10}$$

$$N_B(A,\omega) = \begin{cases} 0 & ,\omega A < \delta \\ \dfrac{2jf_3\omega}{\pi}\left[\cos^{-1}\left(\dfrac{\delta}{\omega A}\right) - \dfrac{\delta}{\omega A}\sqrt{1-\left(\dfrac{\delta}{\omega A}\right)^2}\right] & ,\omega A \geq \delta \end{cases} \tag{4.11}$$

$$N_C(A,\omega) = \begin{cases} 0 & ,\omega A < \delta \\ \dfrac{4j(f_1-f_2)}{\pi A}\sqrt{1-\left(\dfrac{\delta}{\omega A}\right)^2} & ,\omega A \geq \delta \end{cases} \tag{4.12}$$

Remark 4.1. *The DFs (N_B and N_C) are frequency dependent, compared to those in [55], since the inherent relay due to friction is pre-cascaded with a differentiator. This arises because position feedback is used in the method, instead of the velocity feedback used in [55].* $\diamondsuit$

Remark 4.2. *The DFs (N_B and N_C) are piecewise continuous, and ωA is an approximation of the velocity amplitude. This is reasonable the DF analysis assumes a sinusoidal input $x(t) = A\sin(\omega t)$ which, after differentiation and before input to the relay element, becomes $\dot{x}(t) = \omega A\cos(\omega t)$.* $\diamondsuit$

4.4 Limit Cycles in the DCR Feedback System

To propose new identification method, in this section, some properties of limit cycles induced in this DCR feedback system are investigated.

Property 4.1. *For the DCR system in Figure 4.3(a), if a limit cycle exists, its amplitude $A(h_1, h_2)$ will decrease (or increase) with an increase in h_1 (or h_2); the oscillation*

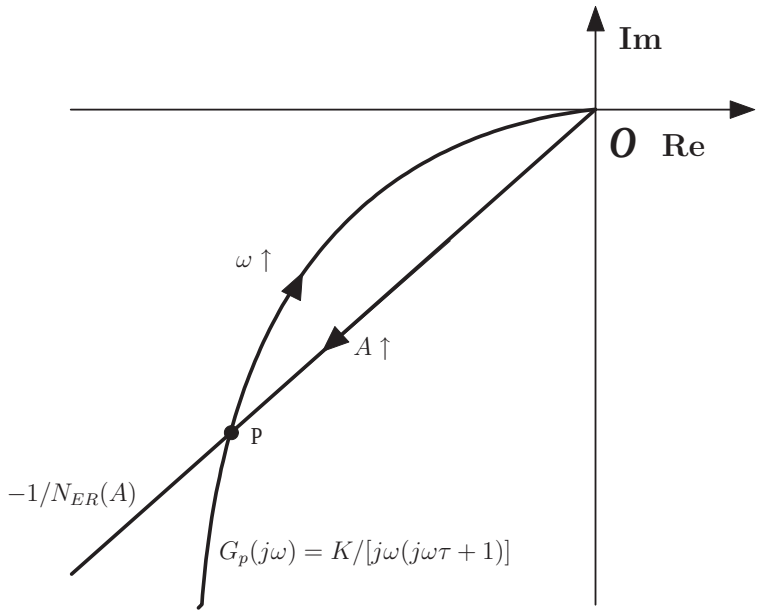

Figure 4.5: Location of limit cycles under DCR feedback.

frequency $\omega(h_1, h_2)$ *will increase (or decrease) with an increase in* h_1 *(or* h_2*).* $\diamondsuit$

Proof of Property 4.1: Two separate cases, corresponding to $\omega A < \delta$ and $\omega A \geq \delta$, will be discussed.

1) When $\omega A < \delta$, from the friction model in (4.7), the nonlinear model is approximated as a simple relay nonlinearity. The DF of the equivalent relay is now simplified to

$$N_{ER}(A) = 4h_1/(\pi A) - 4jh_2/(\pi A) + 4jf_1/(\pi A). \tag{4.13}$$

The frequency response of the linear portion of the system is

$$G_p(j\omega) = K/\left[j\omega(j\omega\tau + 1)\right]. \tag{4.14}$$

As shown in Figure 4.5, by describing function analysis, the sustained oscillation occurs when

$$G_p(j\omega) = -1/N_{ER}(A), \tag{4.15}$$

with the point P as the location of limit cycle. Substitute (4.13) and (4.14) into (4.15), it follows that

$$4h_1/(\pi A) + 4j(f_1 - h_2)/(\pi A) = \omega^2\tau/K - j\omega/K. \tag{4.16}$$

Comparing the real part and imaginary part yields

$$\omega = h_1/[\tau(h_2 - f_1)]. \tag{4.17}$$

$$A = 4K\tau(h_2 - f_1)^2/(\pi h_1). \tag{4.18}$$

From (4.17) and (4.18), it is observed that when h_1 increases, ω will increase and A will decrease; when h_2 increases, ω will decrease and A will increase.

2) When $\omega A > \delta$, the DF of nonlinear portion $N_{ER}(A, \omega)$ is expressed as

$$N_{ER}(A, \omega) = 4h_1/(\pi A) - 4jh_2/(\pi A) + N_{SR}(A, \omega), \tag{4.19}$$

where $N_{SR}(A) = N_A(A) + N_B(A) - N_C(A)$, and

$$\begin{aligned}
N_A(A) &= 4jf_1/(\pi A), \\
N_B(A) &= 2jf_3\omega/\pi\Big[\cos^{-1}(\delta/\omega A) - \delta\sqrt{1 - (\delta/(\omega A))^2}/(\omega A)\Big], \\
N_C(A) &= 4j(f_1 - f_2)\sqrt{1 - (\delta/(\omega A))^2}/(\pi A).
\end{aligned}$$

It is difficult to solve $G_p(j\omega) = -1/N_{ER}(A)$ here, since the function is transcendental and a closed-form solution is not available. Thus, the DF approximation technique is applied to develop an approximate expansion of the exact DF, so that the problem becomes analytical. Using the approximation formulas proposed in [36], when the odd-nonlinearity $y(u)$ is pre-cascaded with an differentiator, it follows that the DF is

approximated by

$$N(A,\omega) \approx j\frac{2}{3A}\left[y\left(A\omega\right) + y\left(\frac{A\omega}{2}\right)\right]. \tag{4.20}$$

By (4.20)

$$N_A(A) \approx 4jf_1/(3A), \tag{4.21}$$

$$N_B(A,\omega) \approx jf_3\left(\omega - 4\delta/(3A)\right), \tag{4.22}$$

$$N_C(A,\omega) \approx 4j(f_1 - f_2)/(3A). \tag{4.23}$$

$$N_{ER1}(A) \approx 4h_1/(3A), \tag{4.24}$$

$$N_{ER2}(A) \approx -4jh_2/(3A), \tag{4.25}$$

and

$$N_{ER}(A,\omega) = N_{ER1}(A) + N_{ER2}(A) + (N_A(A) + N_B(A,\omega) - N_C(A,\omega)). \tag{4.26}$$

Substitute (4.21)$\sim$(4.25) into (4.26), and applying (4.16), yields

$$\omega = h_1(f_3K + 1)/\left[\tau(h_2 - f_0)\right]. \tag{4.27}$$

$$A = pK\tau(h_2 - f_0)^2/\left[h_1(f_3K + 1)^2\right]. \tag{4.28}$$

where $f_0 = f_2 - f_3\delta$, $p = 4/\pi \approx 4/3$. Note that it needs $h_2 - f_0 > 0$ to hold to excite a limit cycle oscillation (see Property 4.3). From (4.27), ω will increase if h_1 increases, or h_2 decreases. From (4.28), when h_1 increases, A will decrease; when h_2 increases, A will increase. $\square$

Property 4.1 discusses the limit cycle properties within the regions $A_v < \delta$ and $A_v \geq \delta$. However, it does not reflect the changes in limit cycle properties when A_v crosses δ. This

phenomenon will be illustrated in Property 4.4.

Property 4.2. *Under the constraints of a describing function analysis, the velocity amplitude will increase with h_2, but it is invariant with h_1.* $\diamondsuit$

Proof of Property 4.2: Using a describing function analysis, $A_v \approx \omega A$. Two cases, $\omega A < \delta$ and $\omega A \geq \delta$ will be discussed accordingly.

1) When $\omega A < \delta$, from (4.17) and (4.18), the velocity amplitude is expressed as

$$\omega A = K(h_2 - f_1). \tag{4.29}$$

From (4.29), A_v will increase (or decrease) if h_2 increases (or decreases), but A_v is not affected much by varying h_1.

2) When $\omega A \geq \delta$, from (4.17)$\sim$(4.18),

$$\omega A = h_1 K^2 \tau p/\omega. \tag{4.30}$$

From (4.30) and (4.27), it follows that

$$\omega A = p h_1 K/\omega = p(h_2 - f_0)K/[\tau(f_3 K + 1)]. \tag{4.31}$$

From (4.31), it is noted that ωA is not affected much by h_1, but it increases with h_2. $\square$

Property 4.1 and 4.2 are summarized in Table 4.2 for quick reference.

Property 4.3. *For the system with DCR structure as in Figure 4.3(a), under a describing function analysis, a necessary condition of existence of the limit cycle is $h_2 > f_1$.* $\diamondsuit$

Table 4.2: Change of limit cycle via tuning of relay gains.

Relay gains	A	ω	A_v
$h_1 \nearrow$	$\searrow$	$\nearrow$	$=$
$h_2 \nearrow$	$\nearrow$	$\searrow$	$\nearrow$

Proof of Property 4.3: Two cases, $\omega A < \delta$ and $\omega A \geq \delta$ will be discussed accordingly.

1) When $\omega A < \delta$, from (4.16), since A, ω, τ and K are all positive, it is necessary for $h_2 > f_1$ to hold for the imaginary part of LHS to be negative.

2) When $\omega A \geq \delta$, from (4.21)$\sim$(4.26),

$$4h_2/(3A) - 4f_2/(3A) + 4f_3\delta/(3A) = \omega/K + f_3\omega > 0, \tag{4.32}$$

yielding

$$h_2 > f_2 - f_3\delta = f_0. \tag{4.33}$$

Note that $f_1 > f_2 > f_0$ physically. However, this necessary condition when $\omega A \geq \delta$ is too conservative and it may be tightened.

From above analysis, when $\omega A < \delta$, h_2 should be larger than f_1 to excite the limit cycle. Meanwhile, from Property 4.2, the velocity amplitude $A_v \approx \omega A$ increases monotonically w.r.t. h_2. Thus, when $\omega A \geq \delta$, h_2 should still be larger than f_1. Thus, $h_2 > f_1$ is a tighter necessary condition within the whole velocity span. □

Property 4.3 provides a simple guideline for tuning the DCR gains to attain a sustained limit cycle oscillation. i.e., if the choice of h_2 does not excite the limit cycle, h_2 is increased till the limit cycle appears.

Property 4.4. *Assume the initial values of h_1 and h_2 result in $A_v < \delta$ in steady state. When h_2 increases so that $A_v > \delta$, the amplitude of oscillation A will increase abruptly while the frequency of oscillation ω will reduce abruptly.* $\diamondsuit$

Proof of Property 4.4: Suppose h_1 is fixed, and h_2 is increased such that $\omega A \to \delta^-$ and the limit cycle is stable. Next, h_2 increases by a small increment Δ, which results in $\omega A > \delta$. From (4.17) and (4.18), the ratio of the frequencies of limit cycle after and before the variation is

$$\lim_{\Delta \to 0} w_2/w_1 = (1 + f_3 K) \lim_{\Delta \to 0} (h_2 - f_1)^2/(h_2 + \Delta - f_0)^2. \tag{4.34}$$

Note that when $A\omega \to \delta^-$, from (4.29),

$$h_2 = \delta/K + f_1. \tag{4.35}$$

Substituting (4.35) into (4.34) will yield

$$\begin{aligned} \lim_{\Delta \to 0} w_2/w_1 &= (1 + f_3 K)\delta K^{-1}/(\delta K^{-1} + f_1 - f_2 + f_3 \delta) \\ &< (1 + f_3 K)\delta K^{-1}/(\delta K^{-1} + f_3 \delta) = 1. \end{aligned} \tag{4.36}$$

This means ω will reduce abruptly with small variation of h_2 when ωA crosses δ.

Similarly, from (4.18) and (4.28), the ratio of amplitudes of limit cycle after and before the small increase in h_2

$$\lim_{\Delta \to 0} A_2/A_1 = (1 + f_3 K)^{-2} \lim_{\Delta \to 0} (h_2 + \Delta - f_0)^2/(h_2 - f_1)^2. \tag{4.37}$$

Substituting (4.35) into (4.37), it follows that

$$\lim_{\Delta \to 0} A_2/A_1 = \left[(\delta K^{-1} + f_1 - f_2 + f_3\delta)/((1 + f_3 K)\delta K^{-1})\right]^2$$
$$> \left[(\delta K^{-1} + f_3\delta)/((1 + f_3 K)\delta K^{-1})\right]^2 = 1. \quad (4.38)$$

This means A will increase abruptly with a small variation of h_2 when ωA crosses δ. □

Property 4.4 is rational physically, since when velocity exceeds δ, the friction abruptly decreases and the torque increases abruptly, so that the system has larger displacement vibration in this case compared with that when $\omega A < \delta$. This property provides a simple way to check whether the gains of DCR keeps the amplitude of velocity below δ at steady state.

4.5 Four-parameter Friction Modeling using DCR Feedback

The proposed procedure to yield the system model from relay feedback experiments can be deemed to comprise of two phases.

4.5.1 Low-velocity mode: Static friction identification

As discussed in the previous section, if the amplitude of velocity is kept below δ, (i.e., $\omega A < \delta$ holds), the DF of the friction model can be simplified as $N_{SR}(A) = 4jf_1/(\pi A)$, which is frequency independent. Thus, it is possible to estimate the generalized static friction model if $\omega A < \delta$.

In order to identify K, τ, and f_1, two relay experiments are to be conducted with the system operating in low-velocity mode with $\omega A < \delta$. The amplitudes and frequencies of

limit cycles are A_1, A_2 and ω_1, ω_2 accordingly, and the gains of relays are represented as h_{11}, h_{21}, h_{12} and h_{22} accordingly, where h_{ij} denotes the gain of the ith relay during the jth experiment. Following the procedures (4.13)$\sim$(4.15), it follows that

$$K = \pi(\omega_2 A_2 - \omega_1 A_1)/[4(h_{22} - h_{21})], \tag{4.39}$$

$$f_1 = (h_{21}\omega_2 A_2 - h_{22}\omega_1 A_1)/(\omega_2 A_2 - \omega_1 A_1). \tag{4.40}$$

Since there are four equations but only three unknowns, two equations are given to compute τ. An averaging approach is used, so that

$$\tau_l = 2K\left[h_{11}/(A_1\omega_1^2) + h_{12}/(A_2\omega_2^2)\right]/\pi, \tag{4.41}$$

where τ_l is the time constant of the linear dynamics of the system estimated in this first phase, with the system operating in a low velocity mode.

It is efficient to estimate the three parameters explicitly via (4.39)$\sim$(4.41). However, the estimation is based on the assumption that $\omega A < \delta$.

From a practical application viewpoint, there are two other considerations, apart from meeting the velocity requirement. First, it is noted that the frequency of oscillation ω should not be too large so as to reduce the sensitivity to noise and the need to use a higher sampling frequency. Secondly, the amplitude A of the output signal should not be too small to maintain an adequate signal-to-noise ratio (SNR). Property 4.2 shows that to meet the low velocity requirement, h_2 can be chosen to be relatively small. However, Property 4.1 shows that a reduced h_2 will increase the oscillation frequency and reduce the amplitude of position signals; both of these phenomenons may cause difficulties in a

practical application. However, a smaller h_1 can be chosen to cushion these effects, since with a smaller h_1, the amplitude of position signal can be increased and the frequency of oscillation can be decreased, while still maintaining the same velocity, according to Property 4.2. Properties 4.3 and 4.4 provide guidelines on the choice of gains to ensure that the limit cycle exists with $A_v < \delta$.

In summary, systematic set of procedures to select appropriate relay gains in the low-velocity experiments, from the properties investigated in Section 4.4, are prescribed as following:

1. Select a small enough h_2 to ensure $A_v < \delta$, by Property 4.2.

2. Select a small h_1 to reduce ω and increase A while maintain small A_v and an adequate SNR, by Property 4.1.

One may run this first phase of the relay experiments to operate the servomechanical system at as low a speed as sustainable and subsequently verify if the assumption holds after δ is obtained (Section 4.5.3).

4.5.2 High-velocity mode: Coulomb and viscous friction identification

When a servo-mechanical system operates in the high velocity mode, the dominant friction components influencing the motion are the Coulomb and viscous friction components. From Figure 4.2, the two-parameters friction model has been used as a good approximation of the four-parameters model. The second phase of the experiment will

aim to extract the two parameters of this model. The intersection f_0 of line l_2 and the f-axis is computed as $f_0 = f_2 - \delta f_3$. Thus, the friction model is expressed as

$$f = [f_0 + f_3|\dot{x}|]\,\mathrm{sgn}\,(\dot{x})\,. \tag{4.42}$$

Once f_0 and f_3 are determined, the remaining parameters f_2 and δ are related by $f_2 = f_3\delta + f_0$.

Similar to the procedures depicted in the last section, the DF of the equivalent relay (N_{ER}) is simply the sum of the individual DFs due to the feedback relays (N_{FR1}), (N_{FR2}) and the inherent system relay (N_{SR}), i.e., $N_{ER} = N_{FR1} + N_{FR2} + N_{SR}$, where $N_{FR1}(A) = 4h_1/(\pi A)$, $N_{FR2}(A) = -4jh_2/(\pi A)$, $N_{SR}(A,\omega) = j\,(4f_0/\pi A + \omega f_3)$. Thus,

$$N_{ER}(A,\omega) = 4h_1/(\pi A) + j\,[4(f_0 - h_2)/(\pi A) + \omega f_3]\,. \tag{4.43}$$

Under relay feedback, the amplitude and oscillating frequency of the resultant limit cycle is approximately given by the solution to (4.15). By varying h_1 and/or h_2, two relay experiments are conducted, yielding three explicit formulas from which the unknown time constant τ, generalized Coulomb friction f_0 and viscous friction f_3 are computed, since the static gain K has already been estimated during the first phase of the experiment.

$$\begin{bmatrix} f_0 \\ f_3 \end{bmatrix} = \begin{bmatrix} 4/(\pi A_1)\ \omega_1 \\ 4/(\pi A_2)\ \omega_2 \end{bmatrix}^{-1} \begin{bmatrix} 4h_{21}/(\pi A_1) - \omega_1/K \\ 4h_{22}/(\pi A_2) - \omega_2/K \end{bmatrix}, \tag{4.44}$$

where h_{ij} denotes the gain of the ith relay in the jth experiment.

From the same data set, the time constant τ_h of the linear dynamics canis also esti-

mated in the high-velocity mode.

$$\tau_h = 2K\left[h_{11}/(A_1\omega_1^2) + h_{21}/(A_2\omega_2^2)\right]/\pi. \tag{4.45}$$

Then, an average value of the time constant τ is computed from τ_l and τ_h as $\tau = (\tau_l + \tau_h)/2$.

It should be noted that an additional step can be taken to improve the estimation accuracy associated with this describing function approach which assumes a sinusoidal input. The velocity waveform is not sinusoidal generally but closer to an repeated isosceles triangle waveform in this mode. As shown in Figure 4.6, assuming the amplitude of the position signal is A, and approximating the velocity signal as a repeating isosceles triangle waveform, the amplitude of velocity signal A_v signal is more accurately expressed as

$$A_v \approx 4\omega A/\pi. \tag{4.46}$$

For this reason, a correction factor of $4/\pi$ can be multiplied to the second term in N_{SR}, to improve the estimation accuracy of DF, yielding $\bar{N}_{SR}(A,\omega) = j\left[4f_0/(\pi A) + 4\omega f_3/\pi\right]$. Thus, $\bar{N}_{ER}(A,\omega) = 4h_1/(\pi A) + j\left[4(f_0 - h_2)/(\pi A) + 4\omega f_3/\pi\right]$. With this correction factor, f_0 and f_3 can be identified as

$$\begin{bmatrix} f_0 \\ f_3 \end{bmatrix} = \begin{bmatrix} 4/(\pi A_1) & 4\omega_1/\pi \\ 4/(\pi A_2) & 4\omega_2/\pi \end{bmatrix}^{-1} \begin{bmatrix} 4h_{21}/(\pi A_1) - \omega_1/K \\ 4h_{22}/(\pi A_2) - \omega_2/K \end{bmatrix}. \tag{4.47}$$

After the second phase, two parameters f_2 and δ are left, but f_2 is computed from $f_2 = f_0 + \delta f_3$, after δ is obtained through an optimization process in Section 4.5.3.

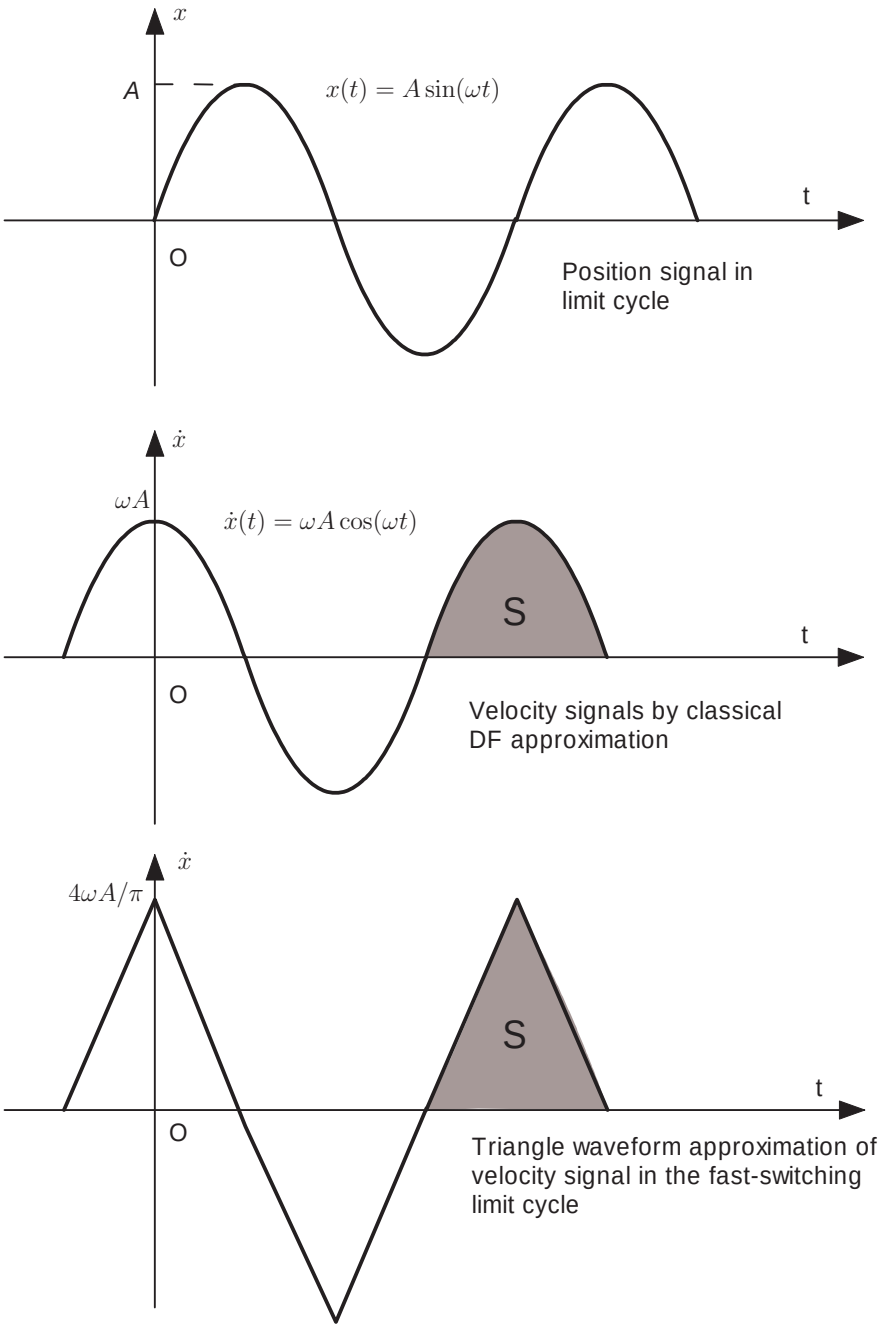

Figure 4.6: Improvement of velocity amplitude estimation.

4.5.3 Estimating the boundary lubrication velocity by optimization

The boundary lubrication velocity δ is estimated via an offline optimization process. This will be a single parameter optimization process, since the other friction parameters f_0, f_1 and f_3 are now known and f_2 is a function of δ only too, i.e., $f_2 = f_0 + \delta f_3$.

The harmonic balance condition is rewritten as $N_{ER}(A, \omega) = -1/G_p(j\omega)$, since the reciprocal of $G_p(j\omega)$ is more easily computed than $N_{ER}(A, \omega)$. The objective is to locate a parameter $\hat{\delta}$ which will minimize a performance index

$$J(\hat{\delta}) = \sum_{n=1}^{m} \Big\{ \Big[\mathbf{Re}(N_{ER}(A_n, \omega_n, \hat{\delta})) + \mathbf{Re}\left(1/G_p(j\omega_n)\right) \Big]^2 + \Big[\mathbf{Im}(N_{ER}(A_n, \omega_n, \hat{\delta})) + \mathbf{Im}\left(1/G_p(j\omega_n)\right) \Big]^2 \Big\}, \tag{4.48}$$

where G_p and N_{ER} are expressed as in (4.14) and (4.19), m is the total number of data sets from the relay experiments. The optimization process will sweep δ over a range and identify the optimal δ as the value which minimizes J. From Figure 4.2, a bound is further fixed for δ as $0 < \delta < \delta_u$, where $\delta_u = (f_1 - f_0)/f_3$. Compared to the estimation of four parameters concurrently via optimization as in [55], the single parameter optimization proposed here which is done offline on existing data sets is far more efficient and reliable.

Remark 4.3. *δ is the velocity threshold, separating the low and high velocity modes of the two phases of experiments. Thus, to estimate δ accurately, data samples should be taken from both sets of experiments, with $\omega A < \delta$ and $\omega A > \delta$.* $\diamondsuit$

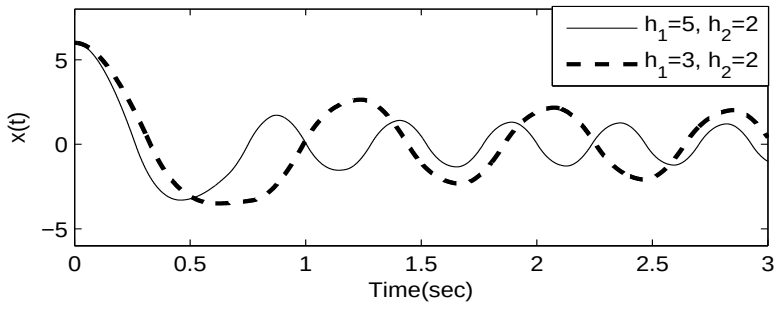

(a)

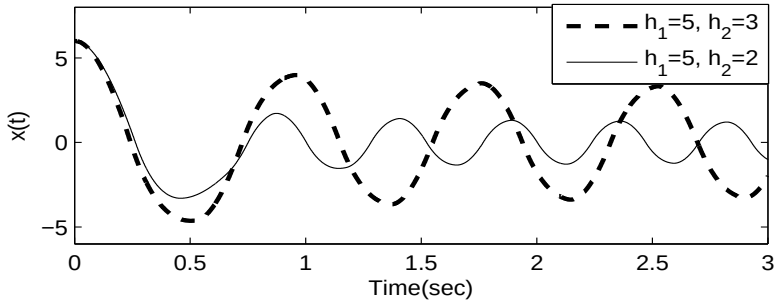

(b)

Figure 4.7: Investigation of limit cycles of $x(t)$ with choices of different relay gains.

4.6 Simulation

To elaborate the modeling phases systematically and to highlight the accuracy achievable, consider a servo-mechanical system described as $G_p(s) = 10/[s(0.2685s + 1)]$ with the four friction parameters given by $f_1 = 0.6$, $f_2 = 0.5$, $f_3 = 0.01$ and $\delta = 0.1$.

4.6.1 Limit cycle variation with relay gains

This subsection will highlight how the limit cycle oscillations in the system can vary with different choice of relay gains, and how the guidelines given by the properties of the relay in Section 4 can be used to position the two phases of the relay experiments in the proper velocity range.

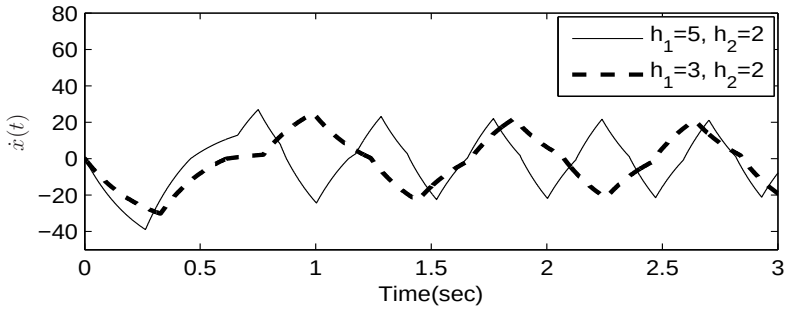

(a)

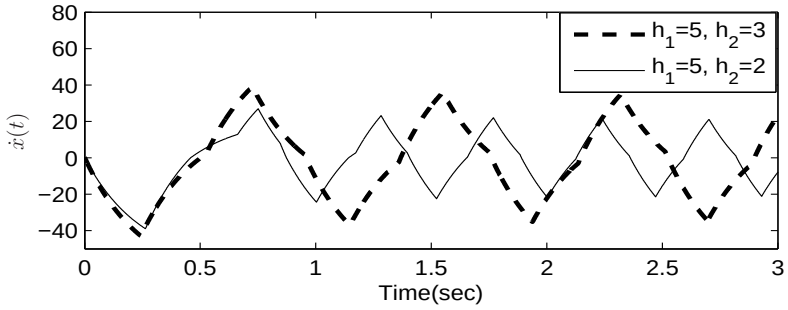

(b)

Figure 4.8: Investigation of limit cycles of $\dot{x}(t)$ with choices of different relay gains.

Property 4.1 is verified through the simulation results as shown in Figure 4.7. Comparing Figure 4.7(a) with Figure 4.7(b), it is observed that when h_1 increases, A decreases and ω increases, while h_2 behaves in the opposite manner. Similarly, Figure 4.8(a) and Figure 4.8(b) show the validity of Property 4.2, i.e. the oscillation amplitude of velocity is invariant with h_1, but it increases with h_2.

Moreover, four sets of relay gains are selected to show four different scenarios as depicted in Figure 4.9(a)$\sim$4.9(d).

In the first scenario as depicted in Figure 4.9(a), $h_2 < f_1$ and no sustainable limit cycle oscillation occurs (Property 4.3).

Figure 4.9(b) shows the scenario when the gains of the relay are sufficiently small to

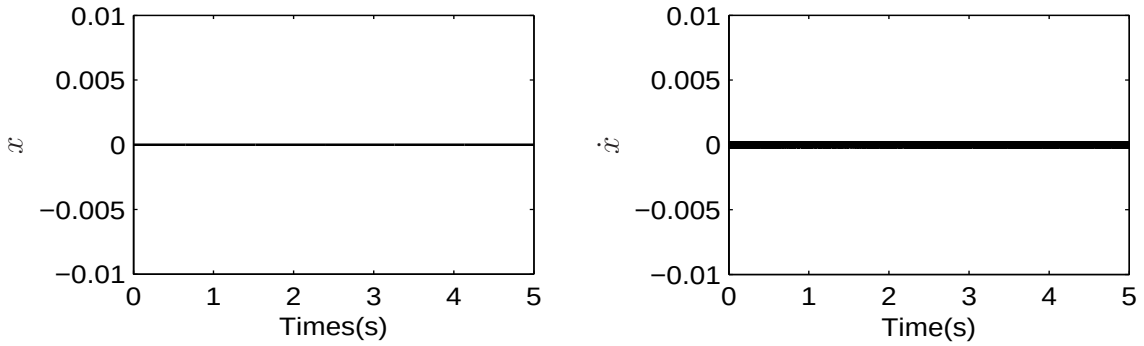

(a) $h_1 = 0.01$, $h_2 = 0.58$ (Scenario 1).

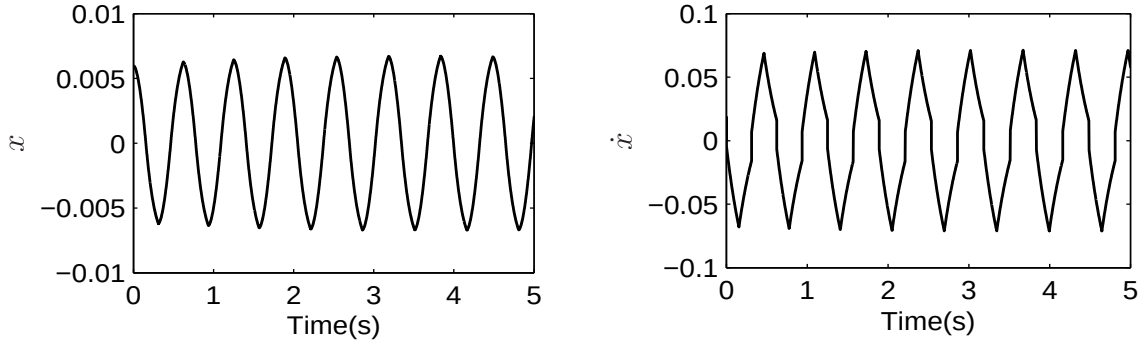

(b) $h_1 = 0.01$, $h_2 = 0.605$ (Scenario 2).

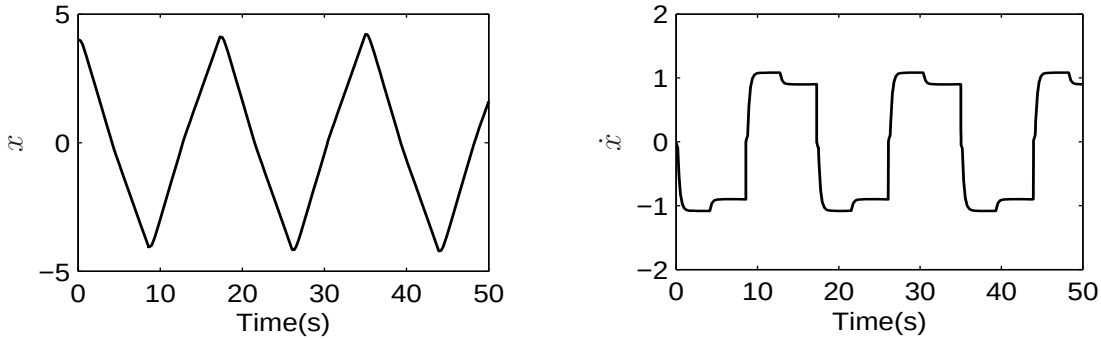

(c) $h_1 = 0.01$, $h_2 = 0.608$ (Scenario 3).

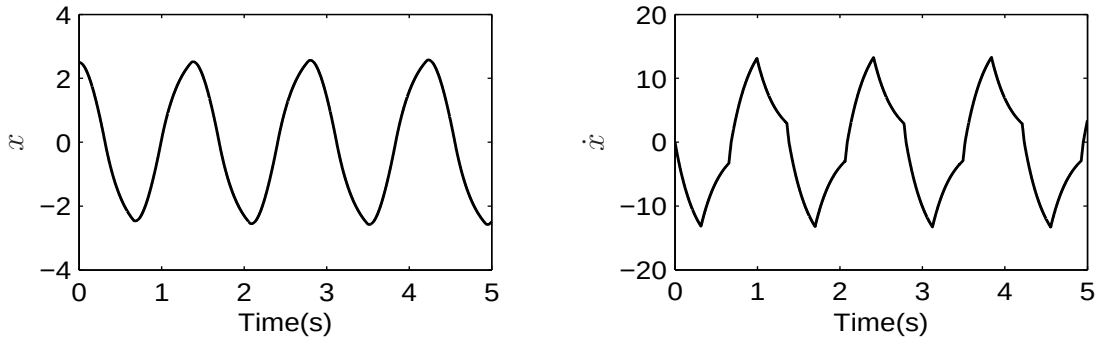

(d) $h_1 = 1$, $h_2 = 1.5$ (Scenario 4).

Figure 4.9: Four limit cycle scenarios w.r.t. different choices of relay gains.

maintain $A_v < \delta$. In this case, the output signal $x(t)$ exhibits a relatively fast switching phenomenon, and it has a sinusoidal waveform. The velocity signal has a triangular-shape periodic waveform.

Figure 4.9(c) presents the scenario when the gains of the relay are still kept small, but now $A_v > \delta$, the frequency of the waveform $x(t)$ decreases significantly while its amplitude increases significantly. Now, $x(t)$ has a triangular-shape periodic waveform, while $\dot{x}(t)$ resembles a pulse train (Property 4.4).

Figure 4.9(d) shows the scenario when the gains of the relay become relatively larger and $A_v > \delta$. The limit cycle becomes fast-switching again, and the velocity waveform has recovered the triangular-shape waveform.

The second scenario corresponds to the first phase of the modeling experiment. The fourth scenario corresponds to the second phase of the modeling experiment. From the velocity diagrams, it also shows that the velocity waveforms are more similar to isosceles triangle waveforms in these two scenarios. Thus, (4.47) will give better estimation results than (4.44).

4.6.2 Phase 1: Low velocity mode

Following the tuning procedures proposed in Section 4.5, by choosing $h_{11} = 0.01$, $h_{21} = 0.605$, $h_{12} = 0.01$ and $h_{22} = 0.603$, the position signals obtained fall in the second scenario, and it yields $\omega_1 = 8.763$, $A_1 = 7.58 \times 10^{-3}$ and $\omega_2 = 14.06$, $A_2 = 2.599 \times 10^{-3}$. By (4.39)$\sim$(4.41), the static friction parameter is correctly identified as $\hat{f}_1 = 0.6001$, while the linear dynamics parameters are identified as $\hat{K} = 9.9382$ and $\hat{\tau}_l = 0.2399$.

Table 4.3: Summary of parameter estimation.

Parameter	True	Estimated	Error
f_1	0.6000	0.6001	0.017%
f_2	0.5000	0.4865	2.700%
f_3	0.0100	0.0129	29.000%
δ	0.1000	0.0900	10.000%
K	10.0000	9.9382	0.618%
τ	0.2685	0.2557	4.770%

4.6.3 Phase 2: High velocity mode

In this phase, both DCR gains h_1 and h_2 should be large enough to ensure that the velocity is higher than the boundary lubrication velocity δ, as well as to keep the oscillation frequency sufficiently high. Choosing $h_{11} = 5$, $h_{21} = 3$, $h_{12} = 3$ and $h_{22} = 2$, two relay experiments are conducted, yielding $\omega_1 = 8.5023$, $A_1 = 3.23$ and $\omega_2 = 8.5486$, $A_2 = 1.935$. Through (4.45) and (4.44), the parameters are successfully identified as $\hat{\tau}_h = 0.2714$, $\hat{f}_0 = 0.4853$ and $\hat{f}_3 = 0.0166$. The estimation of f_3 can be further improved by applying (4.47) rather than (4.44), yielding $\hat{f}_3 = 0.0129$. The final estimation of the time constant is $\hat{\tau} = (\hat{\tau}_l + \hat{\tau}_h)/2 = 0.2557$.

4.6.4 Estimation of δ via optimization

The boundary lubrication velocity δ is identified using the optimization method discussed in Section 4.5.3. Six sets of relay experiment data are used with the system operating in both the low and high velocity modes. The bounds for δ are worked out to be within $(0, (\hat{f}_1 - \hat{f}_0)/\hat{f}_3)$, i.e., $(0, 8.89)$. Using the optimization method discussed in Section

4.5.3, the optimal $\hat{\delta}$ within $(0, 8.89)$ which will minimize the loss function $J(\hat{\delta})$ is found. With all other parameters being identified after the two phases, δ is correctly identified as $\delta_{opt} = 0.09$ with the corresponding minimum performance index $J_{min} = 149.87$. It should be noted that this optimization is done offline on existing sets of data, so there is no need to run extensive and additional experiments for this purpose. Finally, after $\hat{\delta}$ is obtained, $\hat{f}_2$ is directly obtained as $\hat{f}_2 = \hat{f}_0 + \hat{f}_3\delta_{opt} = 0.4865$.

The actual and estimated values of parameters are compared in Table 4.3.

4.7 Real-Time Experiments

To illustrate the effectiveness of the proposed method, real-time experiments are carried out on a precision 3D cartesian robotic system [91], as shown in Figure 4.10. Every axis of the robot is driven by a linear electric motor manufactured by Anorad Co., USA. The dSPACE control development and rapid prototyping system, in particular, the DS1103 board, is used. dSPACE integrates the whole development cycle seamlessly into a single environment. MATLAB and SIMULINK are directly used in the development of the dSPACE real-time control system. This experiment aims to identify the friction parameters of Y-axis servo. For simplicity, the X-axis and Z-axis are fixed on desired positions so that the weight of the loads is evenly distributed on two tracks of the Y-axis, and the disturbance to the Y-axis displacement due to the sliding of other two axis is negligible.

Several relay experiments are conducted according to the procedures described in

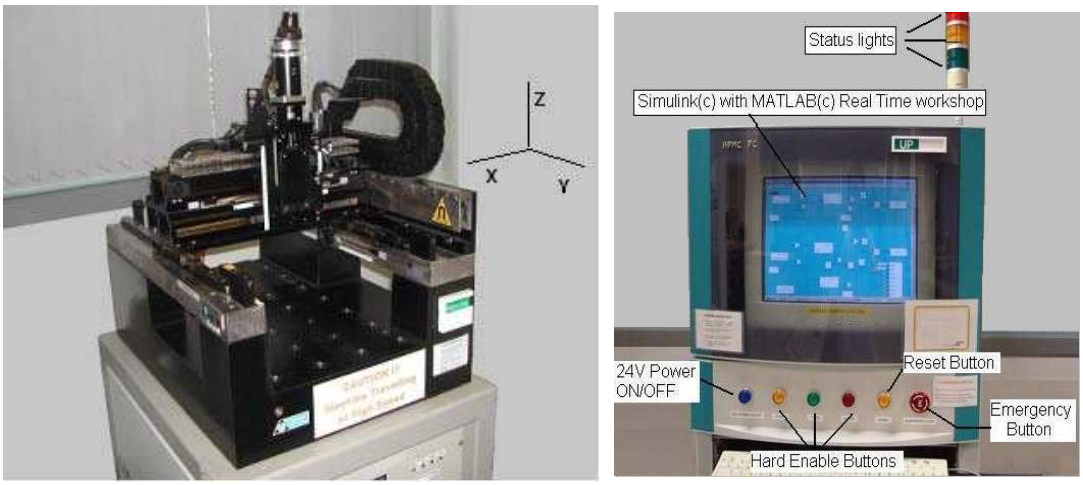

(a) (b)

Figure 4.10: Experiment set-up. (a) 3D cartesian robotic system. (b) Computer control platform.

Section 4.5. The unit of displacement is set to be mm. The motor parameters are identified as $K = 579.8480$ and $\tau = 0.6794$, while the friction parameters are identified as $f_1 = 0.3067$, $f_2 = 0.2688$, $f_3 = 1.1087 \times 10^{-4}$ and $\delta = 14.5$. Typically, two patterns of oscillation with choices of different relay gains, under influence of static and Coulomb/viscous frictions accordingly, are shown in Figure 4.11 and 4.12, which correspond to Scenario 2 and 4 as discussed in Section 4.6.

With the model parameters, a linear feedback controller is commissioned and the feedforward model-based friction compensator is properly initialized as illustrated in Figure 4.13. Since the tracking trajectory is time-varying sinusoidal, and the system itself is a type-1 system, integral controller is not necessary. By selecting controller parameters as $k_p = 0.005$, $k_d = 0.001$, Figure 4.14(b) shows the tracking error under the feedback-feedfoward control scheme to a sinusoidal reference $r(t) = 50 \sin t$ (unit in

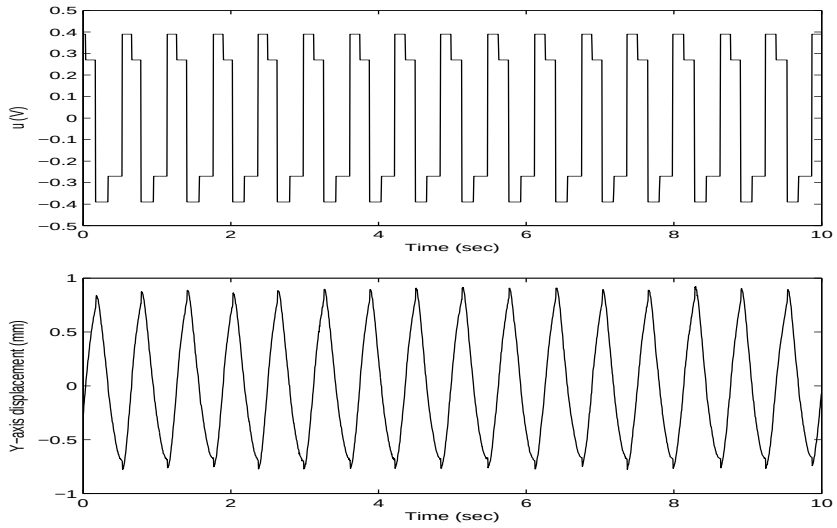

Figure 4.11: Input and output signal with $h_1 = 0.06$, $h_2 = 0.33$ (low velocity mode).

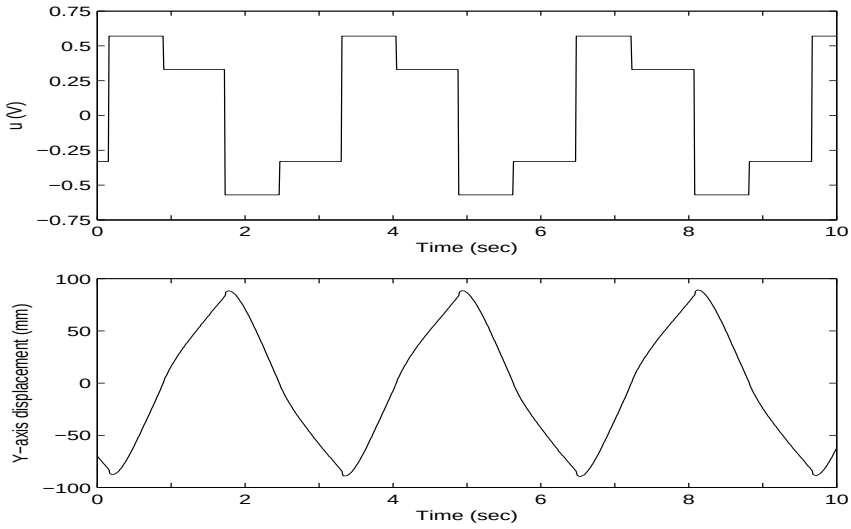

Figure 4.12: Input and output signal with $h_1 = 0.12$, $h_2 = 0.45$ (high velocity mode).

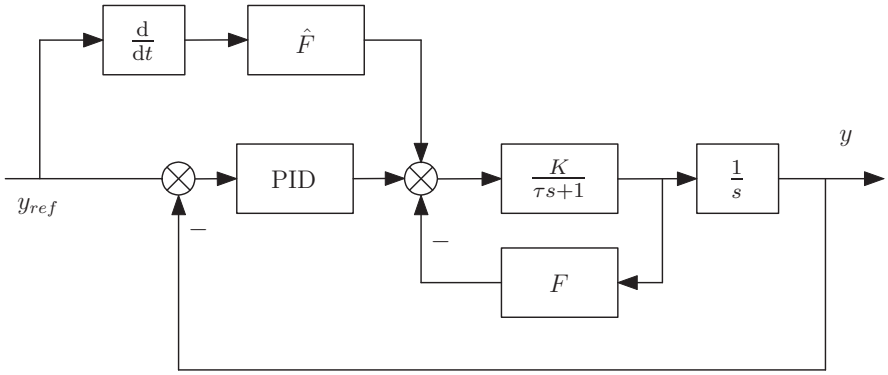

Figure 4.13: PID controller with friction pre-compensator.

mm). For a fair comparison, the tracking performance under same feedback controller but without feedforward friction compensator is shown in Figure 4.14(a). And it can be concluded that the tracking performance under normal linear feedback controller is not satisfactory, since under the effects of friction, the linear controller cannot cope with bidirectional, time-varying trajectory well. With adding in the model-based friction compensator, the maximum tracking error is reduced from 0.3mm to 0.06mm. Clearly, a significant improvement in reduction of the tracking error is achieved with the friction compensator. The remaining error may be due to ripple forces and other unmodeled uncertainties in the linear motor.

4.8 Conclusion

In this chapter, a new approach for the estimation of friction parameters in servomechanical systems has been developed using a DCR apparatus. A two-segment, four-parameter friction model is considered, since it is able to describe friction behavior of long-distance travel machine more precisely. Four important properties related to limit cycles in this

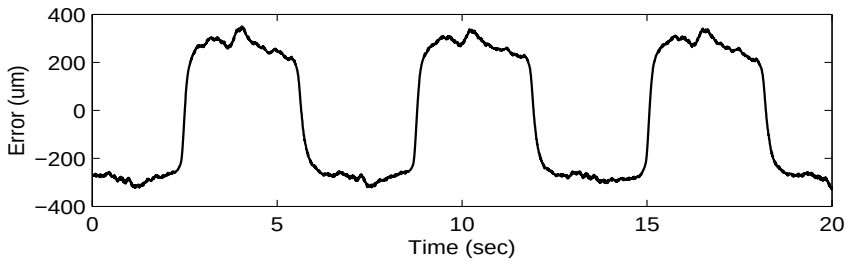

(a)

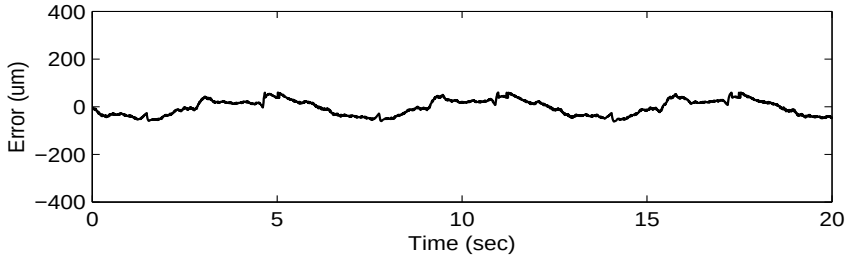

(b)

Figure 4.14: Closed-loop tracking performance. (a) Without friction compensator. (b) With friction compensator.

DCR feedback apparatus are investigated, which form the foundations of the two-phase identification procedures. A position feedback loop is used, instead of velocity feedback one. Hence, no additional filter is required. With closed-loop relay experiments, this method is able to identify most of model parameters by sets of explicit formulae, minimizing the use of nonlinear optimization and reducing the computational intensity. The model obtained is also directly applicable to a fine-tune linear controller with a feed-forward friction compensator, which results better tracking performance. Results from the simulation and real-time experiment have verified the applicability of the proposed method. However, the four-parameter friction model being identified in this chapter does not consider friction force under a zero-velocity condition. For the machine in the sticky states, a dynamical friction model is recommended since it will be better to describe the

system behavior more precisely [10] [45]. Where the static feedforward controller cannot achieve perfect tracking, due to existence of other unmodeled uncertainties; an adaptive sliding controller can be considered to ensure the tracking error is within the predetermined boundary [89]. The model parameters in the adaptive controller can be initialized by the values obtained from relay-based identification method, so that tracking errors will attenuate faster. For other types of permanent magnet linear motors (PMLMs) beyond the U-channel linear motors using in the 3-D Cartesian Robot System in this chapter, the strong force ripples are presented besides friction. In next chapter, the existing DF identification method will be extended to cope with such nonlinearity.

Chapter 5

Modeling and Compensation of Ripples and Friction in Permanent Magnet Linear Motors using Hysteretic Relay Feedback

5.1 Introduction

Permanent magnet linear motors (PMLMs) are now widely used in the precision manufacturing industries since among the electric motor drives, they are probably the most suitable choice for applications involving high-speed, high-precision motion control [91]. The main benefits of a PMLM include the high force density achievable, low thermal losses and the high precision and accuracy associated with the simplicity in mechanical structure. PMLM is designed by cutting and unrolling their rotary counterparts, resulting in a flat linear motor that produces linear force, as opposed to torque. Compared to asynchronous linear induction motors, PMLM incorporates rare earth permanent magnets is able to develop much higher flux without significant heating. Compared with their rotary counterparts, the linear motors require no indirect coupling mechanisms

like ball-screwing, which greatly reduce the contact type nonlinearities, such as friction and backlash, especially when they are used with aerostatic or magnetic bears. However, as trade-off to the direct drive benefit, the tolerance towards the effects of uncertainties and external disturbances is diminished [13]. Therefore, a reduction of these effects, either through proper physical design or via the control system, is of paramount importance if high-speed and high-precision motion control is to be achieved. This chapter just aims to model and compensate force ripples and friction in a typical PMLM, with assistant of hysteretic relay feedback.

5.1.1 Design of PMLM

There are several designs of PMLMs available commercially today, mainly force-platen, U-channel and tubular, etc [93].

Force-platen linear motor Force-platen linear motor, as shown in Figure 5.1 [80], consists of a moving platen and a stationary platen. The moving platen consists of induction coils with winding and iron core, while permanent magnets are placed on the stationary platen oriented at a right angle to the thrust axis, but slightly skewed in the vertical plane to reduce the thrust ripple. Force-platen motors feature a low-height profile and a wide range of available size. The application include automobile and machine tools applications where high continuous and peak forces are required. However, an iron core results in strong "coggy" movement due to the presence of detent (or cogging) force. The thermal energy also induces due to eddy current in iron core

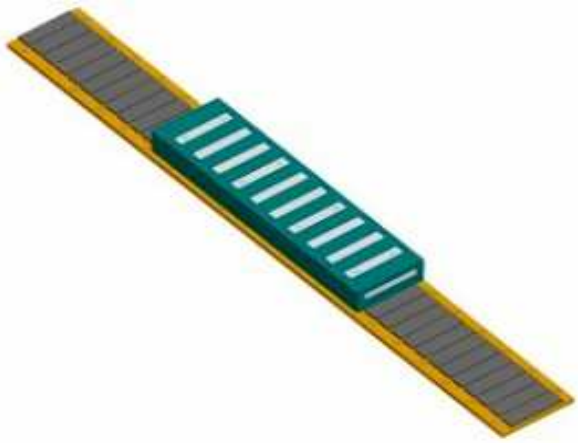

Figure 5.1: Force-platen linear motor.

which are a function of motor velocity. For efficient heat dissipation, the forced cooling is required in stringent applications. In addition, the magnetic flux is not fully utilized in force-platen design. And the installation process is relatively complex due to the requirement of precise air gap for generating consistent output force.

U-channel linear motor The U-channel linear motor has two parallel magnet track facing each other between the plates [2] [75]. Figure 5.2 shows a typical X-Y table driven by U-channel linear motors, which is made by Winnermotor Inc. The 3-D cartesian robotic system used in Chapter 4 experiment is designed with U-channel linear motor too. In such design, the forcer is supported by the magnet track by a bearing system. The forcers are ironless. This assembly has low mass, allowing for very high acceleration. The ironless forcer also ensures little cogging force is generated between forcer and magnet track. This design of linear motor has reduced magnetic flux leakage compared with force-platen design, since the magnets face each other and are housed in a U-shaped channel. This also minimizes the risks of being trapped by external powerful magnets.

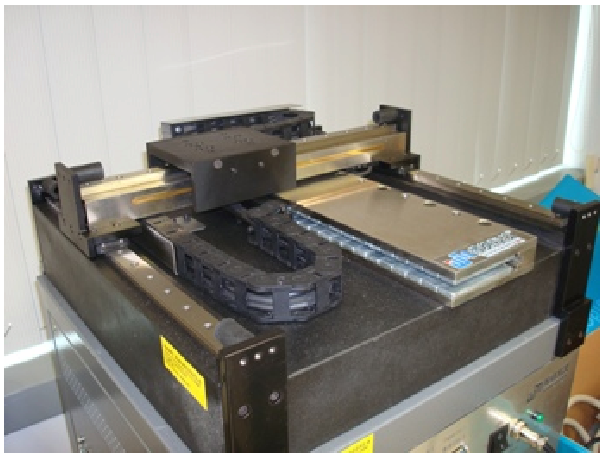

Figure 5.2: U-channel linear motor.

Furthermore, U-channel linear motors offer cost effective solution for long travel length motion control since there is no precision air gap requirements between the forcer and the plate. The major drawback of this design includes low-stiffness of the epoxy-filled armature plate which might lead to resonance under servo control in high acceleration applications.

Tubular linear motor This design of linear motor consists of a stationary thrust rod and a moving thrust block. One of the example is the LD3810 tubular motor, as shown in Figure 5.3. The thrust rod is a permanent magnet while the thrust block is an electromagnet winding. This design confers several advantages compared with the other linear motor types by its radial symmetry of the tubular geometry. First, the attractive force between the translator and stator are minimized by such geometry. Second, The linear force are maximizes by the perpendicularity between the circular windings in the thrust block and the magnetic flux pattern. Third, eddy current losses are insignificant due to the slot-less design. Furthermore, the thrust block is design to serve as a radiator

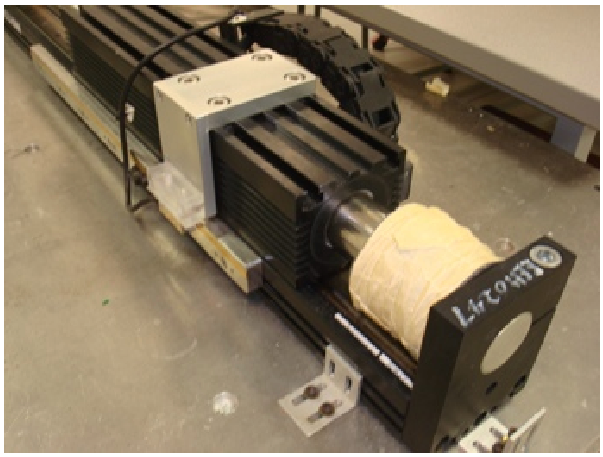

Figure 5.3: Tubular linear motor.

for passive cooling. The installation is simpler by its relatively large allowance of air gap. However, the current commercial tubular linear motor has tall over-height. Moreover, since in this design, the only point of supporting the stator is at the ends, there will always be a limit to length before the deflection in the bar causes the magnets to contact the forcer. In later part of this chapter, the force ripple and friction will be modeled and subsequently compensated in one tubular PMLM.

5.1.2 Force ripples in PMLMs and existing modeling techniques

Specifically, the two major nonlinear phenomenon faced by a PMLM are the force ripples and friction. Force ripples are strong, position dependent forces arising from the magnetic structure of a PMLM. The two primary components of the force ripple are the cogging (or detent) force and the reluctance force. The cogging force arises as a result of the mutual attraction between the magnets and iron cores of the translator [18]. Notice that this force exists even in the absence of any winding current and it exhibits a periodic

relationship with respect to the position of the translator relative to the magnets. The reluctance force is due to the variation of self-inductance of the windings with respect to the relative position between the translator and the magnets. Thus, it also has a periodic relationship with the translator-magnet position.

As mentioned in various designs of PMLMs in Section 5.1.1, force ripple is highly undesirable in motion control, since it will create "bumps" along the direction of motion. Additionally, frictional force arises from the contact between the translator and the track [7]. The limit cycle oscillation induced by friction causes small tracking errors in steady states, and it also limit the achievable closed-loop bandwidth [73]. Through alternate mechanical and material design, force ripples and friction may be kept to tolerable levels, but these approaches can be expensive and compromise on other specifications. An alternate approach is to suppress these nonlinear effects through the control system.

Till now, the control schemes proposed to compensate force ripples and friction can be classified into model-free and model-based ones. In [46] [65] [89] [90] [103], robust adaptive schemes are proposed to compensate friction and force ripples in PMLMs. In [88], a dither compensatory signal is generated based on a ripple model, which is identified using a simplex-optimized method. In [59] [96], learning controllers based on neural networks are applied to linear motors. An iterative learning controller (ILC) is formulated and applied in [106] with a regulated chatter, while a state-periodic adaptive compensation scheme is proposed in [4]. In [107], an adaptive feedforward controller employing a recursive least square (RLS) algorithm is proposed to identify and compensate the

force ripples in PMLM. However, the common drawback for these so called intelligent schemes is that it takes much time to learn and search the optimal parameters. In industrial applications, this drawback may not be acceptable and tuning and returning of controllers must be done efficiently. In this chapter, a relay feedback approach will be leveraged for modeling of the force ripples and friction present in a PMLM.

5.1.3 Motivations and novelty of new approach

Since 1980s, the application of relay feedback techniques to automatic tuning of controllers have been widely explored [10]. The limit cycles generated from RFS have been widely used in linear controller tuning [100] and identification of simple nonlinear friction models [16] [92]. In Chapter 4, a more complex, two-segment, four-parameter friction model [22] [23] [55] has been successfully identified, which includes Stricbeck effect in low-velocity mode with DCR feedback system. However, all the above relay-based methods are applicable only to identification of symmetric odd nonlinearities. For even nonlinearities, these methods cease to be applicable since the classical sinusoidal-input describing functions (SIDF) are not able to describe the biased limit cycles due to existence of even nonlinearities [36] [81]. The force ripple is one such even nonlinear phenomenon, which is usually represented as a single dominant harmonic of the load position, is not a pure odd-symmetric sine function generally [89]. If SIDF is still used to identify the force ripple strength, the reference point needs to be precisely adjusted to the positions with minimal force ripples, which is time-consuming. Otherwise, biased and asymmetrical limit cycle oscillations appear in the position signa with relay feedback, as observed by

simulations and experiment results in this chapter.

In this chapter, a new method is presented for the first time to model simultaneously both the force ripples and friction in the PMLM using a hysteretic relay, in addition to the linear dynamical parameters of the motor, by importing the dual-input describing function (DIDF) [36], which is able to handle sinusoid-alike limit cycle with bias, for model identification. The DIDF for the overall nonlinearities present in the feedback system, including the hysteretic relay added is derived. With this setup, all the system parameters, including the linear and nonlinear ones, are efficiently identified with only two relay experiments using a set of explicit formulae. Based on the correct model parameters, a simple model-based PD-feedforward compensation control scheme is commissioned to achieve improved tracking performance. Simulations and real-time experiments on a multiprocessor-dSPACE-controlled tubular PMLM platform have verified the applicabilities of this new method .

5.2 Overall PMLM Model

Consider a comprehensive model of PMLM, which combines the mechanical and electrical dynamics as in (4.1)$\sim$(4.3). The nonlinear forces f_{nl} in PMLM are represented as

$$f_{\text{nl}} = f_{\text{ripp}}(x) + f_{\text{fric}}(\dot{x}) + f_{\text{res}}(t). \tag{5.1}$$

where f_{fric} and f_{ripp} represent the friction and force ripple accordingly; f_{res} can be considered to be any other residual forces not considered, possibly arising from model un-

certainty and system disturbances present. It is assumed that f_{res} is much smaller than f_{fric} and f_{ripp}, so that it can be ignored.

The frictional force f_{fric} is represented by Coulomb and viscous friction components (with friction model parameters $\bar{f}_1$ and $\bar{f}_2$)

$$f_{\text{fric}} = \bar{f}_1 \text{sgn}(\dot{x}) + \bar{f}_2 \dot{x}. \tag{5.2}$$

The force ripple f_{ripp} is represented by a single dominant spatial frequency Ω sinusoidal function with phase shift ϕ.

$$f_{\text{ripp}} = C \sin(\Omega x + \phi) = \bar{C}_1 \cos(\Omega x) + \bar{C}_2 \sin(\Omega x). \tag{5.3}$$

In addition, since the electrical time constant is much smaller than the mechanical one, the dynamics due to electrical induction is omitted. Thus, the following equation describing the final model can be obtained

$$\ddot{x} = -\left(\frac{K_e K_f + \bar{f}_2 R}{RM}\right)\dot{x} + \frac{K_f}{RM}\left[u - \frac{\bar{f}_1 R}{K_f}\text{sgn}(\dot{x}) \frac{\bar{C}_1 R}{K_f}\cos(\Omega x) - \frac{\bar{C}_2 R}{K_f}\sin(\Omega x)\right]. \tag{5.4}$$

Set $a = (K_e K_f + R\bar{f}_2)/(RM)$; $b = K_f/(RM)$; $f = \bar{f}_1 R/K_f$; $C_1 = \bar{C}_1 R/K_f$; $C_2 = \bar{C}_2 R/K_f$. Furthermore, introduce

$$\tilde{u} = u - f\text{sgn}(\dot{x}) - C_1 \cos(\Omega x) - C_2 \sin(\Omega x), \tag{5.5}$$

so that the linear portion can be written as the following transfer function

$$G(s) = X(s)/\tilde{U}(s) = b/[s(s+a)]. \tag{5.6}$$

In this chapter, a intentional hysteretic relay feedback apparatus is added to induce oscillations from which to identify the system parameters, as shown in Figure 5.4. The

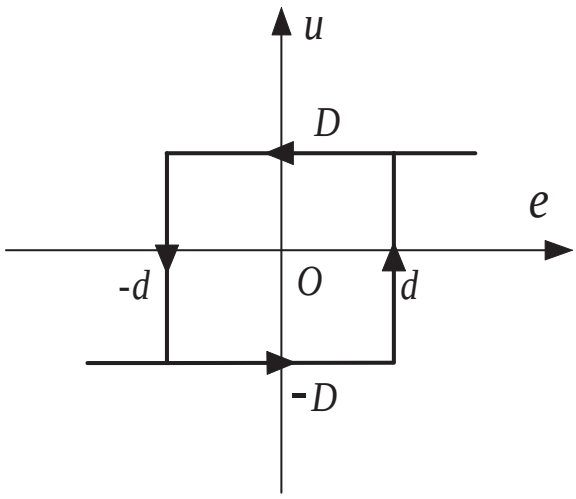

Figure 5.4: The hysteretic relay used for identification.

hysteretic relay is defined by [100] as

$$u = \begin{cases} D & \text{if } e > d, \text{ or } (e \geq -d \text{ and } u(t_-) = D) \\ -D & \text{if } e < -d, \text{ or } (e \leq d \text{ and } u(t_-) = -D) \end{cases}, \tag{5.7}$$

where $e = -x$ under assumption of zero reference input, without loss of generation. The full model, in a block diagram form, is illustrated in Figure 5.5.

5.3 Model Identification

In this section, the approach to identify the parameters associated with the full model presented in (5.5) and (5.6) will be elaborated. First, an equivalent block diagram model of PMLM will be presented, which segregate cleanly the linear and nonlinear parts of the model. DIDF will be used to approximately describe each of the nonlinear component in the block diagram, and subsequently combined into an overall DIDF. Then, with a harmonic balance analysis, explicit equations to obtain all the model parameters from resultant oscillations will be provided.

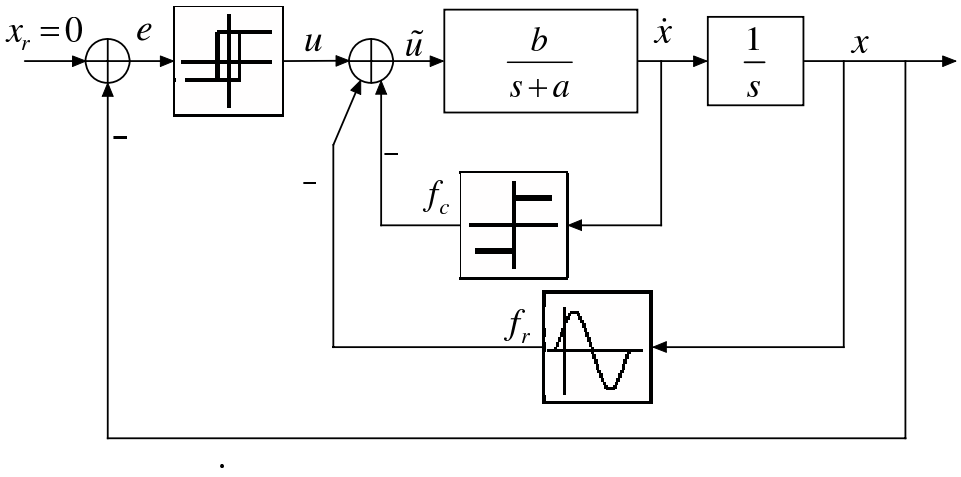

Figure 5.5: PMLM under hysteretic relay feedback.

5.3.1 Dual-input describing function (DIDF) for nonlinear portion of PMLM model

Since $e = -x$, (5.5) can be written as

$$\tilde{u} = u + f\text{sgn}(\dot{e}) - C_1 \cos(\Omega e) + C_2 \sin(\Omega e). \tag{5.8}$$

In other words, the overall system shown in Figure 5.5 can be converted to the equivalent form of Figure 5.6, so that the linear portion and nonlinear portion are cleanly segregated to facilitate subsequent harmonic balancing for parameter estimation.

In the equivalent system, the system nonlinearities, as well as the intentional relay, all use the error signal as the input, similar to [23]. In general, due to non-zero phase ϕ of force ripple in (5.3), there exists an even nonlinearity in the form of the cosine term. This causes asymmetrical oscillation. The simple sinusoidal-input describing function (SIDF), assuming symmetric sinusoidal input, is not able to describe such even nonlinearity. Thus, the dual-input describing function (DIDF) will be used in this

section to approximate each of the nonlinear component. In all of these approximations, a biased sinusoidal input $e(t) = A\sin\omega t + B$ is assumed, where A is amplitude, ω is the oscillating frequency and B is the bias [36].

Consider first the force ripple nonlinearity $f_{\text{ripp}} = -C_1\cos\Omega e + C_2\sin\Omega e$. The following theorem gives the DIDF of this nonlinearity.

Theorem 5.1. *The DIDF of nonlinearity $f_{ripp} = -C_1\cos\Omega e + C_2\sin\Omega e$ under biased sinusoidal input $e = A\sin\omega t + B$ is given by $N_{AR}(A,B)$ and $N_{BR}(A,B)$, where*

$$N_{AR}(A,B) = \frac{2}{A}\left[C_1\sin(\Omega B) + C_2\cos(\Omega B)\right]J_1(\Omega A); \tag{5.9}$$

$$N_{BR}(A,B) = \frac{2}{B}\left[-C_1\cos(\Omega B) + C_2\sin(\Omega B)\right]J_0(\Omega A); \tag{5.10}$$

where

$$J_n(z) = \frac{1}{\pi}\int_0^\pi \cos(n\theta - z\sin\theta)\mathrm{d}\theta, \qquad n \in \mathbf{N}, \tag{5.11}$$

is a Bessel function of the first kind of order n w.r.t. z.$\diamondsuit$

Proof of Theorem 5.1: First, consider the cosine nonlinearity in the force ripple, i.e., $f_{r1} = C_1\cos\Omega e$, under biased sinusoidal input $e = A\sin\theta + B$, where $\theta = \omega t$. The general equation for the limit cycle DIDF for a memoryless nonlinearity yields

$$\begin{aligned}
N_{AC}(A,B) &= \frac{C_1}{\pi A}\int_0^{2\pi}\cos\left[\Omega(A\sin\theta + B)\right]\sin\theta\,\mathrm{d}\theta \\
&= \frac{C_1}{\pi A}\int_0^{\pi}\left[\cos(\Omega A\sin\theta + \Omega B) - \cos(\Omega A\sin\theta - \Omega B)\right]\sin\theta\,\mathrm{d}\theta \\
&= \frac{2C_1\sin(\Omega B)}{\pi A}\int_0^{\pi}\sin(\Omega A\sin\theta)\sin\theta\,\mathrm{d}\theta \\
&= \frac{C_1\sin(\Omega B)}{\pi A}\int_0^{\pi}\left[\cos(\Omega A\sin\theta + \theta) - \cos(\Omega A\sin\theta - \theta)\right]\mathrm{d}\theta \\
&= -2C_1\sin(\Omega B)J_1(\Omega A)/A.
\end{aligned} \tag{5.12}$$

The DIDF relating to the bias term is given by

$$\begin{aligned} N_{BC}(A,B) &= \frac{1}{2\pi B}\int_0^{2\pi} C_1\cos[\Omega(A\sin\theta+B)]\,\mathrm{d}\theta \\ &= \frac{C_1}{2\pi B}\int_0^{\pi}[\cos(\Omega A\sin\theta+\Omega B)+\cos(\Omega A\sin\theta-\Omega B)]\,\mathrm{d}\theta \\ &= \frac{C_1\cos(\Omega B)}{\pi B}\int_0^{\pi}\cos(\Omega A\sin\theta)\,\mathrm{d}\theta \\ &= C_1\cos(\Omega B)J_0(\Omega A)/B. \end{aligned} \tag{5.13}$$

Next, consider the sine nonlinearity in the force ripple, i.e., $f_{r2} = C_2\sin\Omega e$, under biased input $e = A\sin\theta + B$, where $\theta = \omega t$. Similar to the cosine nonlinearity, it yields

$$\begin{aligned} N_{AS}(A,B) &= \frac{C_2}{\pi A}\int_0^{2\pi}\sin\left[\Omega(A\sin\theta+B)\right]\sin\theta\,\mathrm{d}\theta \\ &= \frac{C_2}{\pi A}\int_0^{\pi}[\sin(\Omega A\sin\theta+\Omega B)+\sin(\Omega A\sin\theta-\Omega B)]\sin\theta\,\mathrm{d}\theta \\ &= \frac{2C_2\cos(\Omega B)}{\pi A}\int_0^{\pi}\sin(\Omega A\sin\theta)\sin\theta\,\mathrm{d}\theta \\ &= \frac{C_2\cos(\Omega B)}{\pi A}\int_0^{\pi}\left[\cos(\theta-\Omega A\sin\theta)-\cos(-\theta-\Omega A\sin\theta)\right]\,\mathrm{d}\theta \\ &= 2C_2\cos(\Omega B)J_1(\Omega A)/A. \end{aligned} \tag{5.14}$$

Similarly, for the bias term,

$$\begin{aligned} N_{BS}(A,B) &= \frac{1}{2\pi B}\int_0^{2\pi} C_2\sin[\Omega(A\sin\theta+B)]\,\mathrm{d}\theta \\ &= \frac{C_2\sin(\Omega B)}{2\pi B}\int_0^{\pi}[\sin(\Omega A\sin\theta+\Omega B)-\sin(\Omega A\sin\theta-\Omega B)]\,\mathrm{d}\theta \\ &= \frac{C_2\sin(\Omega B)}{\pi B}\int_0^{\pi}\cos(\Omega A\sin\theta)\,\mathrm{d}\theta \\ &= C_2\sin(\Omega B)J_0(\Omega A)/B. \end{aligned} \tag{5.15}$$

Noting that $N_{AR} = -N_{AC} + N_{AS}$ and $N_{BR} = -N_{BC} + N_{BS}$, Theorem 5.1 is proofed.□

In Theorem 5.1, notice that B is the bias of the error signal, which has opposite sign to the bias of the position signal x.

For the hysteretic relay given by (5.7) under the biased sinusoidal input $e = A\sin\omega t + B$, the DIDF is given by

$$N_{AH}(A,B) = \frac{2D}{\pi A}\varpi(d,A,B) - j\frac{4Dd}{\pi A^2}, \tag{5.16}$$

$$N_{BH}(A,B) = \frac{D}{\pi B}\upsilon(d,A,B), \tag{5.17}$$

where

$$\varpi(d,A,B) = \sqrt{1-\left(\frac{d+B}{A}\right)^2} + \sqrt{1-\left(\frac{d-B}{A}\right)^2}; \tag{5.18}$$

$$\upsilon(d,A,B) = \sin^{-1}\frac{d+B}{A} - \sin^{-1}\frac{d-B}{A}. \tag{5.19}$$

For the Coulomb friction nonlinearity $f_c(\dot{e})$ given by $f_c = f\mathrm{sgn}(\dot{e})$, with the biased sinusoidal input $e = A\sin\omega t + B$, the DIDF is given by

$$N_{AF}(A,\omega) = 4jf/(\pi A); \tag{5.20}$$

$$N_{BF} = 0. \tag{5.21}$$

Here, the bias constant B is eliminated by the differentiator. Thus, the DIDF is equal to the SIDF as discussed in [23].

The overall DIDF of the nonlinear portion is thus given by

$$N_A = N_{AH} + N_{AR} + N_{AF}; \tag{5.22}$$

$$N_B = N_{BH} + N_{BR}. \tag{5.23}$$

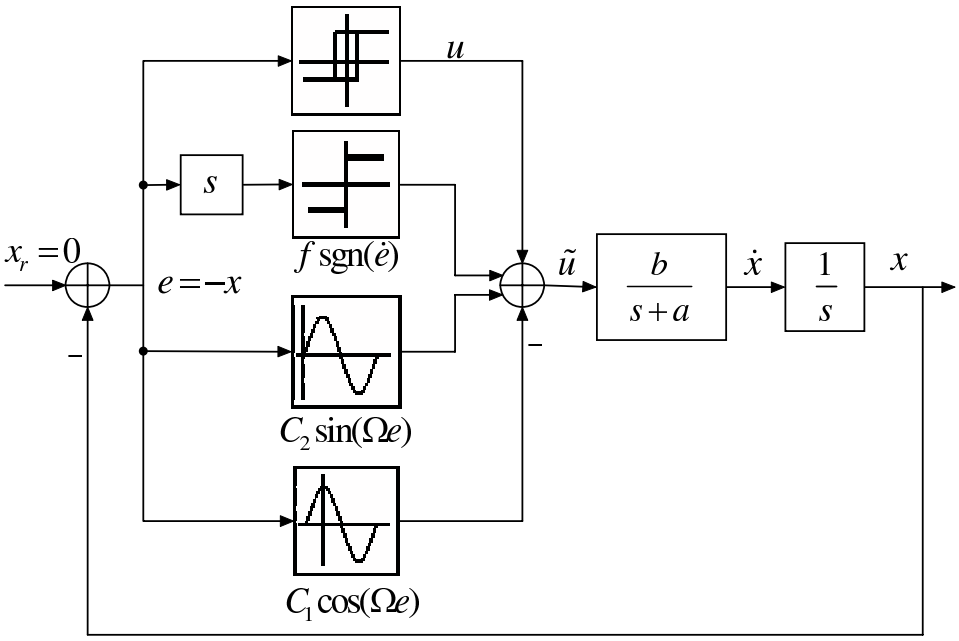

Figure 5.6: Equivalent block diagram.

5.3.2 Parameter estimation from harmonic balance

Note that the linear portion of PMLM model is a type-1 system. Thus, under the assumption of the existence of a biased sinusoidal limit cycle oscillation, the harmonic balance condition is given by [36] as

$$N_A(A, B, \omega)\, G(j\omega) = -1; \tag{5.24}$$

$$N_B(A, B, \omega) = 0. \tag{5.25}$$

With (5.24)$\sim$(5.25), together with (5.9)$\sim$(5.23), the following three equalities can be established,

$$4Dd/(\pi A^2) = \omega\alpha + 4f/(\pi A); \tag{5.26}$$

$$-2D\varpi/\pi = -A\omega^2\beta + 2\sin(\Omega B)J_1(\Omega A)C_1 + 2\cos(\Omega B)J_1(\Omega A)C_2; \tag{5.27}$$

$$-D\upsilon/[\pi J_0(\Omega A)] = -\cos(\Omega B)C_1 + \sin(\Omega B)C_2, \tag{5.28}$$

where $\alpha = a/b$, $\beta = 1/b$. Define A_j as the value of A obtained from the jth experiment, so as D_j, d_j, ϖ_j, υ_j, B_j and ω_j. Since five parameters are required to be identified, but only three equations are available, a minimum of two sets of relay experiments are required which can be obtained by varying the hysteretic relay parameters.

From (5.26), f and α are identified by

$$\alpha = \frac{4(D_1 d_1 A_2 - D_2 d_2 A_1)}{\pi A_1 A_2(\omega_1 A_1 - \omega_2 A_2)}; \tag{5.29}$$

$$f = \frac{A_1^2 \omega_1 D_2 d_2 - A_2^2 \omega_2 D_1 d_1}{A_1 A_2(\omega_1 A_1 - \omega_2 A_2)}. \tag{5.30}$$

C_1 and C_2 can be identified from (5.28) as

$$C_1 = \frac{J_0(\Omega A_2)\sin(\Omega B_2) D_1 \upsilon_1 - J_0(\Omega A_1)\sin(\Omega B_1) D_2 \upsilon_2}{\pi \sin[\Omega(B_2 - B_1)] J_0(\Omega A_1) J_0(\Omega A_2)}, \tag{5.31}$$

$$C_2 = \frac{J_0(\Omega A_2)\cos(\Omega B_2) D_1 \upsilon_1 - J_0(\Omega A_1)\cos(\Omega B_1) D_2 \upsilon_2}{\pi \sin[\Omega(B_2 - B_1)] J_0(\Omega A_1) J_0(\Omega A_2)}. \tag{5.32}$$

β is identified from (5.27) as

$$\beta = \sum_{j=1}^{2} \left[D_j \varpi_j + \pi \sin(\Omega B_j) J_1(\Omega A_j) C_1 + \pi \cos(\Omega B_j) J_1(\Omega A_j) C_2 \right] / (\pi A_j \omega_j^2). \tag{5.33}$$

Thus, a and b are finally obtained by $a = \alpha/\beta$ and $b = 1/\beta$.

5.3.3 Extraction of frequency components from DFT

Compared with the methods proposed in [23] [55] [92], the new method induces a bias term B in the limit cycle due to the presence of an even nonlinearity with respect to the input signal. This bias arises from asymmetry in the limit cycle. Thus, the amplitude and bias of the oscillation may not be directly obtained from the oscillation accurately

especially when the asymmetric is severe. Instead, discrete Fourier transform (DFT) [64] can be applied to obtain the fundamental frequency, based on which A and B can be extracted.

Without loss of generality, a peak-to-peak, N-samples segment $e_s(n)$ consisting of an exact m periods of limit cycles is taken from $e(t)$, so that the spectrum leakage is avoided. The bias B is estimated as the mean value of the periodic segment $e_s(n)$ of $e(t)$, or equivalently, the spectral component $E(0)$ divided by the sample size N,

$$B = \frac{1}{N}\sum_{n=0}^{N-1} e_s(n) = \overline{e_s(n)} = E(0)/N \tag{5.34}$$

Since m periods of signal segment is available, the amplitude A of fundamental frequency component is estimated as twice the real part of mth spectral components normalized by the sample size N,

$$\begin{aligned} A &= \frac{1}{N}\sum_{n=0}^{N-1} e_s(n)\left[\exp\left(-j\frac{2\pi nm}{N}\right) + \exp\left(j\frac{2\pi nm}{N}\right)\right] \\ &= \frac{2}{N}\sum_{n=0}^{N-1} e_s(n)\cos\left(\frac{2\pi nm}{N}\right) \\ &= 2\,\overline{e_s(n)\cos\left(2\pi nm/N\right)}. \\ &= 2\,\mathbf{Re}\left[E(m)\right]/N, \end{aligned} \tag{5.35}$$

5.4 Simulation

Consider the PMLM model of (5.5)∼(5.6), with parameters set as

$$a = 4,\, b = 40,\, \Omega = 0.2\pi,\, f = 0.4,\, C = 1. \tag{5.36}$$

The sampling interval of simulation is fixed as $0.1\,ms$. This section will first highlight

how the limit cycle oscillations are affected with different position phase shift ϕ. By choosing $\phi = 0$ and $\phi = \pi/6$, biased and unbiased limit cycles are observed in Figure 5.7 and Figure 5.8, accordingly, with the same fixed relay parameters $d = 1.2$, $D = 5$. When $\phi = 0$, there is no cosine term in the model of ripple nonlinearity, and the limit cycle is symmetric with period T. When $\phi = \pi/6$, non-odd ripple nonlinearity $f_r = \sin(0.2\pi x + \pi/6)$ is present, the duty time T^+ and T^- of high and low values of the relay output are not equal, and biased limit cycle oscillations occur.

In the following part, in order to verify the effectiveness of the new method, the parameters of hysteretic relay are chosen as $d_1 = 1.2$, $D_1 = 5$, $d_2 = 0.8$, $D_2 = 3$, to identify the system model of (5.5)$\sim$(5.6), with same parameter set as in (5.36), with $\phi = \pi/6$. The simulation results for the two limit cycles within five periods are shown in Figure 5.8 and Figure 5.9 accordingly. The asymmetry and bias in the oscillation are evident in these figures.

DFT is first applied to complete cycles of $e(t)$, beginning from when $e(t)$ is at maximum value and ending five complete periods later. The spectrum of the signals are shown in Figure 5.10. A and B can be obtained from (5.34)$\sim$(5.35). In this way, the frequency and amplitude of the fundamental harmonics, and DC bias are obtained as $\omega_1 = 10.2834$, $A_1 = 2.4639$, $B_1 = 0.1222$, $\omega_2 = 10.2099$, $A_2 = 1.4819$, $B_2 = 0.1763$. With the explicit equations given in (5.29)$\sim$(5.33), the system parameters are correctly identified as $a = 4.0089$, $b = 39.4076$, $C_1 = 0.4423$, $C_2 = 0.8810$, and $f = 0.4107$. Table 5.1 also shows that the error of estimation can be kept to be about 10% and below, which

Table 5.1: Summary of simulation results.

Parameter	Actual	Estimated	Error %
a	4.0	4.0089	0.22
b	40.0	39.4076	-1.48
C_1	0.5000	0.4423	-11.54
C_2	0.8660	0.8810	1.73
f	0.4	0.4107	-2.67

demonstrates the efficiency and applicability of the proposed method. From (5.31) and (5.32), the formulae of computing C_1 and C_2 only differ with each other by terms of $\sin(\Omega B)$ and $\cos(\Omega B)$. The error of estimation of C_1 is larger than C_2 since the gradient of $\sin(\Omega B)$ is steeper compared to $\cos(\Omega B)$, when ΩB is relatively small.

5.5 Real-Time Experiments

To illustrate the effectiveness of proposed method, real-time experiments are conducted on a PMLM at Singapore Institute of Manufacturing Technology (SIMTech), as shown Figure 5.11, using the dSPACE Alpha Combo multiprocessor control system with MATLAB Simulink Real-time Workshop. In this dual-DSP system, the dSPACE DS1004 DSP board is used for computational intensive tasks associated with execution of control algorithms; while the DS1003 DSP board is able to deal efficiently with all the necessary I/O tasks. Both boards are real-time interface enables and configured to give optimal performance via the decentralization. The overall block diagram of Simulink program used in this experiment is shown in Figure 5.12.

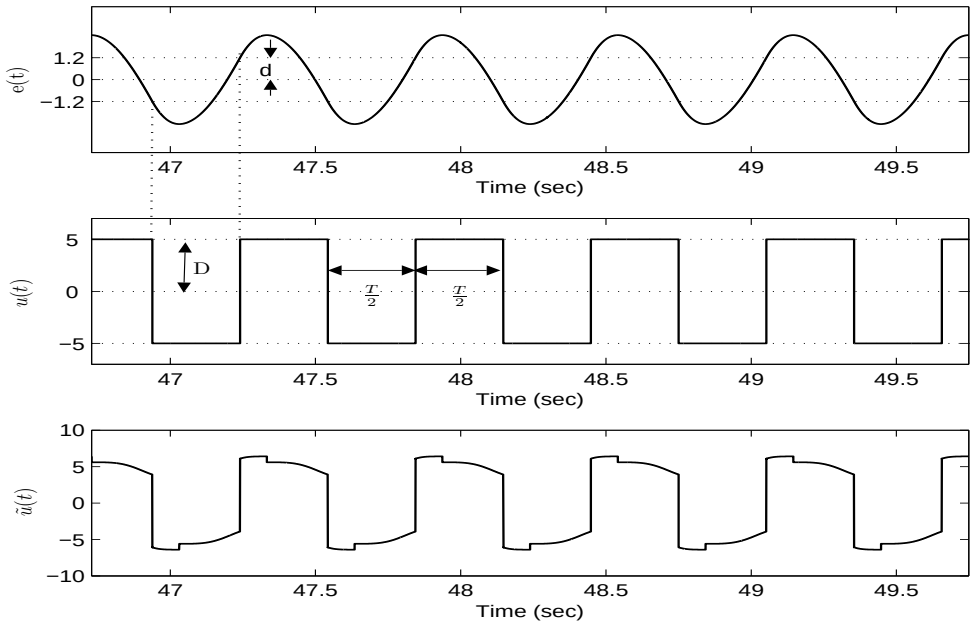

Figure 5.7: Input $e(t)$ and output $u(t)$ of the hysteretic relay and actual control signal $\tilde{u}(t)$ with $d = 1.2$, $D = 5$, $\phi = 0$.

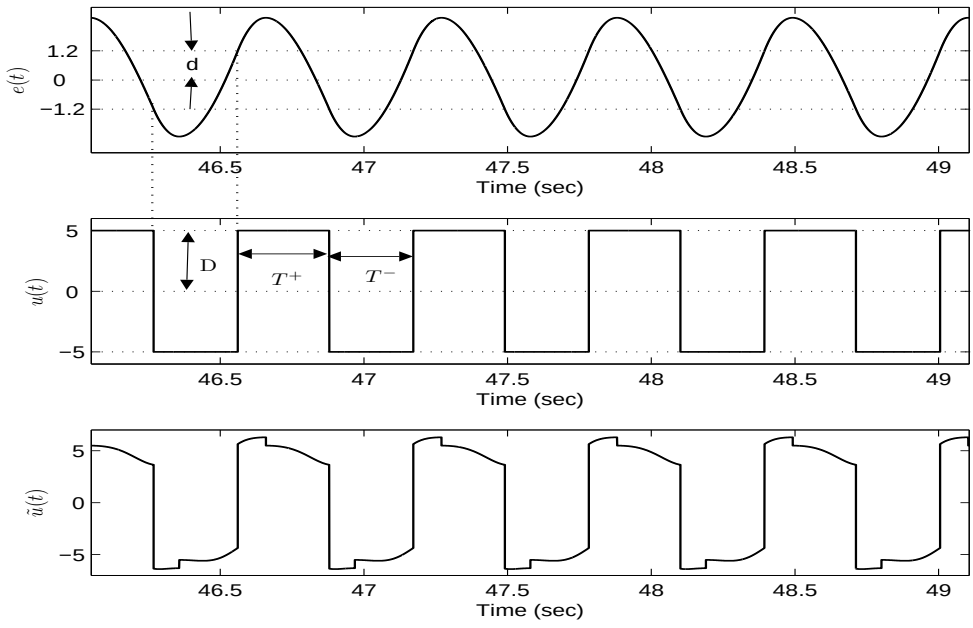

Figure 5.8: Input $e(t)$ and output $u(t)$ of the hysteretic relay and actual control signal $\tilde{u}(t)$ with $d = 1.2$, $D = 5$, $\phi = \pi/6$.

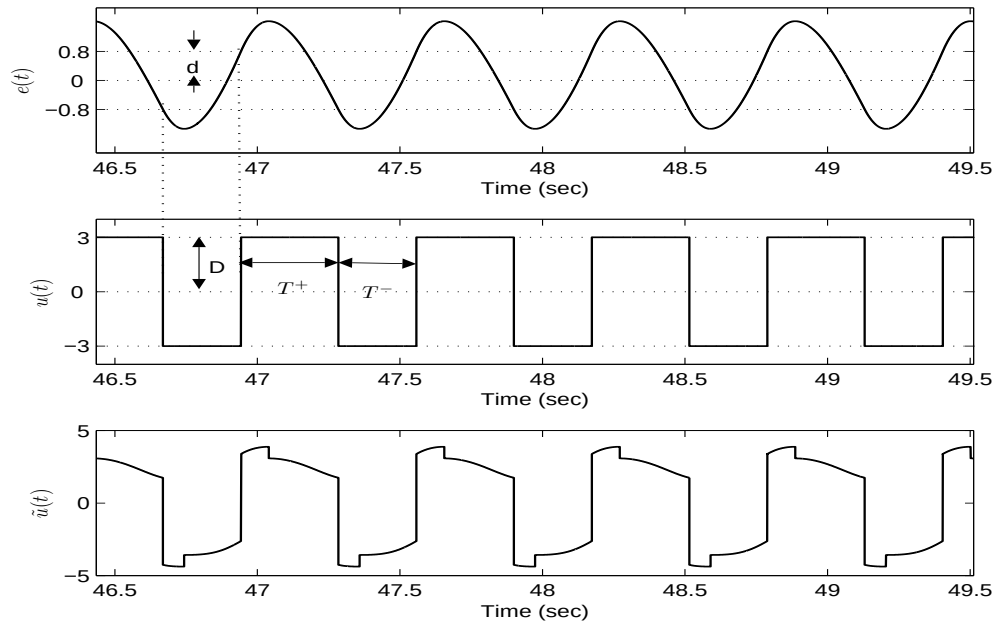

Figure 5.9: Input $e(t)$ and output $u(t)$ of the hysteretic relay and actual control signal $\tilde{u}(t)$ with $d = 0.8$, $D = 3$, $\phi = \pi/6$.

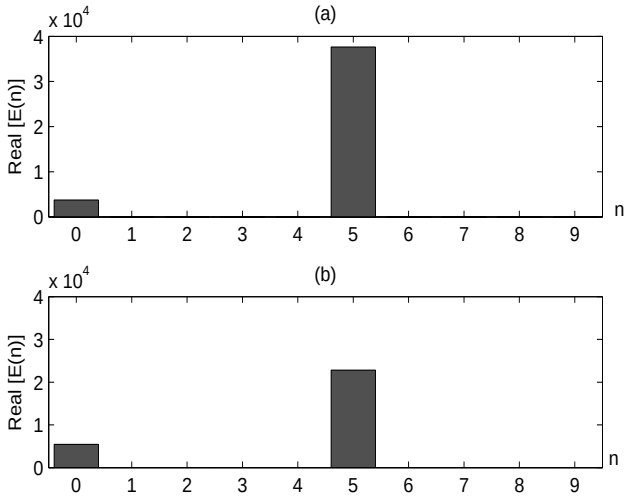

Figure 5.10: Spectrums of limit cycles near the DC region with $m = 5$. Left: with $d = 1.2$, $D = 5$, $\phi = \pi/6$, $N = 29295$. Right: with $d = 0.8$, $D = 3$, $\phi = \pi/6$, $N = 32615$.

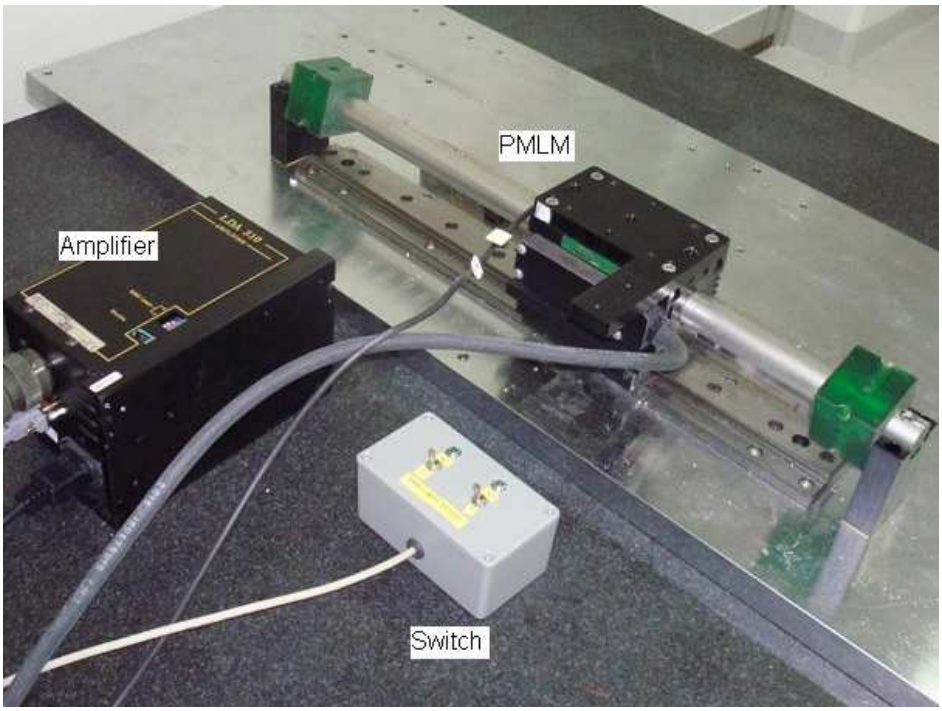

Figure 5.11: The PMLM used in this experiment.

5.5.1 Identification of the spatial cogging frequency

In the first part of experiment, the spatial cogging frequency Ω is identified from the velocity curve with a step voltage input to the PMLM. Figure 5.13 and Figure 5.14 shows the open-loop response of the PMLM with different input voltages. From these two figures, after the initial transience, an almost constant velocity trend is observed in the position signals. However, due to the existence of force ripples, the actual velocity signal manifests a periodic oscillating behavior about a mean level. Denote the mean velocity in the steady state as $\overline{v}$, the period of the velocity oscillation as T_v, then the spatial cogging frequency (in rad/m) can be simply measured as

$$\Omega = \frac{2\pi}{\overline{v}T_v}. \tag{5.37}$$

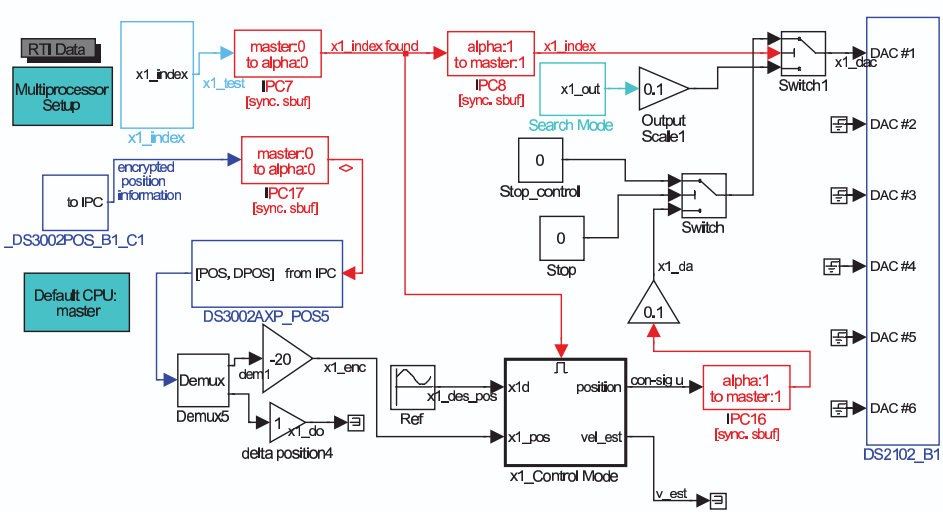

Figure 5.12: The Simulink program for experiment.

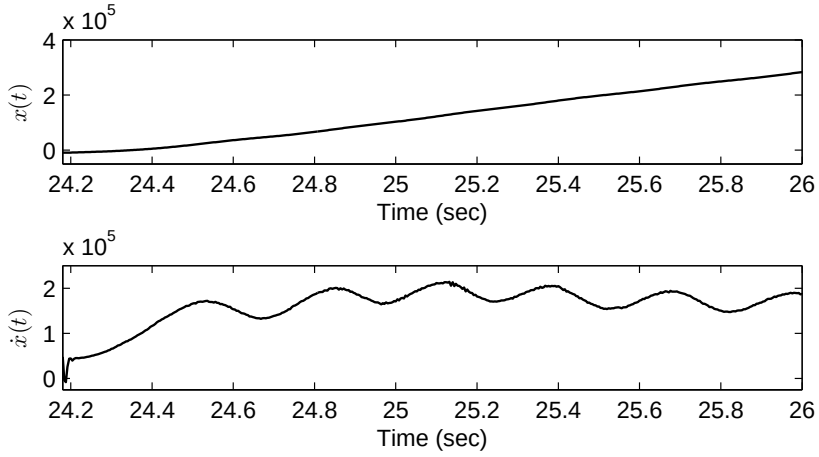

Figure 5.13: Position $x(t)$ (in μ m) and velocity $\dot{x}(t)$ (in μ m/s) of the PLMM with $u = 0.3\,\mathrm{V}$.

Form Figure 5.13, $T_v = 0.2744\,\mathrm{sec}$ and $\overline{v} = 0.18388\,\mathrm{m/sec}$. Hence, by (5.37), Ω is estimated as $124.39\,\mathrm{rad/m}$. Similarly, from Figure 5.14, $T_v = 0.1620\,\mathrm{sec}$, $\overline{v} = 0.3154\,\mathrm{m/sec}$, and Ω is obtained as $122.97\,\mathrm{rad/m}$. Thus, the spatial cogging frequency is identified as $\Omega = 123.68\,\mathrm{rad/m}$ by taking the mean value of above two.

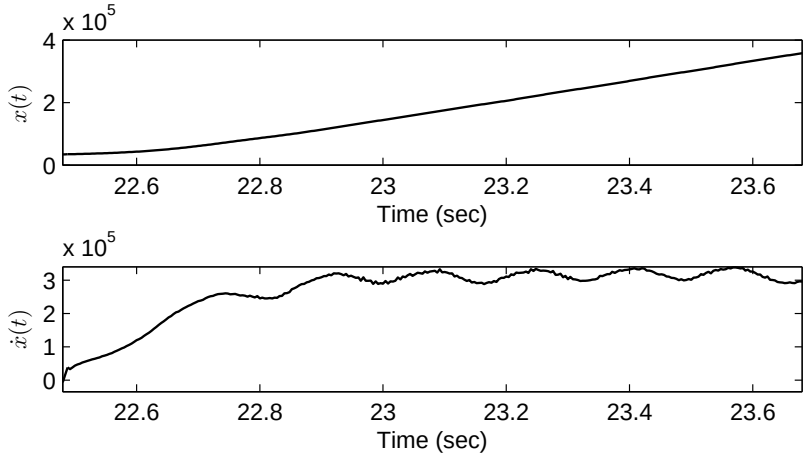

Figure 5.14: Position $x(t)$ (in μm) and velocity $\dot{x}(t)$ (in μ m/s) of the PLMM with $u = 0.5\,\mathrm{V}$.

5.5.2 Parameter estimation

To estimate the model parameters of the selected model of PMLM, choose $d_1 = 5 \times 10^{-4}\,\mathrm{m}$, $D_1 = 0.6\,\mathrm{V}$, $d_2 = 8\times10^{-4}\,\mathrm{m}$ and $D_2 = 0.7\,\mathrm{V}$. The sampling period for experiment is set to 4 ms, and the reference position is set on the 7 cm from the homing position. The results of inputs and outputs of hysteristic relay over five periods of oscillations are shown in Figure 5.15 and Figure 5.16 accordingly. From these figures, the oscillation frequencies are $\omega_1 = 28.3537\,\mathrm{rad/sec}$ and $\omega_2 = 28.560\,\mathrm{rad/sec}$. Figure 5.17 shows the spectrum of the window with five periods of $e(t)$ near the DC region, from which, it can be concluded that it is appropriate to approximate the steady oscillating signals by their dominant fundamental frequency components plus DC biases. By (5.34)$\sim$(5.35), the limit cycle parameters are obtained as $A_1 = 2.4317 \times 10^{-3}\,\mathrm{m}$, $B_1 = 1.4552 \times 10^{-3}\,\mathrm{m}$, $A_2 = 3.4978 \times 10^{-3}\,\mathrm{m}$ and $B_2 = 1.6905 \times 10^{-3}\,\mathrm{m}$. With the explicit equations given in (5.29)$\sim$(5.33), the system parameters are identified as $a = 6.474$, $b = 4.284$, $C_1 = 0.199$,

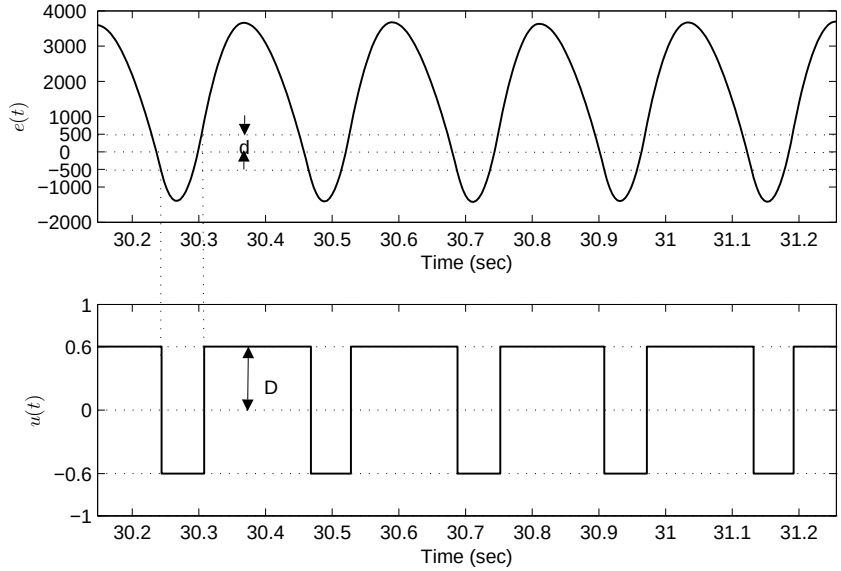

Figure 5.15: Input $e(t)$ (in μ m) and output $u(t)$ (in V) of the hysteretic relay with $d = 0.5\,\text{mm}$, $D = 0.6\,\text{V}$.

$C_2 = -0.303$, and $f = 0.042$.

5.5.3 Model compensation

To verify the model obtained, a linear feedback controller is commissioned and the feedforward model-based nonlinear compensator is initialized as shown in Figure 5.18. The desired moving profile is set as $x_d = 0.02\sin(2\pi t)$ (unit in m). After fine tuning, the linear PID feedback controller is set as $k_p = 0.0243\,V/\mu$ m, $k_i = 0$, $k_d = 0.00013\,\text{V sec}/\mu$ m, with the feedforward controller settings based on the parameters estimated earlier, the tracking error are shown in Figure 5.19(a). For a fair comparison, the tracking performance is tested with same linear feedback controller but without the ripple and friction compensation. The results are shown in Figure 5.19(b). By comparing the above two compensation results, it is able to observe that the maximum tracking errors are

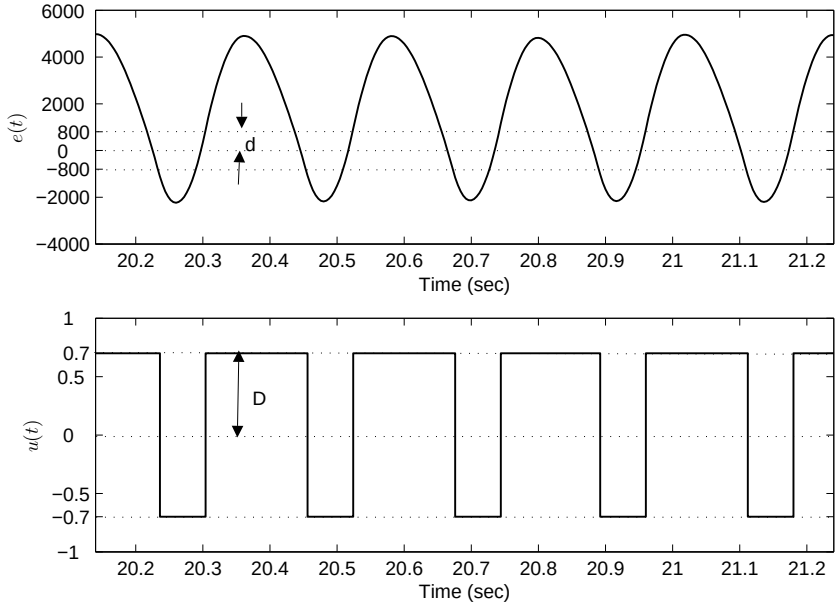

Figure 5.16: Input $e(t)$ (in μ m) and output $u(t)$ (in V) of the hysteretic relay with $d = 0.8\,\text{mm}$, $D = 0.7\,\text{V}$.

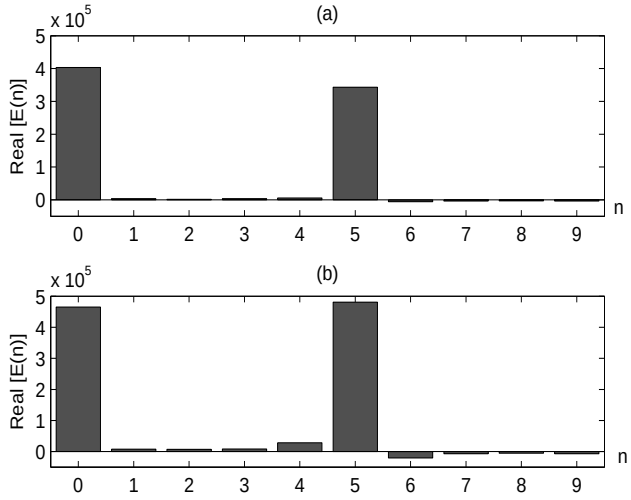

Figure 5.17: Spectrums of limit cycles near the DC region with $m = 5$. Left: with $d = 0.5\,\text{mm}$, $D = 0.6\,\text{V}$, $N = 277$. Right: with $d = 0.8\,mm$, $D = 0.7\,\text{V}$, $N = 275$.

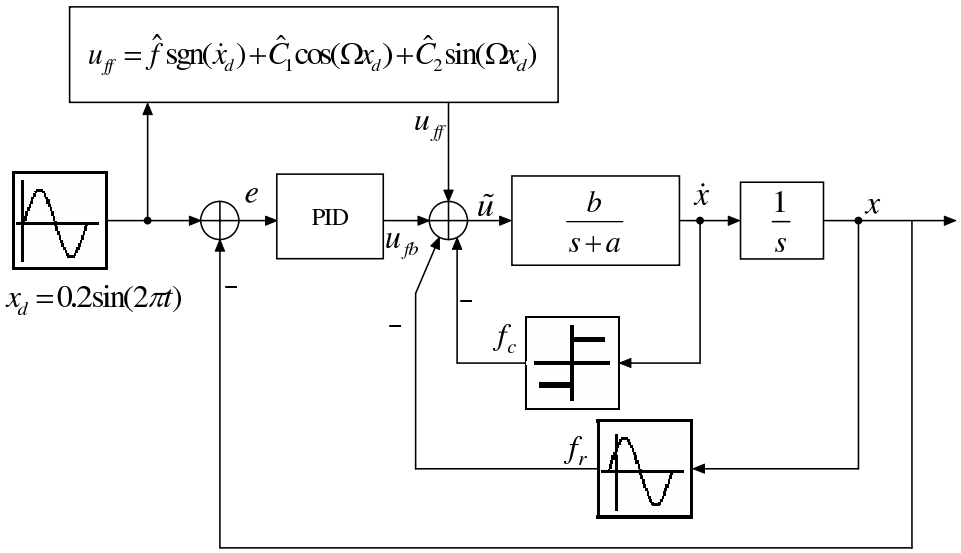

Figure 5.18: Design of compensation scheme, with combination of feedback control u_{fb} and feedforward control u_{ff}.

reduced dramatically from 15 μ m to less than 4.7 μ m (or around 70% improvement), which also verify the validity of the model parameters obtained in Section 5.5.2.

5.6 Conclusion

A new relay-based identification method has been developed to identify the model parameters in permanent magnet linear motor (PMLM), including models for force ripples and friction. Due to existence of non-odd, force ripple nonlinearity in PMLM, biased limit cycles are observable from the symmetric hysteretic relay feedback. Dual-input describing function is thus imported for analysis of bias limit cycles within the relay feedback system to establish a harmonic balance condition. Based on this condition, a set of explicit formulae is derived for direct computation of model parameters. Simulation results and real-time experiments have demonstrated the simplicity and effectiveness of the proposed modeling method. The validity of the model is also verified via

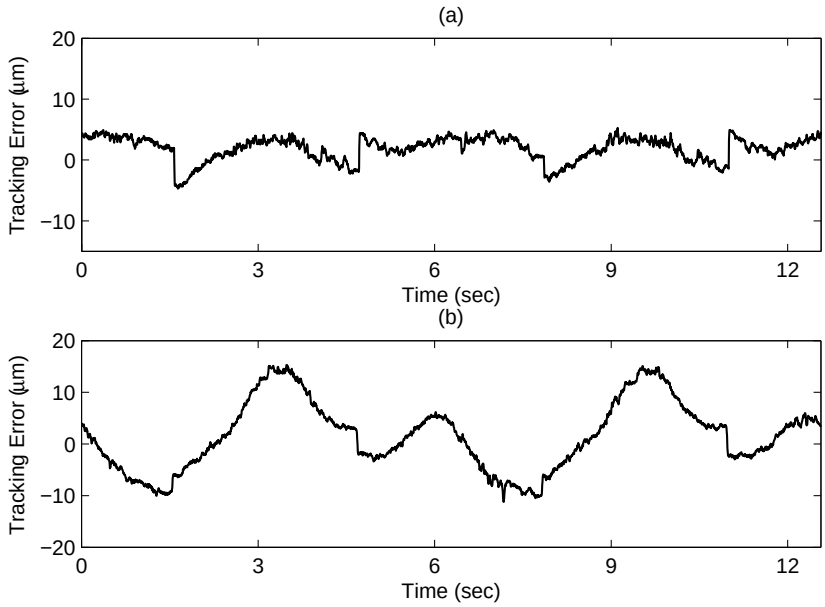

Figure 5.19: Tracking performance of control schemes. (a) With nonlinear feedforward compensation. (b) Without nonlinear feedforward compensation.

model-based compensation, which achieves a superior tracking performance compared to classical linear feedback control without nonlinearity compensation.

Chapter 6

Conclusions

Various nonlinear factors exist in the actuators of motion control systems, such as control valves and electric linear motors, which affect the their performance. It is important to model their behaviors and use appropriate control schemes to eliminate these effects and increase the precision of the motion control systems. The contributions from this thesis are summarized and the recommended future works are also given in this chapter.

6.1 Summary of Contributions

Efficient models and fast identification methodologies have been developed for motion control systems using relay feedback approaches. First, to improve the behavior description of sticky control valve, a two-layer binary tree data-driven stiction model has been proposed. The model is able to completely describe the various of categories of stiction behavior in control valve, with simple logic structures.

Secondly, the locations of limit cycles and stability of limit cycles are analyzed in a class of linear systems with full-state and triple-relay feedback. In practice, the triple-relay feedback configuration maps directly to a servo-mechanical system affected by Coulomb

friction, under deliberate of DCR feedback. A new method, leveraging on the presented analysis, is thus to identify the dynamical and friction parameters of the servo system accurately with only a single relay experiment, surpassing existing results.

Thirdly, by describing function analysis, the properties of limit cycles within servo-mechanical systems impended by a recently proposed four-parameter friction model are carefully investigated. These properties are directly useful for tuning the DCR gains, so that sets of explicit formulae are derived to obtain most of model parameters using experiments of both low and high velocity modes in position feedback loop, with minimum usage of NLS. This improvement greatly releases the computational intensity and increases the robustness of estimation.

Finally, force ripples in PMLM together with friction with hysteretic relay feedback are modeled with hysteretic relay feedback. Due to force ripples' asymmetric nonlinearity, biased limit cycles are observed under relay feedback. Thus, instead of using conventional SIDF, the DIDF is introduced to correctly describe nonlinear characteristics under biased limit cycles. From here, harmonic balance conditions are set up, so that explicit formulae are given for directly computing the all the linear and nonlinear model parameters in PMLM, including Coulomb friction and force ripples.

In this thesis, extensive simulations and experiment results have been furnished to illustrate the effectiveness of the proposed model or modeling methods.

6.2 Suggestions for Future Works

Regarding modeling motion control systems with relay feedback approach, although above contributions have been made in this thesis, there are some topics remaining unsolved till now. Thus, the suggestions for future works are given below.

To identify more complicated state-dependent friction models In this thesis, differential friction models are identified, from single parameter one to multi-parameter one. However, these models are all static models, which are static functions with respect to velocities. One of hot research topics is identification of dynamic friction models such as Dahl model [30], LuGre model [31] and Maxwell slip model [5], which have internal states to describe the deflection of bristles between to contacting surfaces. However, the challenges arisen from unmeasurable internal states of such friction models cause difficulty in model-based compensations. Some existing methods of adaptive control generally do not guarantee the convergence of model parameters to their true valve, if the PE condition is not satisfied.

To use forced oscillations instead of self-excited oscillations Due to its simplicity for analysis, the self-excitation oscillations are commonly used in the relay-based identification methods proposed in this thesis and other publications. However, such self-excited oscillation disturbs the normal operations of the system and causes increase wear and tear of system components [60]. In some situation, the constraints of self-excited oscillations can be released by forced-oscillations or even subharmonic oscillations [14]

due to their lower amplitudes [98]. However, there is few application example of force oscillations on the nonlinear system identification till now, due to the theoretical analysis of forced-oscillation is only limited to FOPDT linear systems currently [60]. The application of forced-oscillations may be possible if the analysis is extended to higher order linear systems or even nonlinear systems.

Bibliography

[1] ——. Motion control. *Wikipedia*, 2009. [Online] http : // en . wikipedia.org / wiki / Motion _ control.

[2] Aerotech, UK. *Linear motors application guide*. [Online] http : // www . aerotech . com / products / PDF / LMAppGuide . pdf.

[3] L. T. Aguilar, I. Boiko, L. Fridman, and R. Iriarte. Generating self-excited oscillations via two-relay controller. *IEEE Transactions on Automatic Control*, 54(2):416–420, Feburary 2009.

[4] H. S. Ahn, Y. Chen, and H. Dou. State-periodic adaptive compensation of cogging and Coulomb friction in permanent-magnet linear motors. *IEEE Transactions on Magnetics*, 41(1):90–98, 2005.

[5] F. Al-Bender, V. Lampaert, and J. Swevers. The generalized Maxwell-slip model: a novel model for friction simulation and compensation. *IEEE Transactions on Automatic Control*, 50(11):1883–1887, 2005.

[6] G. Amontons. On the resistance oriinating in machines. In *Proceedings of the French Royal Academy of Sciences*, pages 206–222, 1699.

[7] B. Armstrong-Helouvry, P. Dupont, and C. C. de Wit. A survey of models, analysis tools and compensation methods for control of machines with friction. *Automatica*, 30(7):1083–1138, 1994.

[8] K. J. Astrom. Oscillations in systems with relay feedback. In K. J. Astrom, G. C. Goodwin, and P. R. Kumar, editors, *Adaptive Control, Filtering and Signal Processing*. Spring-Verlag, 1995.

[9] K. J. Astrom and T. Hagglund. Automatic tuning of simple regulators with specifications on phase and amplitude margins. *Automatica*, 20(5):645–651, 1984.

[10] K. J. Astrom and T. Hagglund. *Automatic Tuning of PID Controllers*. Instrument Society of America, Research Triangle Park, North Carolina, 1988.

[11] K. J. Astrom and B. Wittenmark. *Adaptive control*. Addison-Wesley Longman Publishing Co., Inc., second edition edition, 1994.

[12] D. P. Atherton. *Nonlinear Control Engineering*. Van Nostrand Reinhold, 1975.

[13] A. Basak. *Permanent-Magnet DC Linear Motor*, chapter 2. Oxford University Press, Oxford, 1996.

[14] V.I. Beresnevich and S.L. Tsyfansky. Characteristic properties of subharmonic oscillations and their application in vibration engineering. *Journal of Sound and Vibration*, 280:579–593, 2005.

[15] A. Besancon-Voda and G. Besancon. Analysis of a two-relay system configuration with application to Coulomb friction identification. *Automatica*, 35:1391–1399, 1999.

[16] A. Besancon-Voda and P. Blaha. Describing function approximation of a two-relay system configuration with application to Coulomb friction identification. *Control Engineering Practice*, 10:655–668, 2002.

[17] L. C. Bo and D. Pavelescu. The friction-speed relation and its influence on the critical velocity of the stick-slip motion. *Wear*, 82(3):277–289, 1982.

[18] I. Boldea and S. A. Nasar. *Linear Motion Electromagnetic Devices*, chapter 2-4. Taylor & Francis, NY, 2001.

[19] J. B. Burl. *Linear Optimal Control: H_2 and H_∞ methods.* Addison-Wesley Longman Publishing Co., Inc., Boston, MA, 1998.

[20] S. L. Chen, W. B. Lai, T. H. Lee, and K. K. Tan. Development of an intelligent physiotherapy system. In J. Billingsley and R. Bradbeer, editors, *Mechatroncis and Machine Vision in Practice*, pages 267–273. Springer, Berlin Heidelberg, 2008.

[21] S. L. Chen, J. Shenoy, K. K. Tan, and S. Huang. A collation of recent valve stiction model and compensation approach. *International Journal of Process System Engineering*, 1(1):32–42, 2008.

[22] S. L. Chen, K. K. Tan, and S. Huang. Improvement of tracking performance of servomechanical system by an accurate four-parameter friction modeling and compensation. In *Proceedings of 14th International Conference on Mechantronics and Machine Vision in Practice*, pages 28–34, Xiamen, China, 2007.

[23] S. L. Chen, K. K. Tan, and S. Huang. Friction modeling and compensation of servo-mechanical system using a dual-relay feedback approach. *IEEE Transactions on Control Systems Technology*, 2008. Accepted.

[24] S. L. Chen, K. K. Tan, and S. Huang. Two-layer binary tree data-driven model for valve stiction. *Industrial & Engineering Chemistry Research*, 47:2842–2848, 2008.

[25] Y.-Y. Chen, P.-Y. Huang, and J. Y. Yen. Frequency-domain identification algorithms for servo systems with friction. *IEEE Transactions on Control Systems Technology*, 10(5):654–665, 2002.

[26] M. A. A. S. Choudhury, S. L. Shah, N. F. Thornhill, and D. S. Shook. Auotmatic detection and qualification of stiction in control valves. *Control Engineering Practice*, 14:1395–1412, 2006.

[27] M. A. A. S. Choudhury, N. F. Thornhill, and S. L. Shah. Modelling valvue stiction. *Control Engineering Practice*, 13:641–658, 2005.

[28] C. A. Coulomb. Theorie des machines simples, en ayant egard au frottement de leurs parties, et a la roideur dews cordages. *Mem. Math Phys.*, 1785.

[29] L. Da Vinci. *The Notebooks*. Dover, NY, 1519.

[30] P. R. Dahl. A solid friction friction. Report AFO 4695-67-C-0158, Aerospace Corportation, EI Segundo, California, 1968.

[31] C. C. de Wi, H. Olsson, K. J. Astrom, and P. Lischinsky. A new model for control of systems with friction. *IEEE Transactions on Automatic Control*, 40(3):419–425, 1995.

[32] P. Dupont, V. Hayward, B. Armstrong, and F. Altpeter. Single state elastoplastic friction models. *IEEE Transactions on Automatic Control*, 47(5):787–792, 2002.

[33] C. Edwards and S. K. Spurgeon. *Sliding mode control: theory and applications*. CRC Press, 1998.

[34] A. F. Filippov. *Differential Equations with Discontinous Righthand Sides*. Kluwer Academic Publishers, 1988.

[35] M. Friman and K. V. Waller. A two-channel relay for autotuning. *Industrial & Engineering Chemistry Research*, 36:2662–2671, 1997.

[36] A. Gelb and W. E. V. Velde. *Mutiple-input Describing Functions and Nonlinear System Design*. McGraw-Hill, 1968.

[37] T. T. Georgiou and M. C. Smith. Robustness of a relaxation oscillator. *International Journal of Robust and Nonlinear Control*, 10:1005–1024, 2000.

[38] J. Gerry and M. Ruel. How to measure and combat valve stiction. Presentation, ISA, Houston, TX, USA, 2001.

[39] J. M. Goncalves, A. Megretski, and M. A. Dahleh. Semi-global analysis of relay feedback systems. In *Proceedings of IEEE Conference on Decision and Control*, volume 2, pages 1967–1972, 1998.

[40] J. M. Goncalves, A. Megretski, and M. A. Daleh. Global stability of rela feedback systems. *IEEE Transactions on Automatic Control*, 46(4):550–562, 2001.

[41] T. Gray. *Motion Control*, 2009. [online] http: // www . olympus - controls . com / support _ services / presentations / Motion _ Control _ v2 . pdf.

[42] J. Guckenheimer and P. Holomes. *Nonlinear Oscillations, Dynamical Systems, and Bifurcatiions of Vector Fields*. Springer-Verlag, New York, 1983.

[43] Q. P. He, J. Wang, M. Pottmann, and S. J. Qin. A curve fitting method for detecting valve stiction in oscillating control loops. *Industrial & Engineering Chemistry Research*, 13:4549–4560, 2007.

[44] R. H. A. Hensen, M. J. G de Molengraft, and M. Steinbuch. Friction induced hunting limit cycles: a comparison between the LuGre and switch friction model. *Automatica*, 39:2131–2137, 2003.

[45] R. H. A. Hesen, M. J. G. van de Molengraft, and M. Steinbuch. Frequency domain identification of dynamic friction model parameters. *IEEE Transactions on Control Systems Technology*, 10(2):191–196, 2002.

[46] Y. Hong and B. Yao. A global stable high-performance adaptive robust control algorithm with input saturation for precision motion control of linear motor drive systems. *IEEE/ASME Transactions on Mechatronics*, 12(2):198–207, 2007.

[47] A. Horch. *A Conditional Monitoring of Control Loops*. PhD thesis, Royal Institute of Technology, Stockholm, Sweden, 2000.

[48] C. Hsieh and Y.-C. Pan. Dynamic behavior and modelling of the pre-sliding static friction. *Wear*, 242:1–17, 2000.

[49] S. Huang, K. K. Tan, and K. Z. Tang. *Neural Network Control: Theory and Applications*. Research Studies Press, 2004.

[50] S. L. S. Jocoby, J. S. Kowalik, and J. T. Pizzo. *Iterative Methods for Nonlinear Optimization*. Prentice-Hall, NJ, 1972.

[51] K. H. Johansson, A. Rantzer, and K. J. Astrom. Fast switches in relay feedback systems. *Automatica*, 35(4):539–552, 1999.

[52] M. Kano, H. Maruta, H. Kugemoto, and K. Shimizu. Practical model and detection algorithm for valve stiction. In *IFAC Symposium on Dynamics and Control of Process Systems*.

[53] I. Karasik. Friction. In I. S. Grigoriev and I. S. Meilikhov, editors, *Handbook of Physical Quantities*. CRC Press, Boca Raton, FL, 1997.

[54] A. Kayihan and F. J. Doyle. Friction compensation for a process control valve. *Control Engineering Practice*, 8(7):799–812, 2000.

[55] M. S. Kim and S. C. Chung. Friction identification of ball-screw driven servomechanisms through limit cycle analysis. *Mechatronics*, 16:131–140, 2006.

[56] P.V. Kokotovi. The joy of feedback: nonlinear and adaptive. *IEEE Control Systems Magazine*, pages 7–17, June 1992.

[57] M. Krstic, I. Kanellakopoulos, and P. V. Kokotovic. Nonlinear design of adaptive controllers for linear systems. *IEEE Transactions on Automatic Control*, 39(4):738–752, April 1994.

[58] V. Lampaert, J. Swevers, and F. Al-Bender. Identification of the Leven integrated friction model structure. *IEEE Transactions on Automatic Control*, 47(4):683–687, April 2002.

[59] T. H. Lee, K. K. Tan, S. Y. Lim, and H. F. Dou. Iterative learning of permanet magnet linear motor with relay automatic tuning. *Mechatronics*, 16:169–190, 2000.

[60] L. H. Lim, A. P. Loh, and W. W. Tan. On forced and subharmonic oscillations under relay feedback. *IET Control Theory & Applications*, 2(9):829–840, 2008.

[61] C. Lin, Q.-G. Wang, and T. H. Lee. Relay feedback: a complete analysis for first-order systems. *Industrial & Engineering Chemistry Research*, 43(26):8400–8402, November 2004.

[62] C. Lin, Q.-G. Wang, and T. H. Lee. Existence of solutions to MIMO relay feedback systems. *International Journal of System Science*, 36(10):663–668, 2005.

[63] C. Lin, Q.-G. Wang, T. H. Lee, A. P. Loh, and K. H. Kwek. Stability criteria and bounds for limit cycles of relay feedback systems. *Dynamical Systems*, 19(2):161–170, 2004.

[64] D. K. Linder. *Introduction to Signals and Systems*, chapter 20. McGraw-Hill, Singapore, 1999.

[65] L. Lu, Z. Chen, B. Yao, and Q. Wang. Desired compensation adaptive robust control of a linear-motor-driven precision idustrial gantry with improved cogging force compensation. *IEEE/ASME Transactions on Mechatronics*, 13(6):617–624, 2008.

[66] L. Marton. On analysis of limit cycles in positioning system near Stricbeck velocities. *Mechatronics*, 18:46–52, 2008.

[67] The Mathworks Inc. *Optimization Toolbox User's Guide*, 2000.

[68] G. K. McMillan. Improve control valve response. *Chemical Engineering Progress: Measure, Control*, pages 77–84, 1995.

[69] A. J. Morin. New friction experiments carried out at Metz in 1831-1833. In *Proceedings of the French Royal Academy of Sciences*, volume 4, pages 1–128, 1833.

[70] F. Muller. Simulation of an air operated sticky flow control valve. In *Proceedings of the 1994 Summer Computer Simulation Conference*, pages 742–745, 1994.

[71] H. Nakazawa. *Principles of Precision Engineering*. Oxford University Press, NY, USA, 1994.

[72] H. Olsson. *Control of System with Friction*. PhD thesis, Lund Institute of Technology, Sweden, 1996.

[73] H. Olsson and K. J. Astrom. Friction generated limit cycles. *IEEE Transactions on Control Systems Technology*, 9(4):629–631, 2001.

[74] J. Piipponen. Controlling process with nonideal valves: tuning of loops and selection of valves. In *Preprint of Control System'96*, pages 179–186, Halifax, Nova Scotia, Canada, 1996.

[75] J. A. Profea III. Linear motor basics. *Production Machining*, April 2008. [Online] http: // www . productionmachining . com / articles / linear - motor - basics.aspx.

[76] A. S. Putra, S. Huang, K. K. Tan, S. K. Panda, and T. H. Lee. Design, modeling, and control of piezoelectric actuators for intracytoplasmic sperm injection. *IEEE Transactions on Control Systems Technology*, 15(5):879 – 890, Sept 2007.

[77] O. Reynolds. On the theory of lubrication and its applications to Mr. Beauchamp Tower's experiments. *Philosophical Transactions of the Royal Society*, 177:157–234, 1886.

[78] D. D. Rizos and S. D. Fassois. Friction identification based upon the LuGre and Maxwell slip models. *IEEE Transactions on Control System Technology*, 17(1):153–160, Jan 2009.

[79] M. Ruel. Stiction: The hidden menace. *Control Engineering*, pages 69–75, 2000.

[80] Sewoo Industrial Systems Co., Ltd. *Linear motor*. [Online] http : // www . alibaba . com / product / sunjianan1977 - 10712955 - 10545318 / Linear_Motor . html.

[81] S. H. Shen, J. S. Wu, and C. C. Yu. Use of bias relay feedback for system identification. *AIChE Journal*, 42(4):174–1180, 1996.

[82] J. J. E. Slotine and J. A. Coetsee. Adaptive sliding controller synthesis for nonlinear systems. *International Journal of Control*, 43(6):1631–1651, 1986.

[83] J. J. E. Slotine and W. Li. *Applied Nonlinear Control*. Prentice Hall, NJ, 1991.

[84] Y. Song. *The Exploitation of the Work of Nature*. Pennsylvania State University Press, 1966. First print in 1637 in Chinese, English translation by E. Z. Sun and S. C. Sun.

[85] ISA Subcommittee SP75.05. Process instrumentation terminology. Technical report, Instrument Society of America, Research Triangle Park, NC, 1979.

[86] G. Stein. Adaptive flight control: A pragmatic view. In K. S. Narendra and R. V. Monopoli, editors, *Applications of Adaptive Control*. Academic Press, NY, 1980.

[87] J. Swevers, F. Al-Bender, C. G. Ganseman, and T. Prajogo. An integrated friction model structure with improved presliding behavior for accurate friction compensation. *IEEE Transactions on Automatic Control*, 45(4):675–686, April 2000.

[88] K. K. Tan, S. J. Chin, and H. F. Dou. Feedforward suppression of force ripple based on a simplex-optimized dither signal. *ISA Transactions*, 42:19–27, 2003.

[89] K. K. Tan, S. N. Huang, and T. H. Lee. Robust adaptive numerical compensation for friction and force ripple in permanent-magnet linear motors. *IEEE Transactions on Magnetics*, 38(1):221–228, 2002.

[90] K. K. Tan, T. H. Lee, H. Dou, and S. Zhao. Force ripple suppression in iron-core permanent magnet linear motors using a adaptive dither. *Journal of Franklin Institute*, 341:375–390, 2004.

[91] K. K. Tan, T. H. Lee, and S. Huang. *Precision Motion Control: Design and Implementation*. Springer, London, 2nd edition, 2008.

[92] K. K. Tan, T. H. Lee, S. N. Huang, and X. Jiang. Friction modeling and adaptive compensation using a relay feedback approach. *IEEE Transactions on Industrial Electronics*, 48(1):169–176, 2001.

[93] K. K. Tan and S. Mekid. Actuators, transmission and sensors. In S. Mekid, editor, *Introduction to Precision Machine Design and Error Assessment*, Mechanical Engineering Series, chapter 7, pages 253–288. CRC Press, Boca Raton, FL, 2008.

[94] K. K. Tan, Q.-G. Wang, and C. C. Hang with T. J. Hagglund. *Advances in PID Control*. Springer-Verlag, London, 1999.

[95] K. K. Tan, Y. Xie, and T. H. Lee. Automatic friction identification and compensation with a self-adapting dual relay. *Intelligent Automation and Soft Computing*, 9(2):83–95, 2003.

[96] K. K. Tan, S. Zhao, and S. N. Huang. Iterative reference adjustment for high precision and repetitive motion control applications. *IEEE Transactions on Control Systems Technology*, 13(1):85–97, 2005.

[97] K. Z. Tang, S. N. Huang, K. K. Tan, and T. H. Lee. Combined PID and adaptive nonlinear control for servo mechanical systems. *Mechatronics*, 14:701–714, 2004.

[98] Ya. Z. Tsypkin. *Relay Control Systems*. Cambridge University Press, Cambridge, 1984.

[99] United Nation. The convention on biological diversity, 1992. [Online] http: // www . cbd . int / convention / convention . shtml.

[100] Q.-G. Wang, T. H. Lee, and C. Lin. *Relay Feedback: Analaysis, Identification and Control*. Springer-Verlag, London, 2002.

[101] J.-X. Xu and Y. Tan. *Linear and Nonlinear Iterative Learning Control*. Springer, 2003.

[102] R. R. Yager and D. P. Filev. *Essentials of Fuzzy Modeling and Control*. John Wiley, NY, 1994.

[103] B. Yao and L. Xu. Adaptive feedforward compensation of force ripples in linear motors. *Mechatronics*, 12:595–616, 2002.

[104] Z. Ye, Q.-G. Wang, C. Lin, C. C. Hang, and A. E. Barabanov. Relay feedback analysis for a class of servo plants. *Journal of Mathematical Analysis and Applications*, 334:28–42, 2007.

[105] C. C. Yu. *Autotuning of PID Controllers*. Springer, London, 2nd edition, 2007.

[106] S. Zhao, A. S. Putra, K. K. Tan, S. K. Panda, and T. H. Lee. Intelligent compensation of friction, ripple and hysteresis via a regulated chatter. *ISA Transactions*, 45(3):419–433, 2006.

[107] S. Zhao and K. K. Tan. Adaptive feedforward compensation of force ripples in linear motors. *Control Engineering Practice*, 13(9):1081–1092, 2005.

Author's Publications

Journal Papers:

1. S. L. Chen, K. K. Tan, and S. Huang. Two-layer binary tree data-driven model for valve stiction. *Industrial & Engineering Chemistry Research*, 47(8):2842-2848, 2008.

2. S. L. Chen, J. Shenoy, K. K. Tan, and S. Huang. A collation of recent valve stiction model and compensation approach. *International Journal of Process System Engineering*, 1(1):32-42, 2008.

3. S. L. Chen, K. K. Tan, and S. Huang. Friction modeling and compensation of servo-mechanical system with dual-relay feedback approach. *IEEE Transactions on Control Systems Technology*, 17(6):1295-1305, 2009.

4. S. L. Chen, K. K. Tan, and S. Huang. Limit cycles induced in type-1 linear systems with PID-type relay feedback. *International Journal of System Sciences*, 40(12), 1229-1239, 2009.

5. S. L. Chen, K. K. Tan, S. Huang, and C. S. Teo. Modeling and compensation of ripples and friction in permanent magnet linear motor using a hysteretic relay.

IEEE/ASME Transactions on Mechatronics, accepted 2009.

6. S. L. Chen, K. K. Tan, and S. Huang. Limit cycles of a class of systems under full state relay feedback, with application to modeling of friction-impended servo-mechanical systems. *IEEE Transactions on Control Systems Technology*, under review.

Conference Papers:

1. S. L. Chen, K. K. Tan, and S. N. Huang. Friction modelling of servomechanical systems with dual-relay feedback. In *Proceedings of 33rd Annual Conference of the IEEE Proceedings of Industrial Electronics Society*, pages 557-562, Taipei, Taiwan, November, 2007.

2. S. L. Chen, K. K. Tan, and S. N. Huang. Limit cycles in a class of systems under PID-type of relay feedback. In *Proceedings of 33rd Annual Conference of the IEEE Proceedings of Industrial Electronics Society*, pages 915-920, Taipei, Taiwan, November, 2007.

3. S. L. Chen, K. K. Tan, and S. Huang. Improvement of tracking performance of servomechanical system by an accurate four-parameter friction modelling and compensation. In *Proceedings of 14th International Conference on Mechantronics and Machine Vision in Practice*, pages 2834, Xiamen, China, December, 2007.

4. S. L. Chen, S. Huang, and K. K. Tan. Relay-based force ripple and friction mod-

eling for the permanent magnet linear motor. In *Proceedings of 10th International Conference on Control, Automation, Robotics and Vision*, pages 2015-2019, Hanoi, Vietnam, December, 2008.

5. S. L. Chen, K. K. Tan, S. Huang, C. S. Teo, and T. H. Lee. Concurrent friction and ripple modeling servomechanisms using a hysteretic relay. *9th International IFAC Symposium on Robot Control*, Gifu, Japan September 9-12, 2009, accepted.

Chapters in Books:

1. S. L. Chen, W. B. Lai, T. H. Lee, and K. K. Tan. Development of an intelligent physiotherapy system. In J. Billingsley and R. Bradbeer editors, *Mechatronics and Machine Vision in Practice*, pages 267-273. Springer, Berlin Heidelberg, 2008.

2. S. L. Chen, K. K. Tan, S. N. Huang, and K. Z. Tang. Intelligent approach to cordblood collection. In J. Billingsley and R. Bradbeer editor, *Mechatronics and Machine Vision in Practice*, pages 255-260. Springer, Berlin Heidelberg, 2008.

Design for Competition:

1. R. Yang, S.-L. Chen, and K. K. Tan. Motor Dynamics Simulation Systems. 3rd Prize, *Agilent VEE Challenge 2008*. Penang, Malaysia, 2008.